THE WEST AFRICAN MONSOON: DYNAMICS, DECADAL VARIABILITY AND INTERACTION WITH THE EASTERN TROPICAL ATLANTIC SSTS

A Dissertation

Presented to the Faculty of the Graduate School

of Cornell University

In Partial Fulfillment of the Requirements for the Degree of

Doctor of Philosophy

by

Samson Hagos

January 2008

THE WEST AFRICAN MONSOON: DYNAMICS, DECADAL VARIABILITY AND INTERACTION WITH THE EASTERN TROPICAL ATLANTIC SSTS

Samson Hagos, Ph.D.

Cornell University 2008

This dissertation documents regional modeling studies of various aspects of West African Monsoon dynamics and variability. The physical processes responsible for observed characteristics seasonal evolution of the monsoon, its decadal variability and interaction with the Eastern Atlantic Ocean are presented.

The primary mechanism for abrupt latitudinal shift of precipitation maximum from the Guinea coast to the Sahel region, "the monsoon jump", in June is found to be the deepening of the monsoon flow into the continent by inertial instability. This instability is forced by the pressure gradient associated with low level condensational heating due to the pre-existing boundary layer moisture supply onto the warm land surface.

The decadal variability of the West African precipitation, in particular, the causes of the 1980s droughts over the Sahel and the partial recovery of the 1990s, are also studied using the regional atmospheric model. The primary source of variability of precipitation over the Sahel is found to be variability in the moisture transport across its western coast. This moisture transport is influenced by circulation patterns associated with the regional SST anomalies. The 1980s warming over the Indian Ocean, for example, introduces divergence and anticyclonic easterly wind anomalies which drive moisture away from the region and cause widespread drought. In a similar manner, warming over tropical Atlantic Ocean also contributes to the drought. The modeled recovery of the 1990s is found to be due to changes in the scale and distribution of the anomalous SSTs both over the tropical Atlantic and Indian Oceans. These changes introduce cyclonic circulation

patterns that favor westerly transport of moisture towards the Sahel. The response of the region to an SST forcing is related to the background moisture distribution and is enhanced by circulation patterns associated with the changes in the local condensational heating.

Finally, a coupled regional model is used to investigate the two way interaction between the West African Monsoon and seasonal SST variations over the Eastern Tropical Atlantic Ocean. The model allows thermodynamic and dynamic interactions between the atmospheric planetary boundary layer and the ocean mixed layer. The model results show that the seasonal cooling over the Gulf of Guinea between spring and summer is related to increased entrainment and evaporation due to acceleration of the southerly winds driven by the African heat low. Over northeastern tropical Atlantic, the warming due to solar heating is augmented by the suppression of evaporation. The northward migration of the ITCZ leads to weakened northeasterly winds and reduced evaporation. The warming of the northeastern Atlantic, on the other hand, weakens the anticyclonic easterly winds associated with the Atlantic High and strengthen the cyclonic westerly monsoon winds.

BIOGRAPHICAL SKETCH

Samson Hagos was born in 1979 in Asmara, Eritrea. He got his bachelors degree in physics from University of Asmara. His senior research project was on kinetic theory of waves in plasma. After teaching junior level experimental physics at the University, he joined Cornell in 2002 to pursue his graduate studies in Atmospheric Sciences. His particular areas of interests are numerical and theoretical analysis of geophysical fluid dynamical systems. He likes to spend his leisure time reading and taking long hikes.

ACKNOWLEDGEMENTS

This research would not be possible without the assistance of my advisor Prof. Kerry Cook and members of my special committee Profs. Peter Gierasch, Sidney Leibovich and Richard Rand. I also appreciate the technical assistance I got from Dr. Ned Vizy. I am also grateful for the constant support and guidance of Prof. Rudy Wiens and other members of the faculty of University of Asmara, Eritrea. This research was supported by NSF award ATM-0415481.

TABLE OF CONTENTS

LIST OF TABLES

LIST OF FIGURES

Chapter 1

Introduction

The West African Monsoon system is a climatological feature that provides summer rainfall for much of the Sahel region of Africa. This system transports moisture from the tropical Atlantic Ocean. The inhabitants of the Sahel are mainly subsistence farmers and nomads with primitive farming practices which makes them vulnerable to variability in the onset of the monsoon season and the amount of summer rainfall. For example, variations in the onset of sustained rainfall that provides enough soil moisture in relation to the time of planting could make a difference between well rooted healthy plants or the loss of precious seeds and reduced productivity. Just as important is the variability in the total seasonal summer rainfall. This variability has large impact because it is strongly correlated with the long term water, food and power supply for the growing population. These factors in turn, have consequences for the overall security and stability of the region. The widespread Sahel drought of the 1980s, for example, has caused a large number of deaths of humans and livestock and is believed to be at the root of the current political conflicts in the region.

Even though understanding these variabilities of Sahel precipitation over intra-seasonal to decadal timescales has been the subject of many studies, a comprehensive systematic analysis of the physical and dynamical processes in the West African Monsoon system, its interaction with the various regional features and the processes that give rise to variabilities at various time scales has been lacking. The set of modeling studies documented in this dissertation aim to provide a theoretical framework for understanding the important processes that give rise to the observed dynamics and modes of variability.

In the next chapter, a modeling study of the abrupt latitudinal shift of precipita-

tion maximum from the Guinean coast to the Sahel region in the month of June, "the monsoon jump", is presented. The problem is defined and various observational and theoretical studies aimed at explaining the process are reviewed. The model used in this study is described and the simulation results are compared with the observations. In the analysis section, conservation properties of moisture, momentum and energy are used to link the evolution of precipitation with other relevant fields. After the analysis, a paradigm of the monsoon jump process is constructed and compared with previous results from other authors.

In chapter 3, the study of decadal variability of Sahel precipitation, in particular the roles of Atlantic and Indian Ocean sea surface temperatures (SSTs) in the droughts of the 1980s and the partial recovery of 1990s are presented. The regional model's precipitation responses to various SST patterns derived from observations are analyzed. Moisture transport and other nonlinear processes that link SST and precipitation variations are identified. Finally some implications of these results for understanding and prediction of the response of Sahel climate to future SST variations are inferred.

The interaction of the West African Monsoon circulation with Eastern Tropical Atlantic sea surface temperatures (SSTs) are presented in the fourth chapter. Previous efforts at understanding the influence of the monsoon surface winds on the dynamics and thermodynamics of the ocean surface are reviewed. The coupled climate model developed for this study is described. The performance of the model in simulating various atmospheric and ocean surface fields is evaluated. In order to identify the processes that play essential roles in the land-air-sea interactions, the energy budget, the surface pressure and wind fields are analyzed. In conclusion, the main results of these studies are summarized. Their importance in the context of global climate change is discussed and future research directions are suggested.

Chapter 2

Dynamics of the West African Monsoon Jump

Abstract

The observed abrupt latitudinal shift of maximum precipitation from the Guinean Coast into the Sahel region in June, known as the West African monsoon jump, is studied using a regional climate model. Moisture, momentum and energy budget analyses are used to better understand the physical processes that lead to the jump. Because of the distribution of albedo and surface moisture, a sensible heating maximum is in place over the Sahel region throughout the spring. In early May, this sensible heating drives a shallow meridional circulation and moisture convergence at the latitude of the sensible heating maximum, and this moisture is transported upward into the lower free troposphere where it diverges. During the second half of May, the supply of moisture from the boundary layer exceeds the divergence, resulting in a net supply of moisture and condensational heating into the lower troposphere. The resulting pressure gradient introduces an inertial instability, which abruptly shifts the mid-tropospheric meridional wind convergence maximum from the coast into the continental interior at the end of May. This in turn introduces a net total moisture convergence, net upward moisture flux and condensation in the upper troposphere, and an enhancement of precipitation in the continental interior through June. Because of the shift of the meridional convergence into the continent, condensation and precipitation along the coast gradually decline.

2.1 Introduction

The West African monsoon system is a climatological feature of major economic and social importance to the population of the region whose economy heavily relies on agriculture. Understanding its dynamics, variability at various timescales and ultimately improving our skill in predicting its onset and evolution would contribute toward food security and the stability of the region. For example, information on the timing of the onset of the monsoon, that is, the first rains that are sufficient to provide enough soil moisture at the time of planting and uninterrupted by prolonged dry conditions, would enhance agricultural productivity.

The monsoon season begins with intense rainfall near the Gulf of Guinea in April which typically remains in place until the end of June. A secondary precipitation maximum develops near 10^0N in late May. During the last week of June, on average, the coastal precipitation maximum shifts to the latitude of the secondary maximum over a few days. For the rest of the rainy season, the precipitation maximum follows the seasonal cycle fairly accurately. So the monsoon 'jump' can be characterized as the onset of intense convection and rainfall along 10^0N accompanied by its sudden termination along the Guinean Coast. This is in sharp contrast with the fact that the ultimate cause of the seasonal migration of the ITCZ, the northward march of the sun, follows a smooth and continuous cycle.

Currently, there are contrasts between observational studies of the monsoon jump and the theory of monsoon circulations. The purpose of this paper is to improve our understanding of the atmospheric hydrodynamics of the jump by analyzing the fundamental physics of the jump in an atmospheric model that reproduces its observed characteristics. We do not simulate a particular year, but adopt a "climate mode" approach

in which a representative monsoon onset season is generated in the model with climatological surface and lateral boundary forcing. While recent improvements in seasonal forecast skill over West Africa are encouraging, improved insights about the basic dynamics of the jump will provide more relevant predictors of its timing, as well as the overall intensity and distribution of rainfall during the monsoon season.

Our current state of knowledge of monsoon jump processes over West Africa is reviewed in the following section. A description of the regional climate model is provided in section 2.3, and the simulated monsoon jump is compared with the observed. In section 2.4, a systematic analysis of the moisture, momentum, and energy conservation laws is performed to isolate the physical processes responsible for the monsoon jump in the model, and a chronological summary of the process is provided. In the last section, the results are discussed in the context of previous studies on the subject and predictors of the jump are specified.

2.2 Background

Sultan and Janicot (2000) performed an observational analysis of the discontinuity in the northward migration of the ITCZ using gridded station rainfall data compiled at IRD (Institute de Recherche pour la Developpment), ASECNA (Agence pour la Securite De La Navigation Aerienne en Afrique et a Madagascar) and CIEH (Comite Interafricain d'Etudes Hydroliques) as well as the NCEP/NCAR reanalysis (Kalnay et al. 1996) for 1968 to 1999. They suggested that the jump is an acceleration of the seasonal cycle triggered by westward propagating intra-seasonal scale atmospheric circulations. This phenomenon is also documented in an observational study by Le Barbe et al. (2002), who showed that 5^{o}N and 10^{0}N are preferred locations for precipitation maxima. Thus,

the classic vision of a continuous seasonal migration of the ITCZ giving rise to two rainy seasons along the Coast of Guinea and a single one over the Sahel was called into question.

Using the same rain-gauge data as Le Barbe et al. (2002), along with Meteosat IR images, the EPSAT-Niger network, and the NCEP/NCAR reanalysis, Lebel et al. (2003) further confirmed the discontinuity in the northward migration of rainfall over West Africa. They identified two distinct precipitation regimes. The first, referred to as the oceanic regime, involves the seasonal shift of rain onto the coast from the tropical Atlantic. The second phase, the continental regime, consists of a sudden rise in mean daily rainfall and the number of rain events near 10^0N. The continental regime typically starts at the end of June and accounts for 75 to 90% of the total precipitation at this latitude. They also showed that inter-annual variability of Sahelian rainfall is associated with fluctuations in the number of rain-efficient convective systems within the continental regime.

In a detailed study of the monsoon onset in the observations, Sultan and Janicot (2003) suggest that the jump involves complex interactions among convective processes in the ITCZ, African Easterly Jet dynamics, and circulations associated with local topography. They propose that the Ahaggar Plateau and the Tibesti highlands could exert significant control on the atmospheric circulation and convection in the ITCZ. Their explanation of the process can be summarized as follows: About 40 days before true onset, the ITCZ is located near 5^0N and the inter-tropical front (ITF; the line of confluence between the southwesterly moist flow and the northeasterly dry flow) is located near15^0N. Dynamics associated with the heat low dominates the continental region. During this time, isolated convective systems appear over the continent, resulting in an apparent expansion of the ITCZ. About ten days before the jump, the heat low is enhanced by the

interaction of the northeasterly winds with orography. This occurs when the southward advection of dry air cause temporary rainfall decreases south of the ITF and increased radiative heating of the surface. Meanwhile, the seasonal development of the low-level westerly flow and the mid-tropospheric African easterly jet increases the vertical wind shear, which increases the local potential instability. The heat low eventually introduces a reversal in the potential vorticity gradient as well as the generation of African easterly waves and convection. The release of potential instability and subsequent inertial instability then shift the ITCZ to about 10^0N.

A satellite-based study by Gu and Adler (2004) uses rainfall data from the Tropical Rainfall Measuring Mission (TRMM) and surface winds from QuikSCAT, along with the NCEP/NCAR reanalysis, to show that rainfall tends to be concentrated along two latitudes, 5^0N and 10^0N. They found that the precipitation field lies mainly along 5^0N during April, May and June and it is mainly concentrated along 10^0N during July, August and September. They suggested that the appearance of intense rainfall along the Guinean Coast in April is related to the occurrence of warm SSTs over the tropical eastern Atlantic, and its disappearance might be related to the formation of an oceanic cold tongue complex over the region. They conclude that the appearance of the rainfall along 10^0N during the end of June is independent of the Gulf of Guinea precipitation system and the time of the onset of rainfall events at 10^0N coincides with the northward shift of the African easterly jet and its associated vertical and horizontal shear zones and the low-level westerly flow, along with the development of westward propagating African easterly waves. Okumura and Xie (2004) used the CCSR/NIES GCM and showed that the interaction of the monsoon with the equatorial cold tongue might be responsible for the accelerated northward shift of the rain band. According to their result, the monsoon circulation also accelerates the cooling process in the equatorial Atlantic due to surface southerlies, which induce local upwelling.

Most recently, Ramel et al. (2006) and Sijikumar et al. (2006) used a regional numerical model to simulate the monsoon jump of 1992 and suggested that it was related to an abrupt northward shift of the heat low from 10^0-15^0N to 20^0-25^0N. They also showed the existence of some correlation between the location of the easterly flow and the location of rainfall maximum. Similar work by Sijikumar et al. (2006) suggested that the onset of the monsoon is characterized by an increase in the monsoon flow due to a deepened heat low.

Many previous theoretical models of monsoon onset have been presented in the context of zonal symmetry in a moist, geostrophic atmosphere (e.g., Plumb and Hou 1992, Eltahir and Gong 1996). According to these models, monsoon onset occurs because a strictly zonal flow in thermal equilibrium is unsustainable when the absolute vorticity vanishes somewhere inside the system. These ideas are based on the concept of inertial instability, which can occur when a parcel of air in a geostrophic zonal basic state, u_g, is displaced by a distance δy. The meridional acceleration of the parcel is governed by

$$\frac{Dv}{Dt} = -f\left(f - \frac{\partial u_g}{\partial y}\right)\delta y, \tag{2.1}$$

where f is the Coriolis parameter and the term in parentheses is the absolute vorticity. According to (2.1), when a parcel of air is displaced northward ($\delta y > 0$) in the Northern Hemisphere (f > 0) into a region of negative absolute vorticity, it is accelerated further northward. Therefore, a change in sign of absolute vorticity is considered to be the condition for inertial instability, which introduces meridional flow in an otherwise zonal geostrophic flow. These models relate the change in absolute vorticity to the thermal wind, meridional pressure gradients and, ultimately, the meridional boundary layer entropy gradient (Emmanuel 1995).

The onset of the West African monsoon may be more complicated than these models suggest. Due to the complexity of the background flow over West Africa in summer,

advective processes, deviations from geostrophy, and prominent wave activity and pre-onset shallow meridional circulations are likely to play important roles. Nevertheless, these models have contributed to the improvement of seasonal prediction over West Africa. The primary conclusion of these studies is that the latitudinal gradient in heat content is an important determinant of the timing of the onset and strength of the monsoon. Fontaine et al. (1999) used the NCEP/NCAR reanalysis to demonstrate that using the meridional moist static energy (MSE) gradient between the Guinean Coast and the Sahara, along with oceanic indicators, significantly improves prediction skill. Similarly, by performing statistical analysis on Climate Research Unit (CRU) rainfall data along with the NCEP/NCAR reanalysis, Fontaine and Philipon (2000) found that the seasonal evolution of moist static energy over West Africa is particularly relevant to the intensity of the monsoon, with a stronger monsoon signal preceded by a large northward translation of the MSE maximum.

2.3 Simulation

2.3.1 Model description and simulation design

The tropical regional climate model (RCM) used in this study is an adaptation of the PSU/NCAR MM5-V3 (Grell et al. 1994), modified as in Vizy and Cook (2002). The model is non-hydrostatic and it solves the equations governing horizontal and vertical momentum, temperature, pressure, moisture, and liquid water equations on σ surfaces. The full three-dimensional Coriolis force is included.

The model simulation is run over a rectangular domain enclosed by 50^0E to 50^0W and 30^0S to 45^0N. The grid spacing is 90 km. There are 23 vertical levels and the model

time step is 90 seconds. The top of the atmosphere is fixed to be at 50 hPa for this tropical application and an upper radiative boundary condition is used. The effects of snow cover are neglected.

The model is initialized with climatological conditions from the NCEP/NCAR reanalysis and integrated from the 15th of April to the 15th of August and the first 15 days of output are discarded as the spin-up period. The NCEP/NCAR reanalysis is also used for lateral boundary conditions, with monthly means from the reanalysis taken to represent the middle of the month and a linear interpolation in time used to generate the boundary conditions for every 12 hours. SSTs are also prescribed using the reanalysis and interpolated as described above to generate 12 hourly values from the monthly climatology. Surface albedo, moisture availability, emissivity and thermal inertia of the surface are determined from the model's lookup table based on USGS land use categories (Grell et al. 1994).

The Kain-Frisch scheme (Kain and Frisch 1990) is used to parameterize convection. The closure assumes that the convective available potential energy is almost entirely removed at every time step at which convection occurs. This scheme incorporates the effects of entrainment and detrainment as well as downdrafts associated with evaporation of rain on the convection and large-scale environment and it produces realistic precipitation distribution (Vizy and Cook 2002).

Ground temperature is calculated from the surface heat budget using a force-restore method developed by Blackadar (Zhang and Anthes 1982). The heat flow into the ground is calculated by using the bulk aerodynamic formula. Diffusive and latent heat fluxes are calculated using the Blackadar high-resolution planetary boundary layer (PBL) scheme (Blackadar 1979), which uses the Monin-Obukhov similarity model. The nature of the similarity functions used depends on the stability (i.e., the Richardson number)

within the PBL. Horizontal diffusion in the model is parameterized in such a way that it controls aliasing and nonlinear instability. Second order diffusion is used along the boundaries and fourth order elsewhere.

The radiation scheme is adapted from that of the NCAR Community Climate Model 2. Its short-wave scattering/absorption is parameterized by the δ-Eddington approximation (Joseph et al. 1976) and is applied over 18 spectral intervals. The short-wave optical properties of the clouds depend on droplet size and the liquid water path. The scheme treats long wave absorption by ozone and CO_2 using the broadband absorption technique of Kiehl and Briegleb (1991). Long wave broadband emissivity of clouds is a negative exponential function of liquid water path.

2.3.2 Observations of the monsoon jump, and comparison with the model simulation

Figure 2.1a displays the time series of precipitation from the RCM simulation on the model's 90-km grid. The output is averaged between 10^0E and 10^0W where the coastline is parallel to the equator and land surface features such as topography and land use type have zonal uniformity. The model's 3-hourly output is averaged to form daily means. The vertical line marks the Guinean coastline, and the dashed line denotes the approximate date of the monsoon jump. The criteria used by Sultan and Janicot (2003) for the choice of the date of the jump is generalized here to be applicable to modeled precipitation as well as other fields. Here the jump of a maximum of precipitation or any other field from the coast into the continent is said to have occurred if the 10-day average of the field along the 10^0N (hereafter referred to as the continental interior) becomes greater than that at near 5^0N. An intense precipitation band develops near 4^0N in early

May and its latitudinal extent shrinks through June. Meanwhile, precipitation develops in the continental interior and gradually increases in intensity. The continental precipitation becomes greater than the coastal (oceanic) precipitation on about June 27, defined as the date of the monsoon jump in this simulation. After the jump, the continental precipitation migrates northward following the solar forcing. The coastal precipitation dies away after the jump, falling below 2 mm/day after the first week of July.

Similar trends are displayed in the observed climatology but there are important differences from the simulation. Figures 2.1b and 2.1c display the daily mean precipitation from the TRMM (Nicholson et al. 2003a and b) and the Global Precipitation Climatology Project (GPCP; Huffman et al. 2001), respectively. Both are averaged over 1998 – 2004. The horizontal resolution of both of these observations is 1^o of latitude and longitude, only slightly coarser than that of the RCM output so no interpolation has been done for the comparison. In the GPCP observations the jump occurs around the 3^{rd} of July, and in the TRMM data it occurs about one week later, on July 10. Note that even though these observations are averaged over the same time period, the date of the jump is not the same. Unlike in the RCM simulation, precipitation rates greater than 3 mm/day persist until the end of July (not shown) along the coast. Similar to the simulation, the continental precipitation is in place as early as the middle of May, but with magnitudes lower than those along the coast.

A longer-term representation of the precipitation climatology is available from the Climate Prediction Center's Merged Analysis of Precipitation product (CMAP; Xie and Arkin 1997) shown in Figure 2.1d. These are available only for 5-day-means, and the horizontal resolution is only 2.5^o of latitude and longitude, so the jump is not well resolved. However, many of the features of the precipitation development seen in the model and higher resolution data are in evidence. Relatively weak continental precipita-

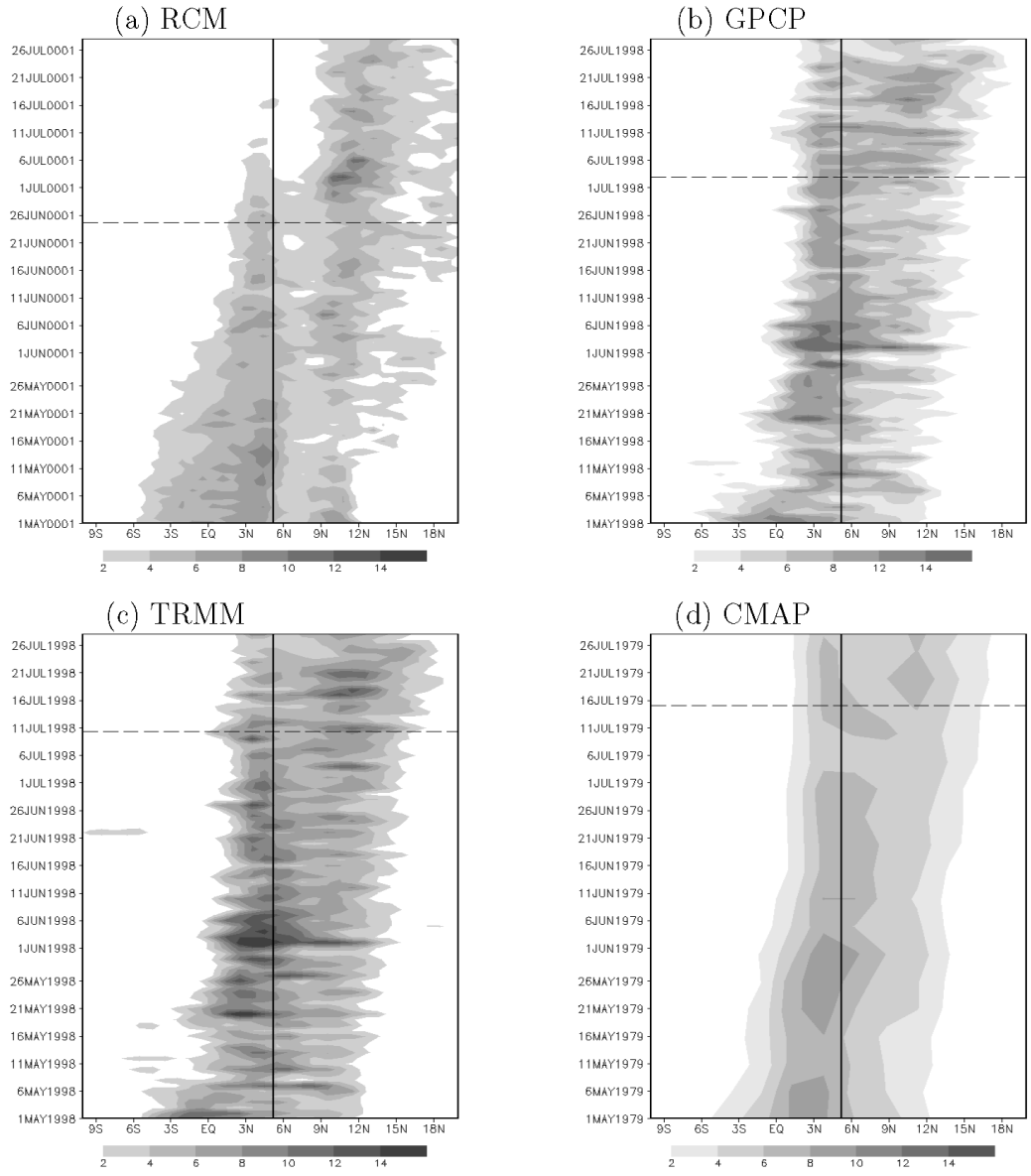

Figure 2.1: Precipitation from the (a) RCM simulation, (b) GPCP 6-year mean, (c) TRMM 6-year mean, and (d) CMAP 6-year mean. All fields are averaged between 10^0E and 10^0W and are in mm/day. Dashed lines indicate approximate date of the monsoon jump and the bold lines represent the approximate latitude of the coastline.

tion develops by mid-May and, in June, the latitudinal extent of the oceanic precipitation shrinks. The jump occurs on roughly the 14th of July, more than two weeks later than in the RCM, 3 days later than in the TRMM data, and 10 days later than in the GPCP observations for 1998-2004. After the jump, precipitation rates up to 5mm/day persist through August along the Guinean coast.

Since averaging over even a few years may obscures the sharpness of the monsoon jump, and the RCM simulation is a single realization of climate and not an average, we also present observations for individual years. Figures 2.2a and 2.2b illustrate the evolution of West African precipitation during 1999 and 2003, respectively, from the TRMM data. Overall, the precipitation field for 1999 is more similar to the climatologies (Figures 2.1b, 2.1c, and 2.1d) than 2003. Significant rainfall develops over the continent during May of 1999, but it is weaker during 2003. Progressive shrinking of the oceanic precipitation during June occurs in 1999, but in 2003 it is less pronounced. The pre-jump continental precipitation during June of 2003 is stronger than that of 1999 and, as shown by the analysis below, this may be partly responsible for the earlier jump in 2003 (near June 23) when compared to that of 1999 (near July 10). This degree of interannual variability is also registered in the observational analyses (Sultan and Janicot 2003) and (Fontaine et al. 2006). They reported that the standard deviation of about 7-8 days when filtered series are used and when the series are unfiltered the standard deviation was found to be about 15 days. Under slightly different experimental set up Sijikumar et al. (2006) also verified MM5's ability to simulate the West African monsoon onset.

The monsoon jump is also manifested in the NOAA daily outgoing longwave radiation (OLR) data (Liebmann and Smith 1996), converted to cloud top temperature using the Stefan-Boltzmann relation. Figure 2.3a shows a time series for 1999, averaged between 10^oE and 10^oW, of the location of clouds with black body temperatures lower

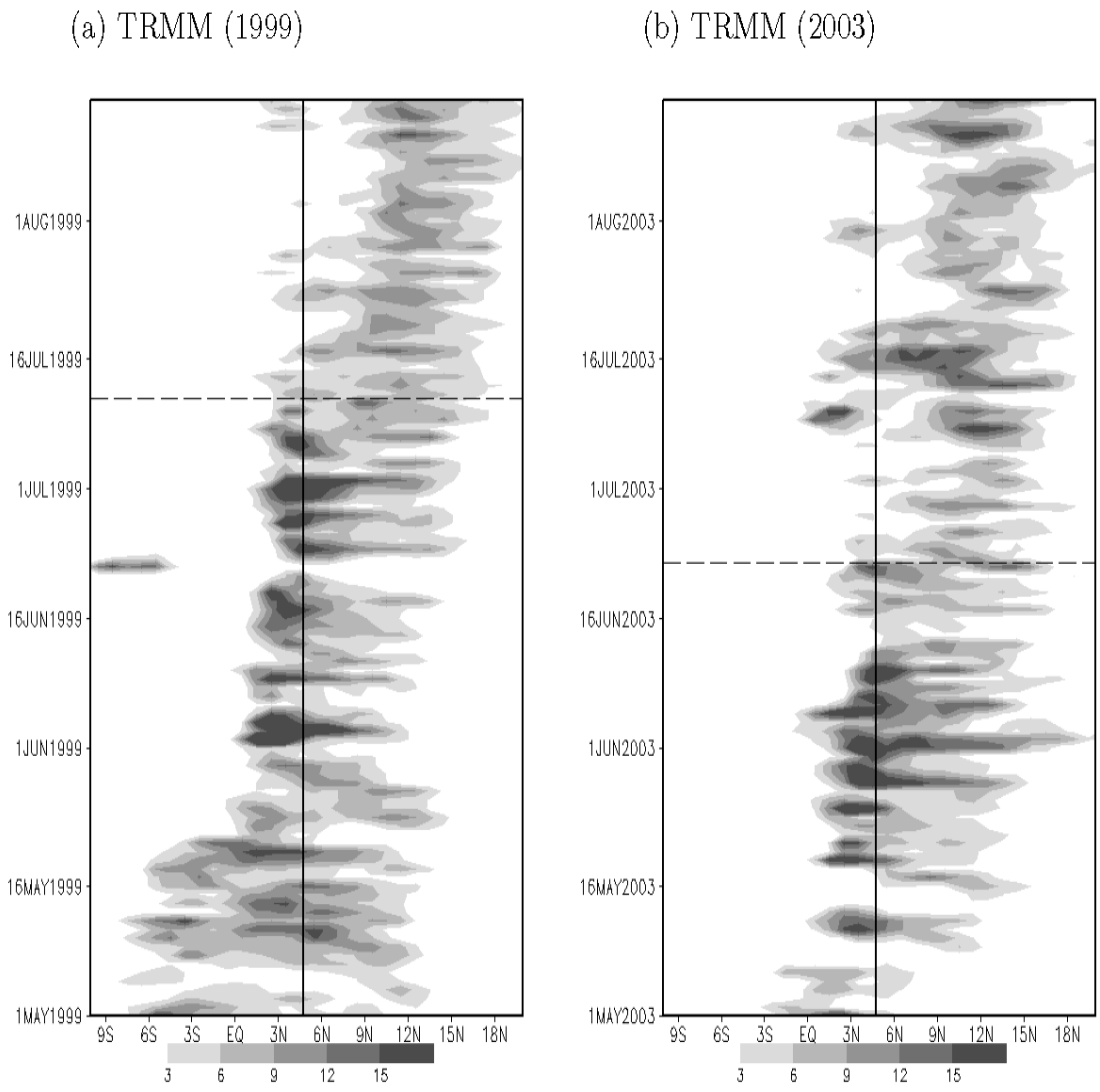

Figure 2.2: Precipitation from TRMM (3B42) for the years, (a) 1999 and (b) 2003. Both fields are averaged between 10^0E and 10^0W and are in mm/day. Dashed lines indicate approximate date of the monsoon jump and the bold lines represent the approximate latitude of the coastline.

than 240 K. This corresponds to pressure levels of approximately 300 hPa and above. Many of the features of the monsoon jump identified in the precipitation data and the model are reflected in the evolution of the high cloud distribution, including the narrowing of their latitude width from May to the end of June and the subsequent jump into the continental interior.

The OLR signal for black body temperatures of 240 - 260 K is shown in Figure 2.3b. This temperature range approximates the locations of lower clouds, while roughly filtering out emission from the surface and near-surface water vapor. There are indications of significant amounts of low clouds in the continental interior throughout the spring, but the jump is not apparent.

The monsoon jump occurs in the unique large-scale dynamics of the West African summer, and the RCM is able to capture that environment accurately. For example, May through July 925 hPa winds and geopotential heights from the model are compared with the NCEP/NCAR reanalysis (Kalnay et al. 1996) in Figure 2.4. Of particular relevance for the physics of the monsoon jump (discussed below) is the evolution of the continental low-pressure system and low-level flow. Comparison of the distance between the 780m and 760m geopotential height contours in the reanalysis shows that this low-pressure system intensifies as the season progresses. A similar increase in pressure gradients is also evident in the RCM (e.g., the distance between the 760m and 740m contours). As the low strengthens, the line of confluence between the southwesterly monsoon flow and the northeasterly Harmattan flow moves from about 15^0N in May to about 20^0N in July in both the reanalysis and the model simulation. The strong low-level southerly flow into the continent is in place during May and shows little variation as the season progresses. Further validation is also provided by Vizy and Cook (2002).

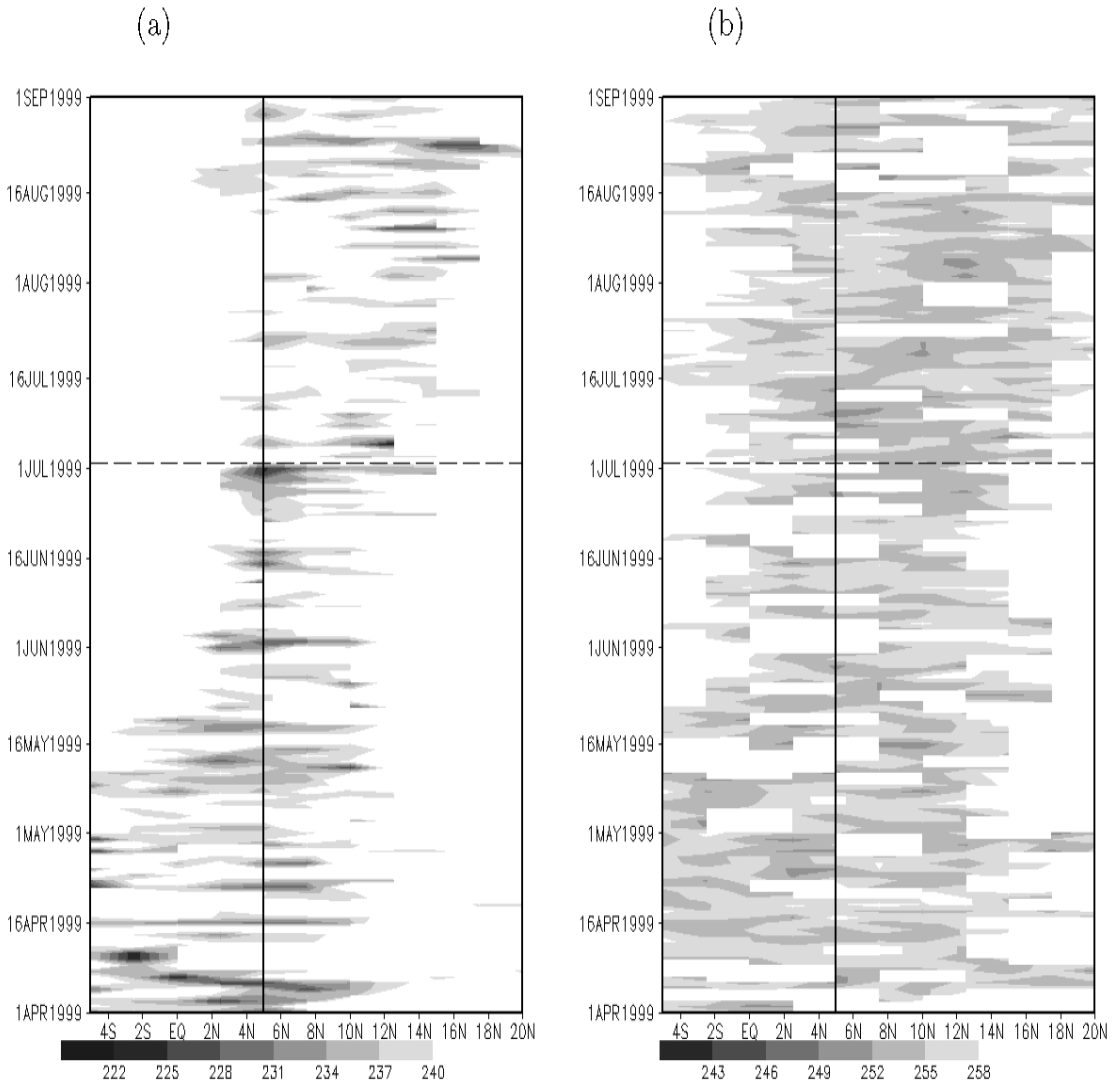

Figure 2.3: Black body cloud temperature (a) 220K to 240K and (b) 243K to 258K. Calculated from NOAA CDC outgoing long wave radiation data. Averaged between 10^0E and 10^0W. The bold line represents the approximate latitude of the coastline. The dashed line represents the approximate date of the shift of the temperature minimum into the continent.

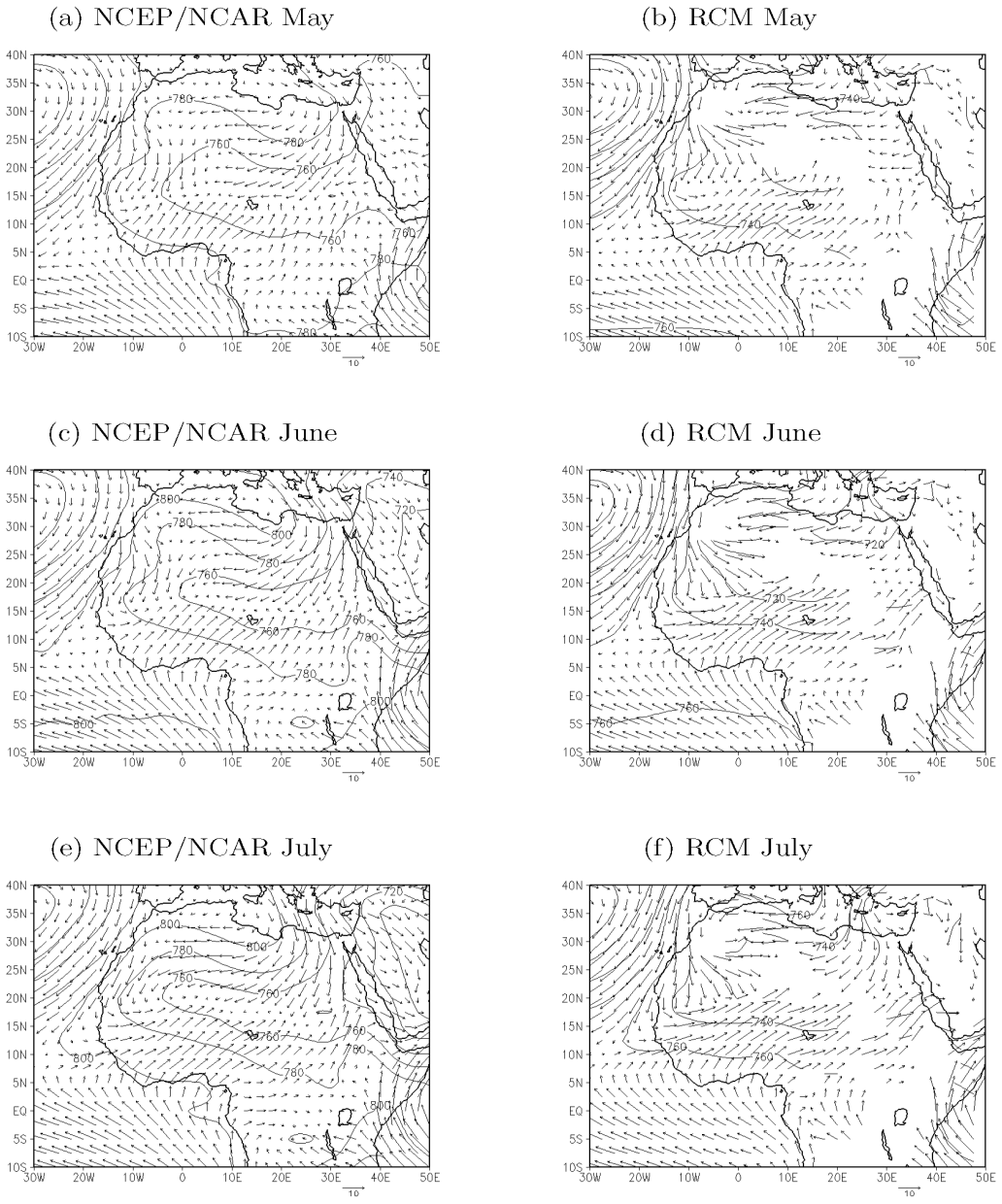

Figure 2.4: Monthly mean wind (m/s) and geopotential height (gpm) at 925 hPa from NCEP/NCAR reanalysis and RCM simulation.

2.4 Analysis

The vertical structure of the condensation field is considered because the OLR data presented in Figure 2.3 suggest that the monsoon jump involves an abrupt shift in upper tropospheric clouds. The free troposphere in the model can be classified into two layers in which the condensation field evolves in a distinct manner. Figures 2.5a and 2.5b show the development of the condensation field in the upper layer (above 525hPa) and the middle layer (825-525hPa), respectively.

Many features of the precipitation field (Figure 2.1a) are reflected in the upper layer condensation field (Figure 2.5a). The oceanic condensation field narrows throughout the pre-jump period and there is a marked discontinuity in its evolution near the time of the precipitation jump on June 25. Significant amounts of upper layer condensation (and precipitation) are present over the continent from the end of May through June. After the jump, the upper-level condensation follows the seasonal cycle deeper into the continent as in the precipitation and OLR observations.

The seasonal evolution of the middle-layer condensation is significantly different. It is established near 10^0N as early as the middle of May, and intensifies in the end of June. Its conspicuous absence along the coast and its early appearance suggest that it is mainly related to land surface processes.

The moisture, momentum and energy budgets of the system are analyzed to understand the relationship between processes in the upper and middle layers and their interactions with the boundary layer and the surface. A chronology of the entire process is given afterwards.

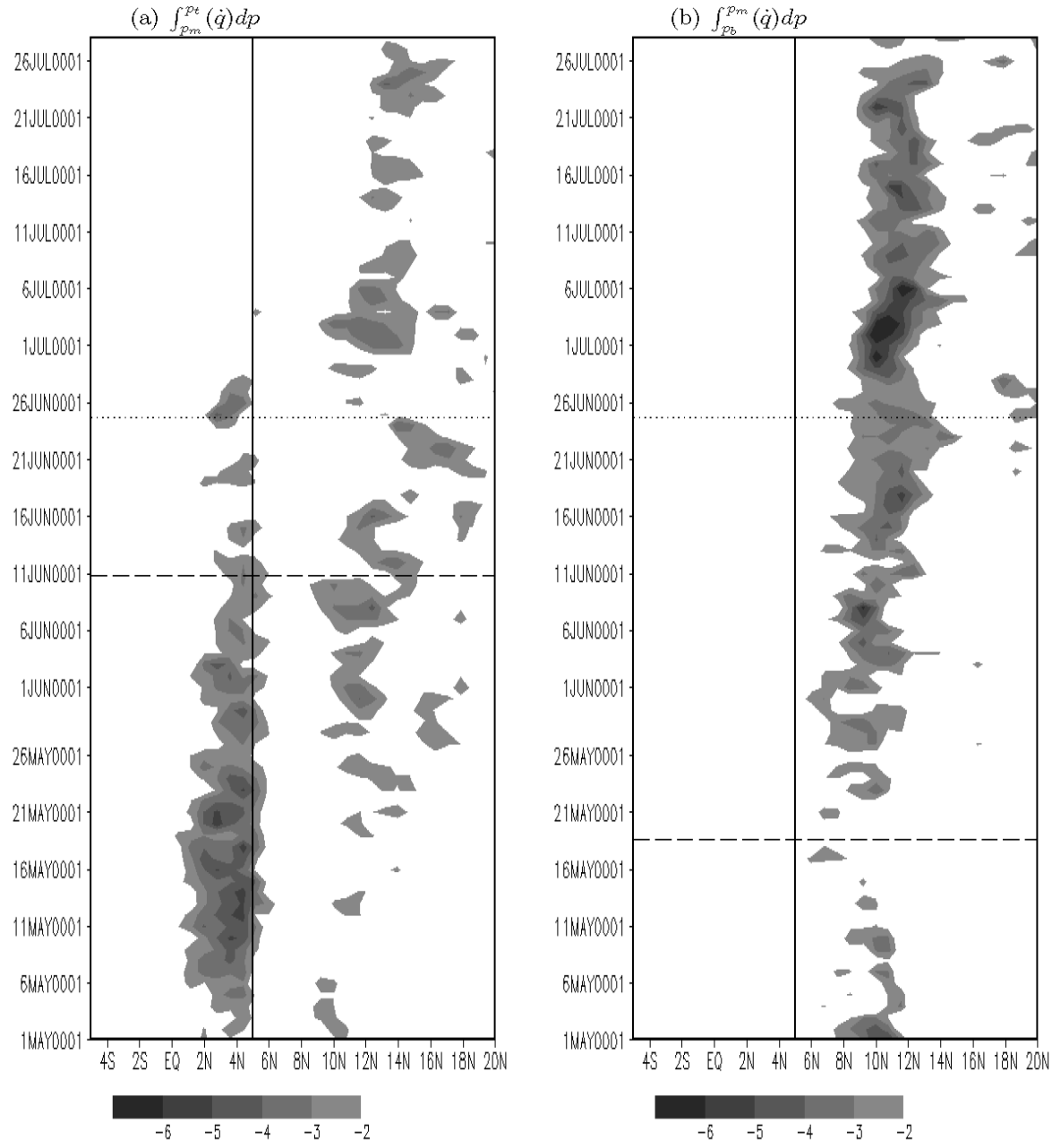

Figure 2.5: Vertical integral of moisture condensation between (a) between 525 hPa and 50 hPa and (b) between 825 hPa and 525 hPa in the model in mm/day, both are averaged between 10^0E and 10^0W. The bold line represents the approximate latitude of the coastline and the dashed lines represent the approximate dates of onset and the start of pre-onset precipitation (see text).

2.4.1 Monsoon jump processes

To isolate the physical processes responsible for the evolution of the upper layer condensation field, the moisture budget equation is integrated from the bottom of the layer at $p_m = 525hPa$ to $p_t = 50hPa$, given by

$$\int_{P_m}^{P_t}(\dot{q})dp = \int_{P_m}^{P_t}(\frac{\partial q}{\partial t})dp + \int_{P_m}^{P_t}(\frac{\partial uq}{\partial x} + \frac{\partial vq}{\partial y})dp - \omega q_{P_t} + \omega q_{P_m} + \int_{P_m}^{P_t} F_q dp \quad (2.2)$$

The left hand side of (2) is the net change in mixing ratio by evaporation and condensation (if negative) and the right hand side includes the local time rate of change, the zonal and meridional components of the moisture convergence, and the vertical fluxes. F_q is the sum of horizontal diffusion, vertical diffusion and the non-hydrostatic divergence of moisture.

Figures 2.6a and 2.6b display the vertical flux of moisture from the middle layer, $-\omega q_{Pm}$, and the horizontal convergence of moisture within the upper layer, respectively. These are the two largest contributors to the upper-level condensation. The sum of the other terms in (2.2) accounts for less than 10% of the total condensation. As marked by the dotted line in Figure 2.6a, the vertical moisture flux into the upper level over the continent (near 10^oN) begins on June 2. nearly 4 weeks before the monsoon jump (dashed line) in the simulation. From this time till the occurrence of the jump, two regions of vertical flux are maintained, reminiscent of a "double ITCZ" structure. After the jump, the vertical moisture flux along the Guinean coast falls below 2 mm/day within a week.

Between June 2 and June 25, a small horizontal moisture convergence helps to maintain the upper-level condensation along the Guinean coast (Figure 2.6b), and this term is also important during the second half of May in the continental interior.

The next step is, then, to identify the sources of moisture flux from the middle to the

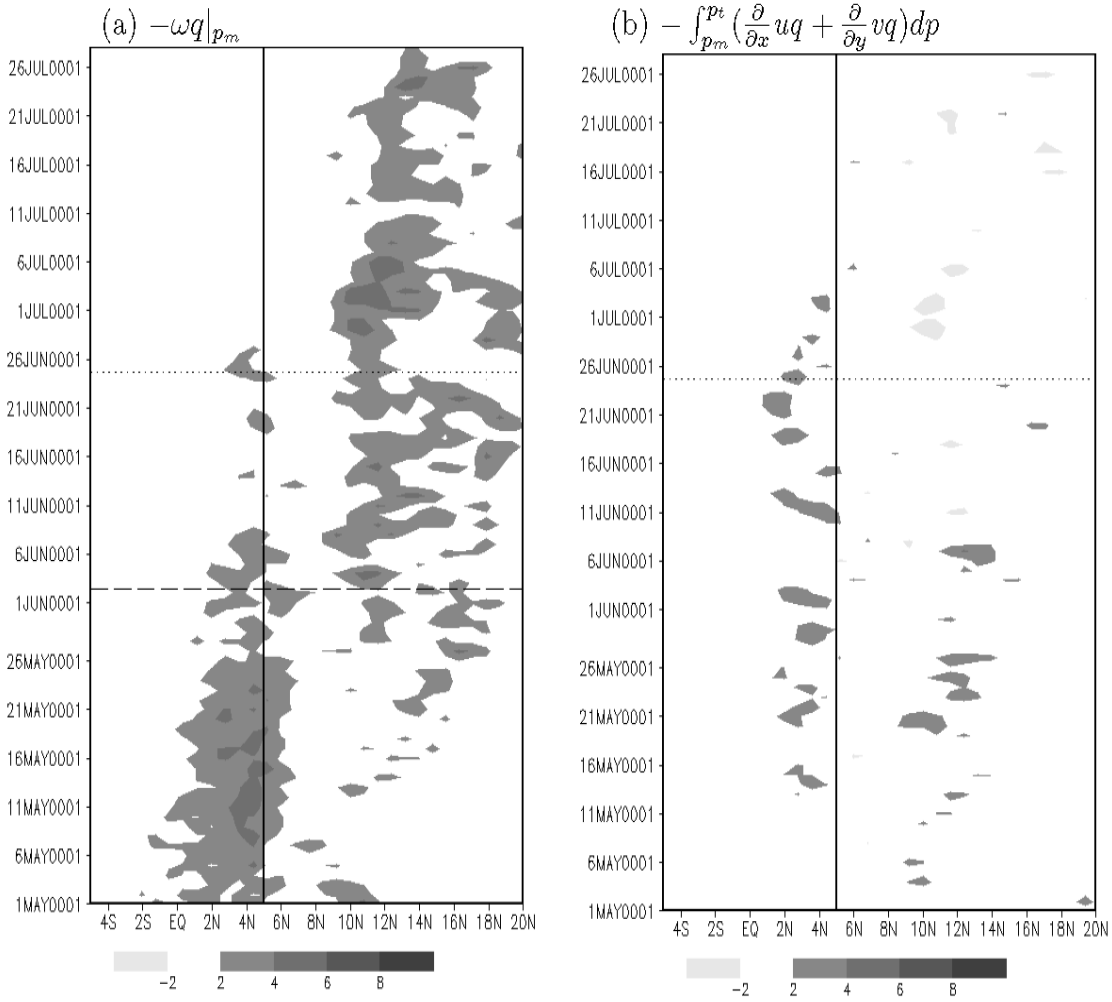

Figure 2.6: (a) Vertical moisture flux into the upper layer and (b) and convergence of moisture at the upper layer (mm/day). All are averaged between 10^0E and 10^0W. The bold line represents the approximate latitude of the coastline and the dashed lines represent the approximate dates of the appearance of vertical flux of moisture at N and the jump in the precipitation maximum (see text).

upper layer. The moisture budget for the middle-layer can be written as

$$\omega q_{P_m} = -\int_{P_b}^{P_m}(\frac{\partial}{\partial x}uq + \frac{\partial}{\partial y}vq)dp - \omega q_{P_b} + \int_{P_b}^{P_m}(\dot{q})dp - \int_{P_b}^{P_m}(\frac{\partial}{\partial t}q)dp - \int_{P_b}^{P_m} F_q dp \quad (2.3)$$

The left hand side, ωq_{P_m}, is the moisture flux between the middle and the upper-layer shown in Figure 2.6a, and the variables are defined as in (2.2). Figure 2.7 displays the first four terms from the RHS of (2.3). The last two terms are small. The shadings are changed relative to (2.2) for clarity, so that the sources of moisture in the middle level that supply the flux into the upper layer are positive (darker shading) and the sinks are negative.

The two main sources of moisture in the middle layer are meridional moisture convergence (Figure 2.7a) and the vertical flux from the boundary layer below (Figure 2.7b). The abrupt jump in deep convection and upper layer condensation around June 2 (Figure 2.6a) coincides with a similar jump in the middle layer meridional moisture convergence (dashed line; Figure 2.7a), but the vertical flux from the boundary layer is relatively constant throughout the season. This vertical flux is a source of moisture for the middle layer in the continental interior throughout the season.

Figure 2.7c shows that the zonal divergence of moisture significantly reduces middle layer moisture levels almost everywhere north of 4^oN, and is strong enough to compensate the meridional convergence of moisture at times. For example, in May, zonal divergence of moisture balances the meridional convergence of moisture just north of the Guinean coastline. In June, the strongest zonal divergence is located over the continental interior, but it does not completely compensate for the meridional convergence (Figure 2.7a). Condensation in this layer also weakens the vertical moisture flux (Figure 2.7d).

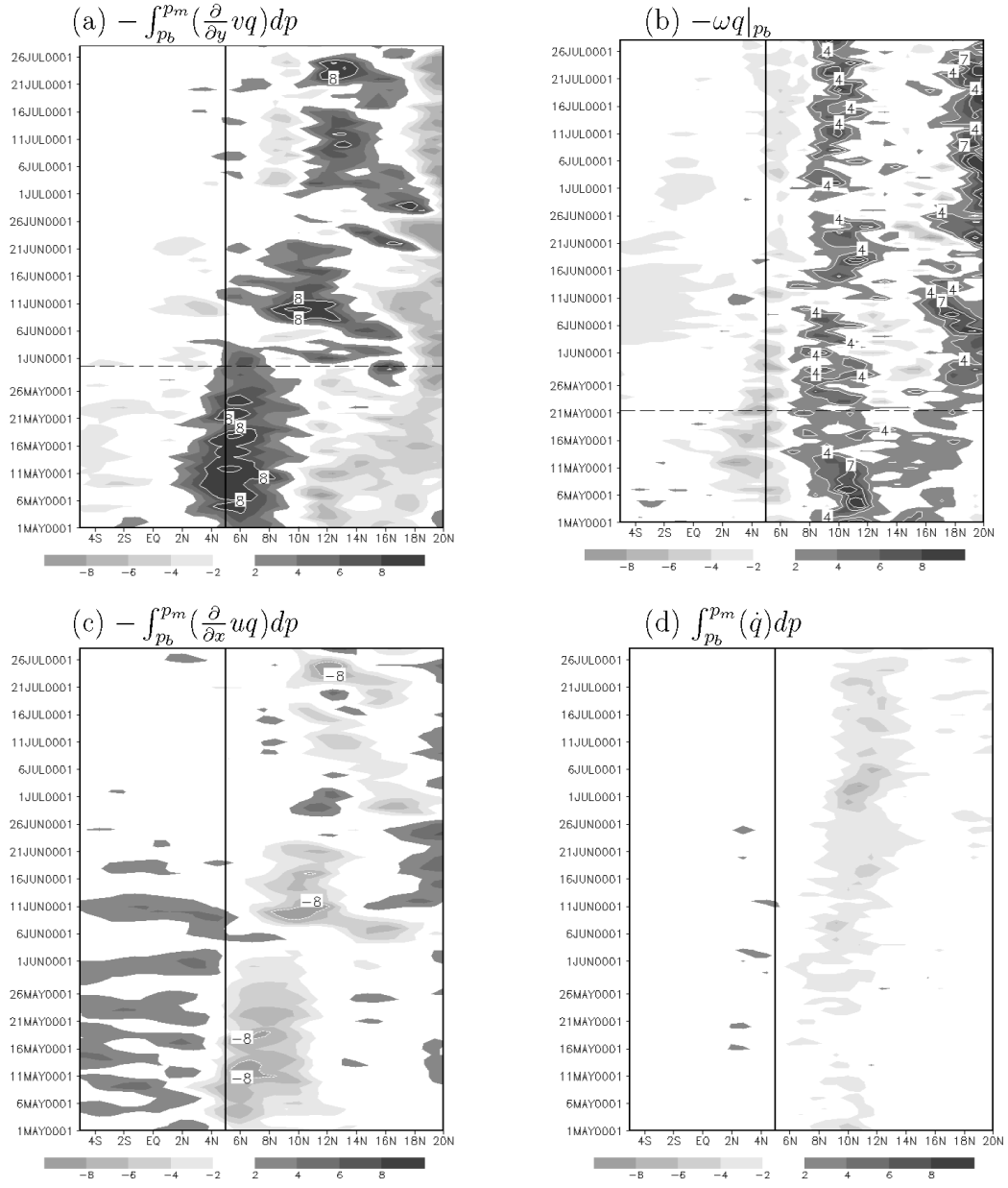

Figure 2.7: Sources and sinks of moisture for the middle layer (in mm/day). All are averaged between 10^0E and 10^0W. The bold line represents the approximate latitude of the coastline and the dashed line represents the approximate date of the appearance of middle layer moisture convergence at the continental interior.

The net moisture convergence in the middle layer can be decomposed as follows:

$$-\int_{P_m}^{P_b}(\frac{\partial}{\partial x}uq+\frac{\partial}{\partial y}vq)dp=-\int_{P_m}^{P_b}q(\frac{\partial}{\partial y}v)dp-\int_{P_m}^{P_b}q(\frac{\partial}{\partial x}u)dp \\ -\int_{P_m}^{P_b}u(\frac{\partial}{\partial x}q)dp-\int_{P_m}^{P_b}v(\frac{\partial}{\partial y}q)dp \tag{2.4}$$

Figures 2.8a and 2.8b show the evolution of the first two terms on the RHS of (2.4). Taken together, these two figures demonstrate that the meridional wind convergence accounts for almost all of the moisture convergence while zonal wind divergence is a major sink north of the coastline (Figure 2.8c). The third term in RHS of (2.4), the meridional advection of moisture, is only important near the northern edge of the continental regime where gradients in moisture distribution are significant, and the last term is negligibly small throughout (Figure 2.8d).

Figures 2.9a and 2.9b show the meridional and zonal wind convergence. Comparison of Figures 2.8a and 2.9a shows that evolution of the shift of the meridional moisture convergence from the coast into the continent is tied to a similar shift in the meridional wind convergence. The zonal moisture divergence near 10^oN is located at the southern edge of the African easterly jet and is related to the easterly acceleration of the flow across West Africa, which results in a net loss of moisture (Figure 2.9b). One important question is, then, why does the meridional convergence suddenly move into the continental interior on near May 30?

More general than (2.1), which assumes that the zonal flow is zonally uniform and geostrophic, perturbations are small, and friction, F_y, is negligible, the large-scale meridional flow is governed by the momentum equation

$$\frac{\overline{Dv}}{Dt}=-f\bar{u}-\frac{\partial\overline{\phi}}{\partial y}+\overline{F}_y \quad . \tag{2.5}$$

where the over bars indicate vertical averaging over the middle layer (825 hPa to 525 hPa). The left hand side term of (2.5) is displayed in Figure 2.10a, from the RCM sim-

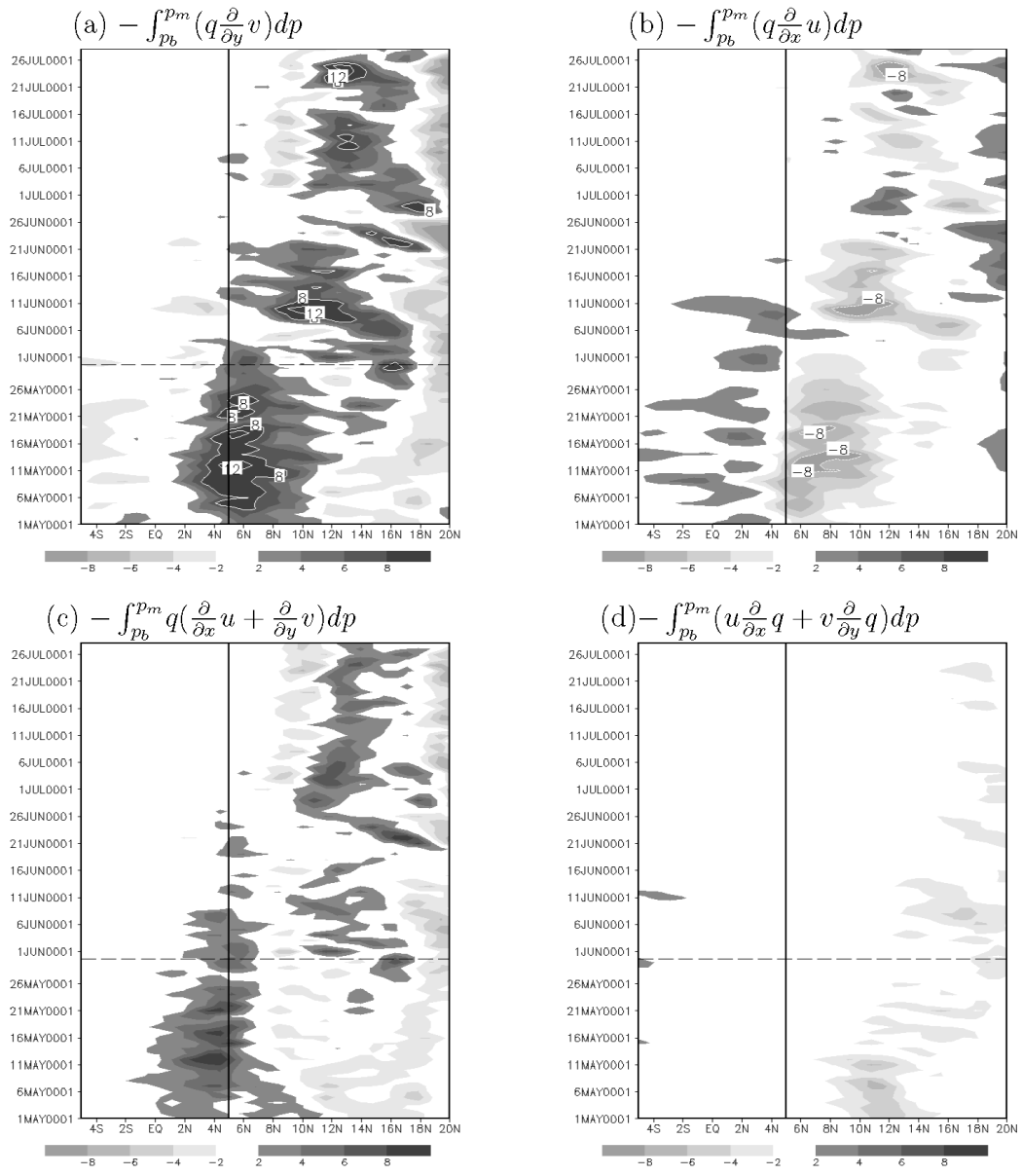

Figure 2.8: Components of the moisture convergence in the middle layer in mm/day. All are averaged over 10^0E and 10^0W. The bold line represents the approximate latitude of the coastline and the dashed line represents the approximate date of the shift of middle layer meridional moisture convergence into the continental interior.

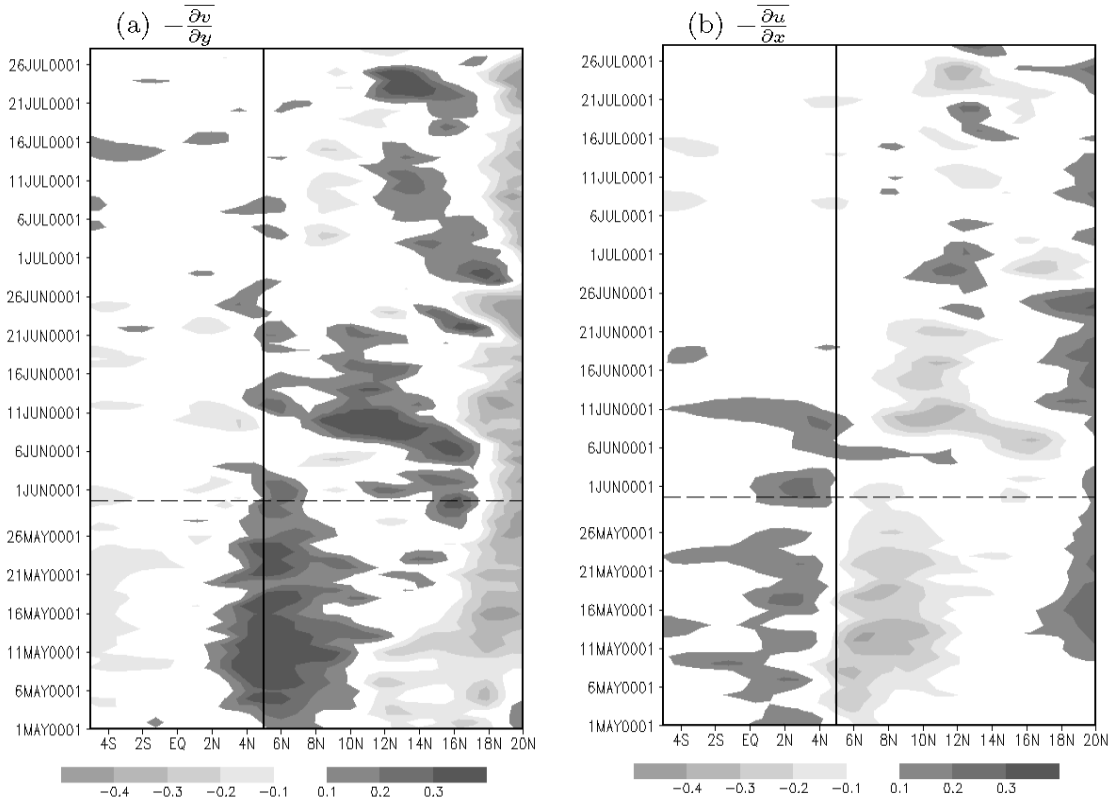

Figure 2.9: Components of the wind convergence in the middle layer (in mm/day) . All are averaged over 10^0E and 10^0W. The bold line represents the approximate latitude of the coastline and the dashed line represents the approximate date of the shift of middle layer meridional wind convergence into the continental interior.

ulation. To eliminate most of the 3 to 5 day fluctuations, the plot is smoothed using ten point running mean. During the last days of May, the sign of the meridional acceleration of parcels along the coastline changes from positive (northward) to negative (southward).

For example, in line with the idea of inertial instability, consider a parcel of air located at point X on the zero contour of acceleration (Figure 2.10a). Initially its acceleration is zero. Any northward displacement would move the parcel into a region of positive net force and cause it to accelerate further into the continent. Likewise, a parcel displaced southward is also accelerated further southward. Therefore, because of inertial instability the coastal region (the region surrounded by the contour of zero acceleration) becomes unfavorable for meridional convergence in the end of May and the meridional wind convergence jumps into the continental interior where convergence is sustainable.

Comparing Figure 2.10b, which shows the sum of the first two right hand side terms of (2.5), with Figure 2.10a indicates that the change in sign of the meridional acceleration is related to a change in the balance between the Coriolis and pressure gradient forces, while friction delays the process by about three days. Thus, the condition for northward acceleration and the associated shift in meridional convergence is a change in sign of $-f\bar{u} - \frac{\partial\overline{\phi}}{\partial y}$. For a geostrophic, zonally uniform flow, this condition can be simplified to the change in sign of absolute vorticity discussed in the background section. The significant meridional acceleration over both the ocean and the continent throughout the period of simulation, however, makes assumption of purely zonal flow during the pre-monsoon period questionable. The analysis is performed over a layer bounded by isobaric surfaces, therefore the distribution of geopotential height, $\overline{\phi}$, is related to the mean potential temperature of the layer, $\overline{\theta}$. To identify the mechanisms that control

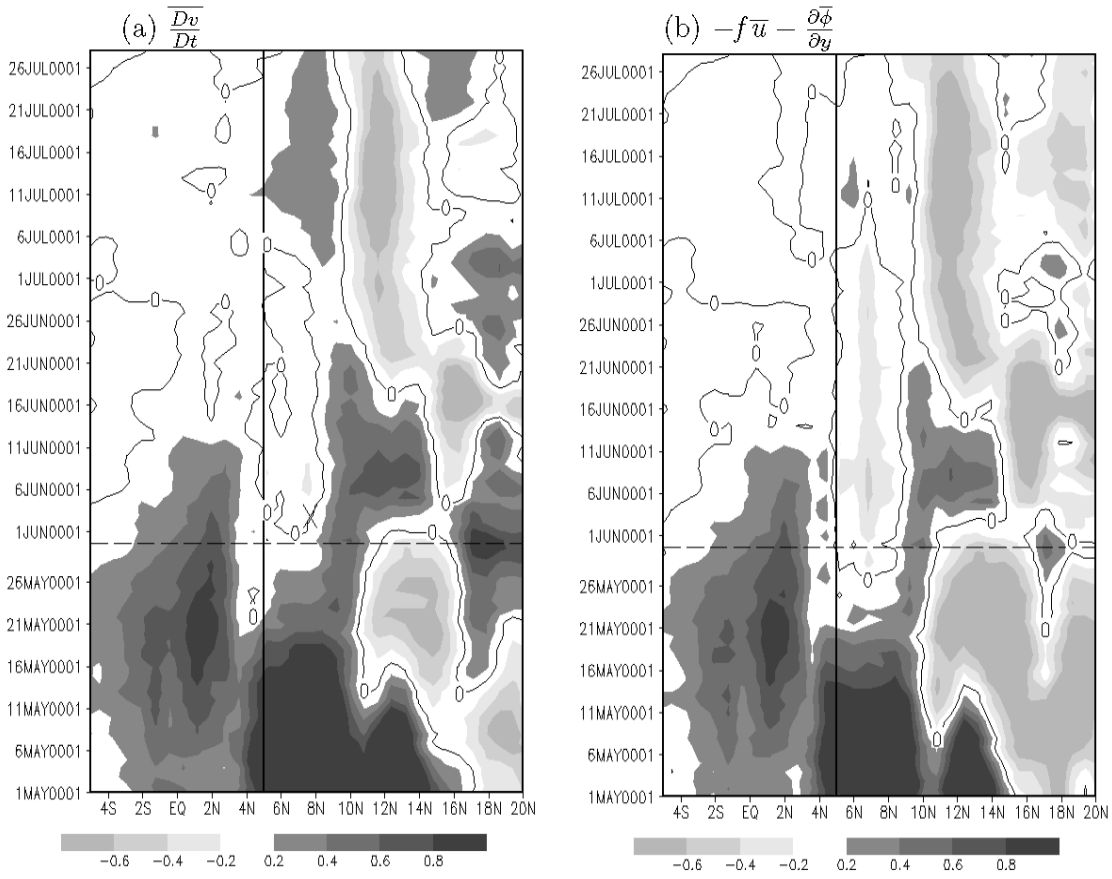

Figure 2.10: (a) Acceleration and (b) force in $10^{-4}ms^{-2}$. Both are averaged between 10^0E and 10^0W as well as 825 hPa and 525 hPa. The bold line represents the approximate latitude of the coastline and the dashed line represents the approximate date of the shift of middle layer meridional wind convergence into the continental interior.

potential temperature over the continent and the ocean, the pre-onset thermodynamic balance over the middle layer is considered, given by

$$\int_{p_b}^{p_m} \frac{D\theta}{Dt} dp = \int_{p_b}^{p_m} \left[\frac{\theta Q_r}{c_p T} + \frac{\theta Q_c}{c_p T} + \frac{\theta Q_d}{c_p T} \right] dp \quad . \tag{2.6}$$

The right hand side of (2.6) consists of the potential temperature tendencies due to radiative, condensational, and diffusive heating, respectively. The condensational and radiative heating terms are plotted in Figure 2.11a and b for the oceanic ($3 - 5^0$N) and continental regimes ($9 - 11^0$N) in the middle layer, respectively, along with the total potential temperature tendency. Diffusive heating is small and positive, as is expected for the free atmosphere. The values are smoothed by a ten-point running mean.

In both regions the supply of heat is mainly by middle layer condensation, with generally constant radiative cooling reducing the overall potential temperature tendency. Throughout May, condensational heating rates over the oceanic regime decline (Figure 2.11a) while those over the continent start to rise by the middle of May (Figure 2.11b). The central questions then are: what are the physical processes that govern the condensation in the middle layer? What makes the oceanic and continental mid-tropospheric condensation evolve in an opposite manner? These issues are discussed in the next sub-section.

2.4.2 Pre-monsoon jump processes

In the last subsection it was shown that the most important source of the heating that fuels the inertial instability is condensation in the middle layer within the continent. As shown in Figure 2.5b and 2.11b, this condensation starts increasing near the middle of May. In this section the mechanisms that control this increase in continental condensation through last two weeks of May are analyzed.

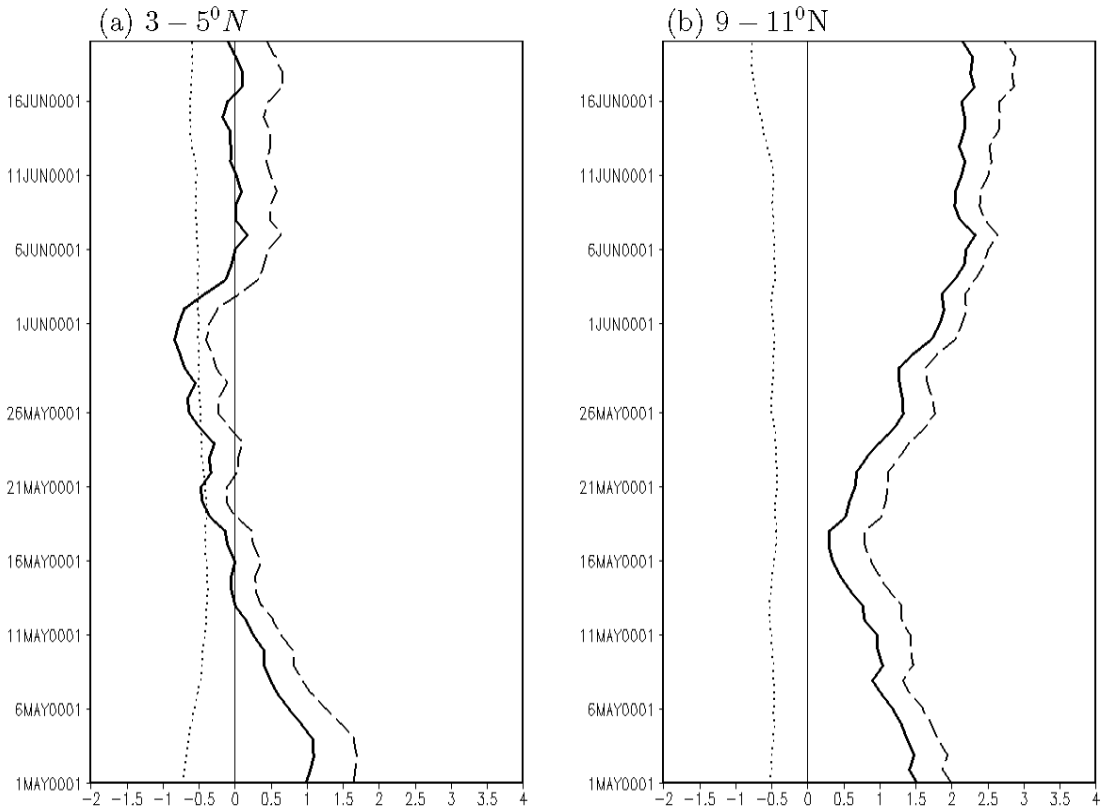

Figure 2.11: Sources and sinks of mean potential temperature tendency (in K/day) (a) along the coast (5^0N) and (b) in the continental interior (10^0N). The solid lines are total tendency, the dashed and dotted lines are condensational heating and radiative cooling, respectively. All are averaged over 10^0E and 10^0W.

The moisture budget equation in the middle layer, (2.3), can be rewritten as

$$\int_{P_b}^{P_m}(\dot{q})dp = \int_{P_b}^{P_m}(\frac{\partial}{\partial t}q)dp + \int_{P_b}^{P_m}(\frac{\partial uq}{\partial x} + \frac{\partial vq}{\partial y})dp + \omega q_{P_b} - \omega q_{P_b} + \int_{P_b}^{P_m} F_q dp \quad (2.7)$$

Continental condensation in May is controlled by the first three terms on the RHS, i.e., moisture flux from the boundary layer (Figure 2.7b) and divergence in the middle layer (Figure 2.8c) . Near the middle of the month, the gradually increasing moisture supply from the boundary layer becomes larger than the loss by divergence, and this leads to the onset of condensation in the middle layer on May 20 in the simulation. The other terms in (2.7) are relatively small.

In contrast, the roles of the boundary layer flux and moisture convergence in the middle layer are reversed along the coast. Here, the main source of moisture for the oceanic middle layer is meridional convergence (Figure 2.7a) and the net vertical moisture flux is directed downward into the boundary layer (Figure 2.7b). The sources of the moisture that converges along the coast are the upward boundary layer fluxes to the south and, especially, to the north of the precipitation maximum along the coast. Therefore, the boundary layer supplies moisture to the continental middle layer and deprives the oceanic region. In this way, boundary layer fluxes facilitate the processes that lead to the monsoon jump.

The moisture budget equation for the boundary layer can be written as

$$\omega q_{P_b} = -\int_{P_s}^{P_b}(\frac{\partial uq}{\partial x} + \frac{\partial vq}{\partial y})dp + \omega q_{P_s} + \int_{P_s}^{P_b}(\dot{q})dp - \int_{P_s}^{P_b}(\frac{\partial}{\partial t}q)dp - \int_{P_s}^{P_b} F_q dp \quad (2.8)$$

wherep_s is the pressure at the lowest model level. Over the ocean p_s is 995 hPa and over land it varies with topography. Figures. 2.12a and 2.12b show the zonal and meridional moisture convergence terms, respectively. The main source of moisture for the flux from the boundary layer into the middle layer within the continent (~10^oN-12^oN) is meridional moisture convergence (Figure 2. 12a). For the most part, the zonal flow

diverges moisture in this layer (Figure 2.12b). Fluxes from the surface also have a small positive contribution over the continental interior (not shown). The sum of the last three terms in (2.8) is important only where moisture gradients are relatively large (not shown).

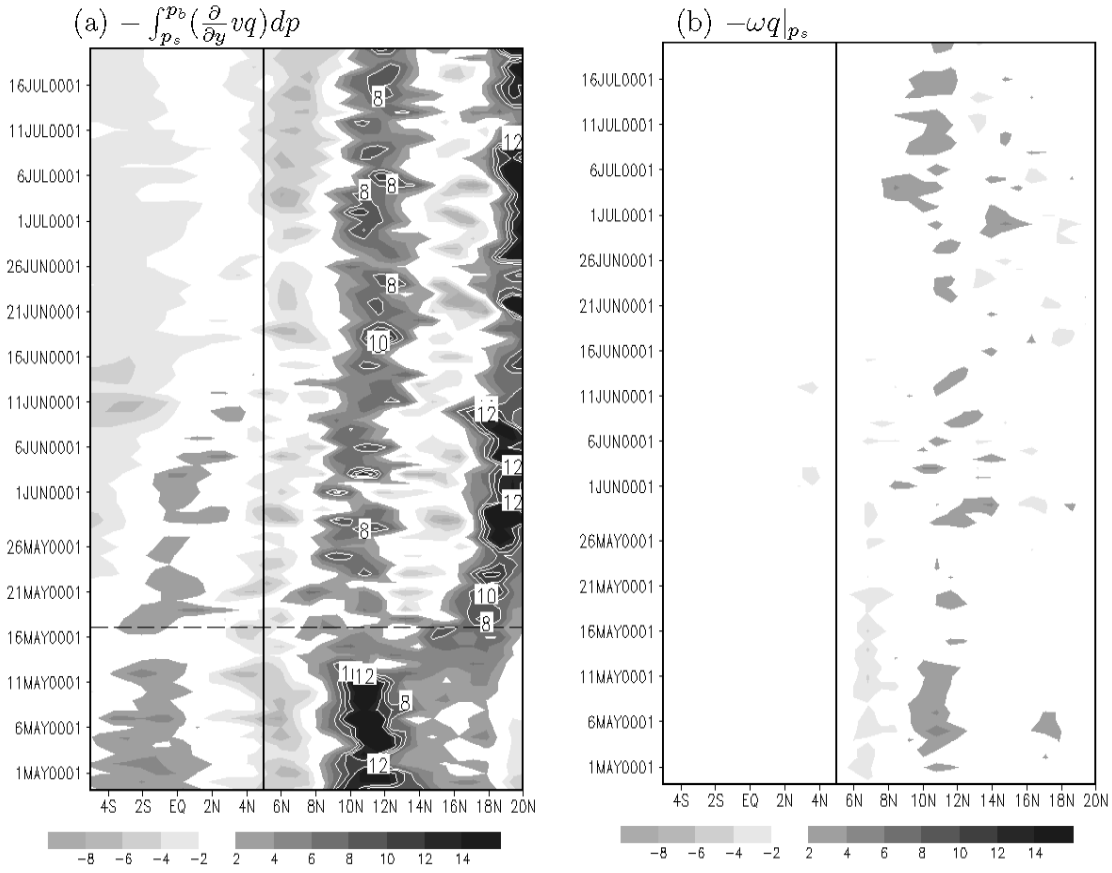

Figure 2.12: Sources and sinks of moisture in mm/day in the boundary layer. All are averaged between 10^0E and 10^0W. Solid lines represent the approximate latitude of the coastline.

The shallow meridional circulation that drives moisture into the continent well before the monsoon jump has recently been observed by Zhang et al. (2006). Using sounding data, they demonstrated that this circulation exists throughout the year. This

is consistent with our modeling result that the shallow meridional convergence at 10^0N exists throughout the period of simulation without significant variations (Figure 2.12a). They also observe that the monsoon onset is associated with the deepening of this otherwise boundary layer circulation. This is also consistent with our modeling result that during the monsoon season, the meridional moisture convergence extends well into the lower free troposphere (Figure 2.8a).

Having shown that the ultimate source of moisture (and heat) for the monsoon jump is meridional boundary layer convergence in the continental interior, the physical processes that control the evolution and the latitudinal location of this meridional convergence are investigated. The dynamics in the boundary layer is closely tied to the surface heat budget, which determines the amount of sensible heat transferred into the boundary layer. This supply of heat is balanced by the divergence of heat by the shallow circulation. For the time-scales of interest, sensible (Q_{sh}) and latent (Q_{lh}) heat fluxes from the surface approximately balance the sum of the net short wave (Q_{sw}) and long wave (Q_{lw}) radiative heating supplied into the surface

$$Q_{sh} + Q_{lh} \simeq Q_{sw} + Q_{lw} \quad . \tag{2.9}$$

Figure 2.13a shows the evolution of sensible heating, Figure 2.13b the net radiative heating, Figure 2.13c short wave heating only and Figure 2.13d the latent heat lost by the surface due to evaporation. The sensible heating maximum remains in the continental interior (10^0N) without significant latitudinal change (Figure 2.13a). The location of the sensible heating maximum is determined by two factors; Because of relatively low albedo the net shortwave radiation and the net total radiation have their maxima between 10^0N and 15^0N (Figure 2.13b and Figure 2.13c). But about half of this radiation input into the surface is used in evaporation, which has its local maxima values between 12^0N and 18^0N as well as south of 6^0N (Figure 2.13d). This introduces a sensible heating maximum between 6^0N and 12^0N, which is also the location of the pre-onset shallow

meridional convergence, the subsequent deep monsoon meridional convergence, deep convection and precipitation.

2.5 Summary of the process

The above discussion provides an analysis of the monsoon jump process. Based on this, one can construct the following summary of the process. The dates are approximate.

- Because of the distribution of albedo and surface moisture availability, a sensible heating maximum persists over the Sahel. This sensible heating drives a shallow meridional circulation and moisture convergence at that latitude. The moisture is transported upward into the middle layer, where it diverges (Figures 2.12a and 2.13a).
- During the second half of May, the increasing moisture flux from the boundary layer exceeds the divergence in the middle layer and results in a net supply of moisture and condensation (Figures 2.5b and 2.7b). This condensation warms up the continental middle layer, while the evaporation of rain and radiation cool the middle layer along the coast (Figure 2.11).
- The resulting pressure gradient results in an inertial instability, which abruptly shifts the meridional wind convergence maximum from the coast into the continental interior on around May 30. This introduces a net total moisture convergence, net upward moisture flux and condensation in the upper layer, and the enhancement of precipitation in the continental interior (Figures 2.10, 2.8, and 2.5a).
- During June, because of the shift of the meridional convergence into the continent

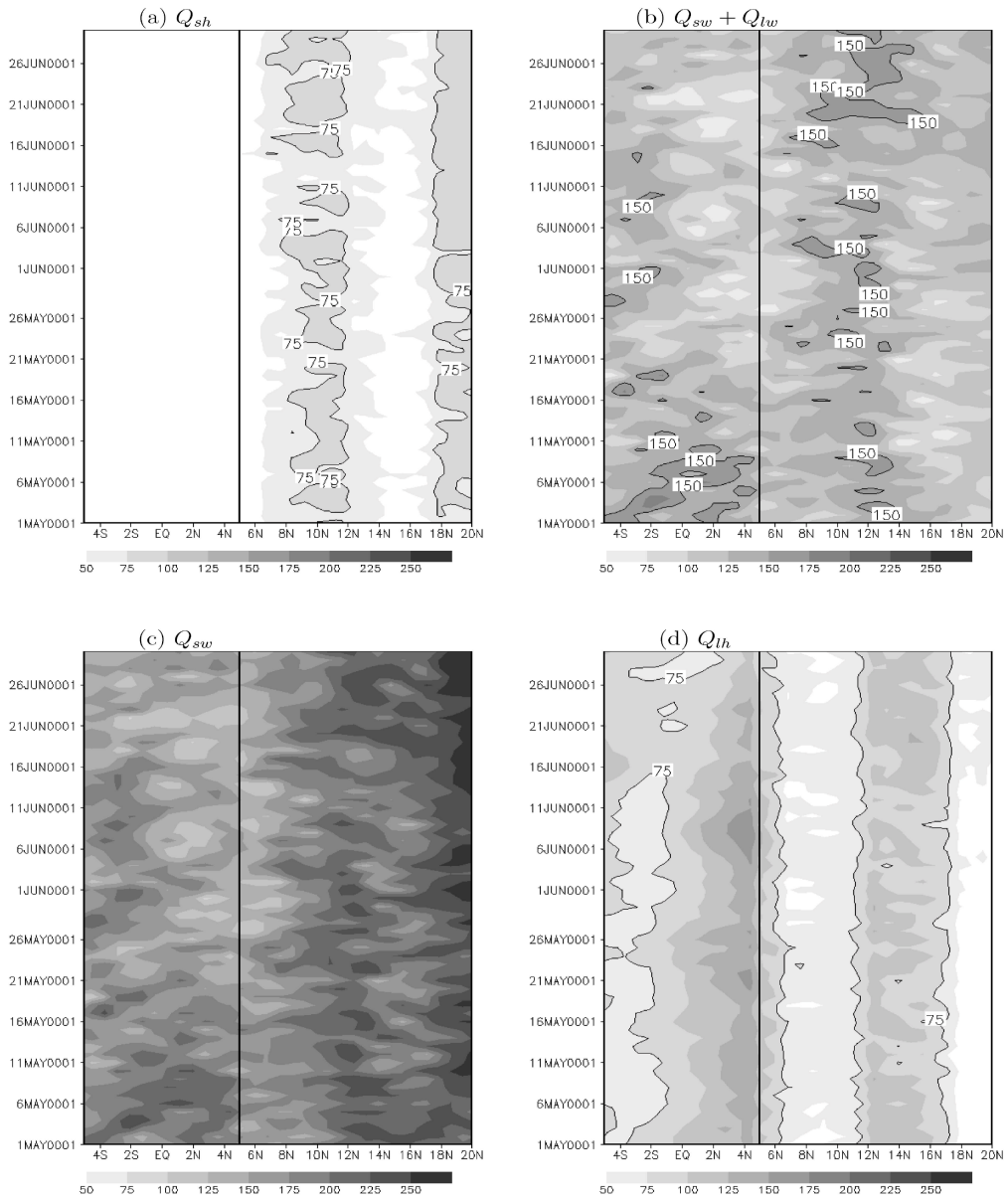

Figure 2.13: (a) Surface upward sensible heating, (b) net downward radiative heating, (c) net downward short wave heating and (d) net upward latent heating fluxes in . Solid lines represent the approximate latitude of the coastline.

and downward flux of moisture into the boundary layer, upper layer condensation and precipitation along the coast gradually disappear.

2.6 Discussion

The above modeling results agree to some extent with the previous observational analysis of Sultan and Janicot (2003), who also find that the West African monsoon jump involves the release of potential instability due to the supply of moisture by southerly surface winds followed by an inertial instability. In addition, our model agrees with their finding that surface heating drives the pre-onset moist southerly winds. However, in our model topography doesn't play a primary role in the process.

In their model simulations, Sijikumar et al. (2006) showed that the monsoon onset is characterized by a deepening of the heat low and accompanied by increased monsoon flow from eastern Atlantic. Our results agree with that except in our model, the abrupt change is in the depth of the predominantly southerly monsoon flow from the Gulf of Guinea.

The above-discussed processes of the monsoon onset are not unique to West Africa. A similar onset mechanism has also been observed in the South Asian monsoon. The South Asian monsoon circulation is known to be driven by heating above the boundary layer, while the pre-monsoon shallow circulation provides the moisture which in turn introduces inertial instability in the free troposphere (see Webster et al. 1998 and references therein).

This work extends the previous theoretical studies that suggest boundary layer entropy gradients are responsible for the onset of the monsoon. The change in the sign of

$-f\bar{u} - \frac{\partial\bar{\phi}}{\partial y}$ shown here to be the primary condition for the inertial instability reduces to the negative absolute vorticity condition that implies the breakdown of a strictly zonal geostrophic flow in the idealized systems described by Emmanuel (1995) and Eltahir and Gong (1996). In this case, however, the pre-onset system is not necessarily strictly zonal or geostrophic. In fact, the inertial instability owes its appearance to the ageostrophy of the system. By divesting moisture, zonal wind divergence plays a delaying role in the onset process. In our study, the pre-monsoon shallow meridional circulation, which is observed in atmospheric sounding study by Zhang et al. (2006), plays a very important role in transporting moisture from the ocean into the continent weeks before the onset of deep convection over the continent. Considering the contribution of the simple theoretical models to the improvement of prediction (Fontaine et al. 1999), one can hope to achieve even better skill by considering the above-discussed interactions among the boundary layer and the various layers of the free troposphere in future work on prediction.

In this study, the seasonal evolution of SST is prescribed. As noted in the background section, there are some modeling and observational results that suggest the monsoon has significant influence on SSTs in the Gulf of Guinea (e.g., Okumura and Xie 2004, Mitchell and Wallace 1992). This interaction should be further investigated using coupled models.

BIBLIOGRAPHY

[1] Blackadar, A. K. 1979: High-resolution models of the planetary boundary layer, *Adv. Environ. Sci. Eng*., **50** 85, 1979.

[2] Eltahir, E. A. B., Gong, 1996: Dynamics of wet and dry years in the West Africa. *.J.Clim.* **9** 1030-1042

[3] Emanuel, K. A., 1995: On thermally direct circulations in moist atmospheres. *J. Atmos. Sci.* **52** 1529-1534

[4] Fontaine, B, N. Philipon and P. Chamberlin, 1999: An improvement of June-September rainfall forecasting in the Sahel based upon April-May moist static energy content (1968-1997). *Geophys. Res. Lett* **26** 2041-2044.

[5] Fontaine B., and S. Louvet 2006: Sudan-Sahel rainfallonset: Definition of an objective index, types of years, and experimental hindcasts. *J. Geophys. Res*., **111** doi:1029/2005JD007019, 2006.

[6] Gu, G. and R. Adler, 2004: Seasonal evolution and variability associated with the West African Monsoon System. *J. Clim.* **17** 3364-3377

[7] Joseph, J.H., W.J. Wiscombe, and J.A. Weinman, 1976: The delta-Eddington approximation for radiative flux transfer. *J. Atmos. Sci.,* **33**, 2452-2459.

[8] Kain, John S. and J. M. Fritsch. 1990: A One-Dimensional Entraining-Detraining Plume Model and its Application in Convective Parameterization. *J. Atmos. Sci.,* **47**, 23, pp 2784 - 2802.

[9] Kalnay, E. M, and others, 1996: The NCEP/NCAR 40-year reanalysis project. *Bull. Amer. Meteor. Soc.* **77** 437- 471

Kiehl, J.T., and B.P. Briegleb, 1991: A new parameterization of the absorptance due to the 15-micron band system of carbon dioxide. *J. Geophys. Res*., **96**, 9013-9019.

[10] Le Barbe, L., T. Lebel, and D.Tapsoba, 2002: Rainfall variability in the West Africa during the years 1950-1990. *J.Clim.* **15** 187-202

[11] Lebel, T., A. Diedhiou, and H. Laurent, 2003: Seasonal cycle and interannual variability of the Sahelian rainfall at hydrological scales. *J. Geophys. Res.- Atmos*., **108**, 8389, doi: 10.1029/2001JD001580.

[12] Liebmann, B., and C. A. Smith, 1996: Description of a complete (interpolated) outgoing longwave radiation dataset. *Bull. Amer. Meteor. Soc*., **77**, 1275-1277.

[13] Mitchell T. P., and J. M. Wallace 1992: The Annual Cycle in Equatorial Convection and Sea Surface Temperature. *J.Clim.* **5** 10 1140–1156.

[14] Neelin, J. D., C. Chou, and H. Su, Tropical drought regions in global warming and El Niño teleconnections, *Geophys. Res. Lett*., **30** (24), 2275, doi:10.1029/2003GL018625, 2003

[15] Nicholson S. E., Coauthors, 2003: Validation of TRMM and other rainfall estimates with a high-density gauge dataset for West Africa. Part I: Validation of GPCC rainfall product and pre-TRMM satellite and blended products. *J. Appl. Meteor.*, **42**, 1337–1354

[16] Nicholson, S. E., 2003 Validation of TRMM and other rainfall estimates with a high density gauge data datasets for West Africa. Part II: validation of TRMM products. *J. Appl. Meteor., **42**, 1355-1368*

[17] Okumura, Y. and S. Xie 2004: Interaction of the Atlantic equatorial cold tongue and the African monsoon. . *J.Clim.* **17** 3589-3601.

[18] Ramel, R., H. Gallee, C. Messager 2006: On the northward shift of the West African monsoon *Climate Dynamics 26: 429-440*

[19] Sijikumar S., P. Roucou, and B. Fontaine 2006: Monsoon onset over Sudan-Sahel: Simulation by a regional scale model MM5. *Geophys. Res. Lett*., 33, L03814, doi 10.1029/2005GL024819,2006.

[20] Sultan, B., and S. Janicot, 2000: Abrupt shift of the ITCZ over West Africa and intra-seasonal variability. *Geophys. Res. Lett.*, **27**, 3353-3356.

[21] Sultan, B and S. Janicot, 2003: The West African monsoon dynamics. Part II: The ”preonset” and ”onset” of the summer monsoon. *J.Clim.* **16** 3407-3427.

[22] Vizy, E. K., and K. H. Cook, Development and application of a mesoscale climate model for the tropics: Influence of sea surface temperature anomalies on the West African monsoon, *J. Geophys. Res.- Atmos*., **107** (D3), 10.1029/2001JD000686, 2002.

[23] Webster, P. J., and coauthors 1998: Monsoons: Processes, predictability and prospects for prediction. *J. Geophys. Res.- Atmos*., **103**(C7), 14,451 14,510,1998.

[24] Xie, P., and P. A. Arkin, 1996: Global precipitation: a 17-year monthly analysis based on gauge observations, satellite estimates, and numerical model outputs. *Bull. Amer. Meteor. Soc*., **78**, 2539-2558.

[25] Zhang, C., P. Woodworth and G. Gu, 2006: Seasonal cycle in the lower troposphere over West Africa in sounding observations. 132, 2561-2584 *Quart. J. Roy. Meteor. Soc.*,

Chapter 3

Ocean Warming and Late 20^{th} Century Sahel Drought and Recovery

Abstract

The influences of decadal Indian and Atlantic Ocean SST anomalies on late 20^{th} century Sahel precipitation variability are investigated. The results of this regional modeling study show that the primary cause of the 1980s Sahel drought is divergence and anomalous anticyclonic circulation associated with Indian Ocean warming. The easterly branch of this circulation drives moisture away from the Sahel. By competing for the available moisture, concurrent tropical Atlantic Ocean warming enhanced the areal coverage of the drought. The modeled partial recovery of the precipitation in the 1990s simulations is mainly related to warming of the northern tropical Atlantic Ocean and an associated cyclonic circulation that supplies the Sahel with moisture. Because of the changes in the scale and distribution of the forcing, the divergence associated with the continued Indian Ocean warming during 1990s was located over the tropical Atlantic, contributing to the recovery over the Sahel. In general, the influence of SSTs on Sahel precipitation is related to their modulation of the easterly flow and the associated moisture transport. Precipitation anomalies are further enhanced by the circulation patterns associated with local convergence anomalies. These convergence anomalies and circulation patterns are sensitive to the scale and distribution of the SST anomalies and the moisture.

3.1 Introduction

One of the most prominent signals of decadal precipitation variability of the 20^{th} century was observed over the Sahel region of Africa (Ward 1998). This region, which extends from Senegal coast to the Ethiopian highlands and roughly between 10^0N and 20^0Nlatitudes, suffered widespread droughts through the 1970s and 1980s with major economic and social consequences to the population of the region. In the 1990s, there was a partial recovery, bringing annual rainfall rates up to the climatological mean in the central and eastern Sahel. This recovery persists through the early years of this decade as well.

Figure 3.1a shows the difference between the 1980-1989 mean and the 50-year precipitation climatology obtained from the University of East Anglia's Climate Research Unit (CRU TS 2.1) precipitation data set (Mitchell and Jones 2005). It shows widespread drought across the Sahel. Comparison with the magnitude of the climatology indicates about 40% of the climatological value. Similarly, Figure 3.1b displays the difference between the 1990-1999 mean precipitation and the 50 year climatology, showing that precipitation in the 1990s over the central and eastern Sahel was similar to the climatology. The recovery is even more apparent when the mean precipitation of the 1990s and 1980s are compared. Figure 3.1c shows the difference between these two decades.

Because of the devastating effects on the population of the region, Sahelian drought has been the subject of great concern and extensive research for more than 30 years. In general, studies have progressed along two competing lines (Brooks 2004). The first one emphasizes localized feedbacks between land surface degradation and atmospheric radiation. According to these studies (e.g., Charney 1975), an increase in surface albedo due to human-induced change in vegetation decreased the precipitation, which in turn,

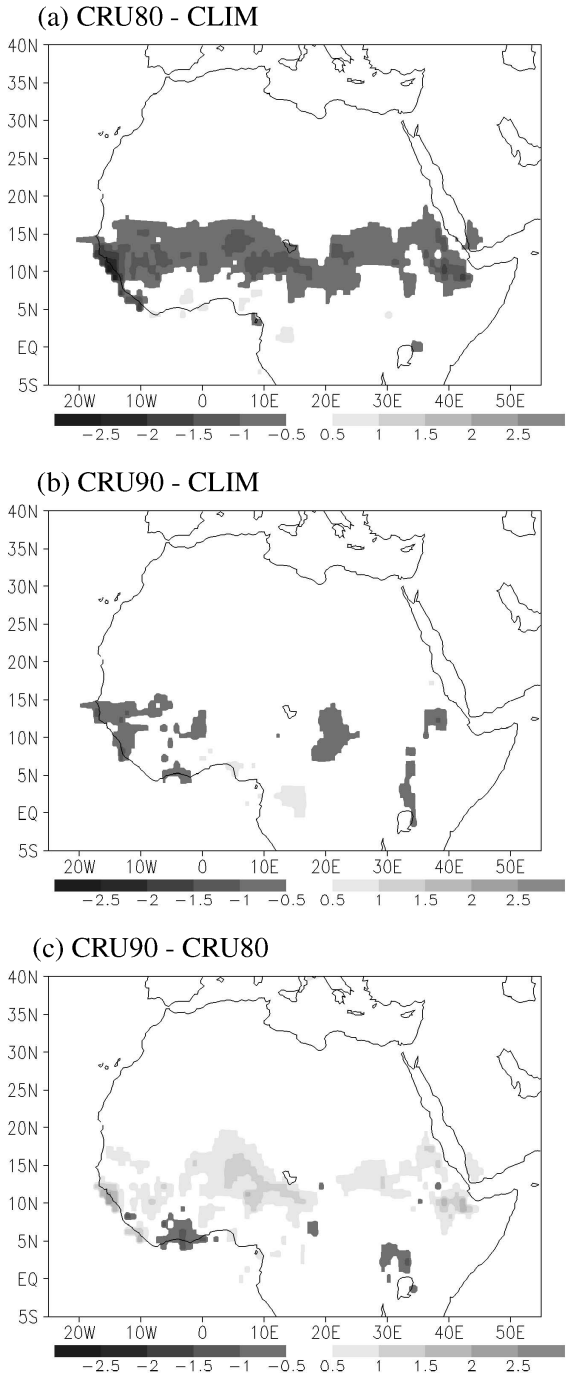

Figure 3.1: JAS precipitation (mm/day) from CRU TS 2.1 (a) 1980s minus climatological, (b) 1990s minus climatological and (c) 1990s minus1980s.

led to decreased vegetation and further increased surface albedo. Some recent studies challenge this hypothesis on the ground that many of the modeling studies used to support it exaggerated the prescribed land use changes. They suggest the observed changes in land surface conditions were more a consequence of the low precipitation rates than a cause of the drying (Taylor et al. 2002). On the other hand, using a coupled atmosphere-vegetation model, Zeng et al. (1999) show this land-surface feedback amplifies the precipitation response to decadal scale SST variability.

In the mid 1980s and afterwards, modeling and observational analysis studies revealed an association between observed Sahel rainfall variability and tropical Atlantic Ocean SSTs (Folland et al. 1986, Palmer 1986, Rowell et al. 1995). Giannini et al. (2003) showed that the NSIPP1 atmospheric GCM forced by observed SSTs from 1930 to 2000 captures decadal scale variability similar to the observed over the Sahel and identified the Indian Ocean and, to a lesser extent, tropical Atlantic Ocean SSTs as the primary forcing of decadal scale Sahel precipitation variability. Using the ECHAM4 atmospheric GCM, Bader and Letif (2003) as well as Lu and Delworth (2005), using the CM2 GFDL atmospheric GCM, agreed that the primary influence is Indian Ocean warming. In contrast, using an ensemble of 18 GCMs, Hoerling et al. (2006) suggested cooling in the northern tropical Atlantic Ocean and concurrent warming over southern tropical Atlantic is the primary cause of this decadal variability.

The purpose of this study is to evaluate the physical processes responsible for the Sahel droughts of the 1980s and the partial recovery of the 1990s. It is important to understand the physics of the relationship between regional SSTAs and Sahel rainfall to improve our ability to predict for this region. For example, if the Sahel droughts of the 1970s and 1980s are indeed caused by warming in the Indian Ocean, then why was there a partial recovery in Sahel precipitation in the 1990s and early 2000s as the Indian

Ocean continues to warm? Is the large spread in predictions of future Sahel rainfall from state-of-the-art coupled GCMs (Cook and Vizy 2006) due to a spread in simulations of future SSTs, or to an inability of the GCMs to capture the forced response to given SST distributions. If we know the physical processes responsible for precipitation variability, then we will be better able to evaluate predictions of 21^{st} century precipitation from coupled GCMs.

3.2 Description and evaluation of model and experiments

In this study we use regional climate model simulations forced by observed SSTs in the ocean basins adjacent to the African continent. SSTs derived from the 50 year climatology and the decadal means (1980s and 1990s) over the Atlantic and Indian Oceans are applied individually and in concert. Since the model captures the precipitation differences of the two decades from the climatology, the dynamical analysis reveals the reason for the dry conditions of the 1980s and the recovery in the 1990s.

3.2.1 Model description and simulation design

The tropical regional climate model (RCM) used in this study is an adaptation of the PSU/NCAR MM5-V3 (Grell et al. 1994), modified as in Vizy and Cook (2002). The model is non-hydrostatic and solves the equations governing horizontal and vertical momentum, temperature, pressure, moisture, and liquid water equations on σ surfaces. The model simulations are run over a rectangular domain enclosed by 49^0E to 100^0W and 47^0S to 47^0N (Figure 3.2). The grid spacing of 135 km used in these simulations allows for resolution of the important surface and precipitation features, over a domain

large enough to cover the whole continent and tropical and subtropical regions of both tropical oceans. There are 23 vertical σ levels and the model time step is 90 seconds. The top of the atmosphere is fixed at 50 hPa for this tropical application and an upper radiative boundary condition is used. The effects of snow cover are neglected.

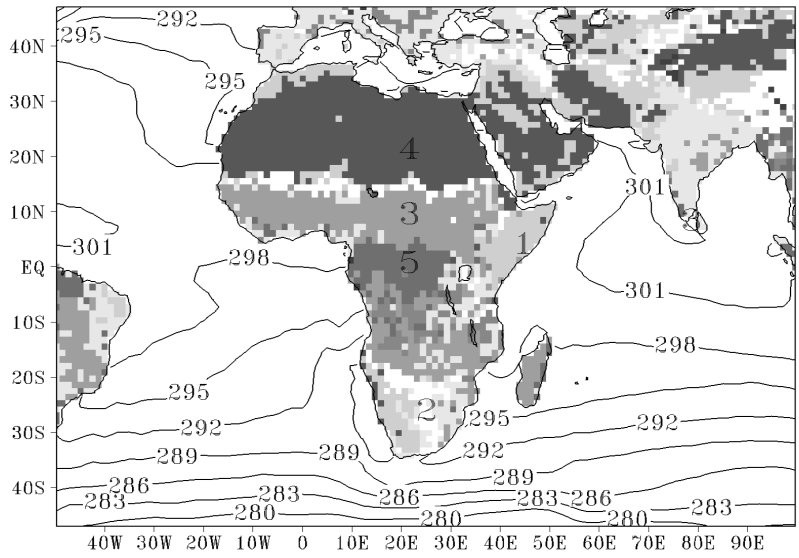

Figure 3.2: Simulation domain with JAS mean of the prescribed SSTs (K) and the vegetation distribution. The numbers indicate USGS vegetation categories as follows: 1 = shrubland, 2 = grassland, 3 = savanna, 4 = desert, 5 = evergreen (rain) forest.

The Kain-Frisch scheme (Kain and Frisch 1990) is used to parameterize convection. The closure assumes that the convective available potential energy is almost entirely removed at every time step at which convection occurs. This scheme incorporates the effects of entrainment and detrainment as well as downdrafts associated with evaporation of rain on the convection and large-scale environment and it produces realistic precipitation distributions over northern Africa in summer (Vizy and Cook 2002).

The Medium Range Forcasting (MRF) scheme (Troen and Mahrt, 1986) represents boundary layer processes. NOAH land surface model (Mitchell et al. 2002) is used for the interaction of the boundary layer with the surface. It is set to calculate soil moisture and temperature at depths of 10 cm and 200 cm. The NOAH LSM is initialized by soil moisture and temperature fields at the two levels from the NCEP/NCAR Reanalysis Project (NNRP hereafter, Kalnay et al. 1996).

The radiation scheme is adapted from that of the NCAR Community Climate Model 2. Its shortwave scattering/absorption is parameterized by the δ-Eddington approximation (Joseph et al. 1976) and is applied over 18 spectral intervals. The short-wave optical properties of the clouds depend on droplet size and the liquid water path. The scheme treats longwave absorption by ozone and CO_2 using the broadband absorption technique of Kiehl and Briegleb (1991). Longwave broadband emissivity of clouds is a negative exponential function of liquid water path.

A total of seven simulations are performed (see Table). In the control simulation (CTL hereafter), the annual SST cycle is obtained by averaging observed monthly mean SSTs from 1950 to 1999 from the NNRP (Reynolds and Smith 1995). These monthly mean SSTs are linearly interpolated into a 12-hourly time series as they are fed into the model. Values for the JAS average are displayed in Figure 3.2. In a similar manner, initial, lateral and land surface boundary conditions are obtained from the monthly mean NNRP climatology. The summer vegetation data is obtained from the USGS, and shown in Figure 3.2 at the resolution of the model.

SSTs for the decadal simulations of the 1980s and 1990s are calculated in a similar manner. As detailed in Table 1, these SSTs are applied throughout the model domain and in the Atlantic and Indian Ocean basins separately. All lateral, initial, and land surface boundary conditions, as well as the physical parameterizations are the same for

all the experiments.

This procedure filters out interannual SST variability, and the simulation design excludes influence from the Pacific Ocean. This is appropriate because previous work (Giannini et al. 2003) suggests that influence from the Pacific is mainly interannual. The simulation design is intended to isolate the decadal signal, enabling higher resolution modeling that captures the dynamics of the system accurately in a computationally efficient manner.

In order to evaluate the performance of the model, the JAS mean precipitation from CTL (Figure 3.3a) is compared with precipitation fields from three observational data sets (Figures 3.3b and 3.3c). Each precipitation field presented has been interpolated to a 1^0 x 1^0 grid. Figure 3.3b shows the JAS 1998-2004 mean precipitation from the Tropical Rainfall Measuring Mission (TRMM 3B42V5). This is a blend of microwave and infrared precipitation estimates scaled to monthly rain gauge measurements (Adler et al. 2004). The 1998-2004 JAS mean precipitation climatology from the Global Precipitation Climatology Project (GPCP) is shown in Figure 3.3c. The data set is derived from rain gauge measurements merged with satellite estimates of rainfall (Huffman et al. 1997). In Figure 3.3d the 1950-1999 JAS precipitation climatology from the University of East Anglia's Climate Research Unit (CRU TS 2.1; Mitchell and Jones 2005) is displayed. This data set depends only on rain gauge measurements.

The model simulates the precipitation over Africa reasonably well. The maxima over the west coast (10^0W, 10^0N), the Cameroon Highlands (10^0E, 5^0N), and Ethiopian Highlands (35^0E, 15^0N) are all in place. The northern edge of the modeled precipitation (e.g., the 2mm/day line) is slightly further north than in the observations, all of which are south of 18^0N. Therefore, the modeled precipitation over the Sahel is greater than the observed averages by roughly 2mm/day. This difference will be revisited when the model's performance in reproducing the observed precipitation variability is considered in the next section.

The African precipitation from the regional model is better than those of most of the atmospheric GCMs from the Atmospheric Model Intercomparison Project (AMIP; Gadgil and Sajani 1998). Few of the AMIP GCMs reproduce the northern edge of summer precipitation near the observed latitude and even fewer reproduce the magnitude and location of the precipitation maxima in the continent. Currently, much GCM mod-

Table 3.1: Table 1 Description of the regional model experiments

Experiment Name	**Prescription of SST annual cycle**
CTL	50-year mean (1950-1999) over the entire domain.
ATL+IND80	1980-1989 mean over the entire domain.
IND80	1980-1989 mean over the Indian Ocean and the 50-year mean elsewhere.
ATL80	1980-1989 mean over the Atlantic Ocean and the 50-year mean elsewhere.
ATL+IND90	1990-1999 mean over the entire domain.
IND90	1990-1999 mean over the Indian Ocean and the 50-year mean elsewhere.
ATL90	1990-1999 mean over the Atlantic Ocean and the 50-year mean elsewhere.

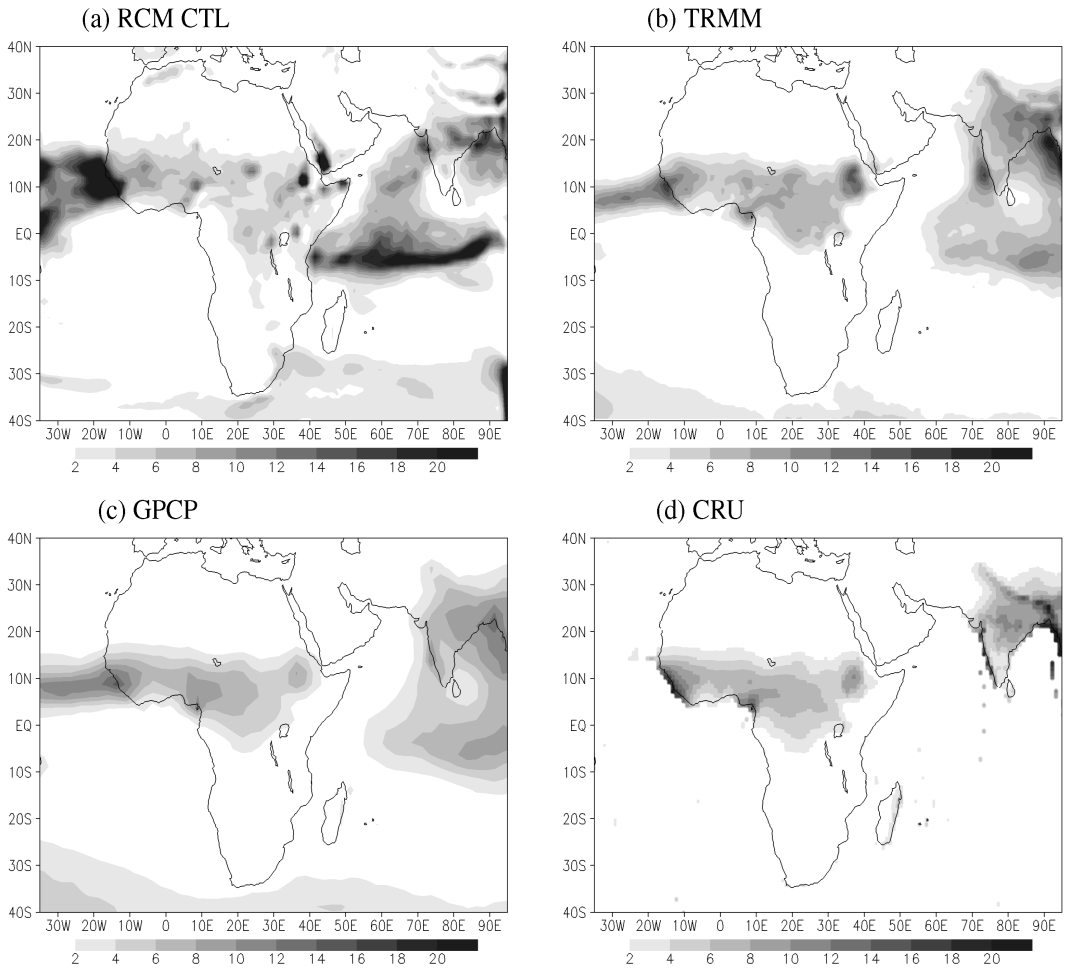

Figure 3.3: JAS mean precipitation (mm/day) from the (a) RCM simulation and observations from (b) TRMM (3B42) (7-year mean), (c) GPCP (27-year mean) and (d) CRU TS 2.1 (50-year mean).

eling effort is focused on coupled ocean/atmosphere models. Many of these models do not capture the strong meridional precipitation gradients that characterize the transition from rain forest to desert across the Sahel (Cook and Vizy 2006).

The model also captures the precipitation maxima over India (75^0E, 15^0N) and western coast of Thailand and Burma (90^0E, 15^0N). The relatively dry condition surrounding southern India and Sri Lanka is also reproduced. However, precipitation over the equatorial Indian Ocean is excessive in the model and extends too far west toward the east coast of Africa.

Figure 3.4 shows the mean summer atmospheric circulation from CTL and the NNRP at the 925 hPa and 700 hPa pressure levels. The model simulates the low-level southwesterly monsoon flow over West Africa, and the flows associated with the North and South Atlantic Highs (Figures 3.4a and 3.4b) realistically. Consistent with the fact that the model produces excessive precipitation over the equatorial Indian Ocean, the model's Somali jet is weaker than that in the NNRP. Similarly, the African Easterly jet is weaker than in the reanalysis, but the westerly flow across the South Atlantic and Indian Oceans is well represented (Figures 3.4c and 3.4d).

Since the model captures the important features of the circulation and precipitation fields over regions relevant to the purpose of the study, it builds confidence in the subsequent analysis.

3.3 Analysis

Figure 3.5a shows the modeled anomalous precipitation when 1980s SSTs are prescribed over both ocean basins, i.e., ATL+IND80 minus CTL. Precipitation rates over

(a) NNRP 925 hPa

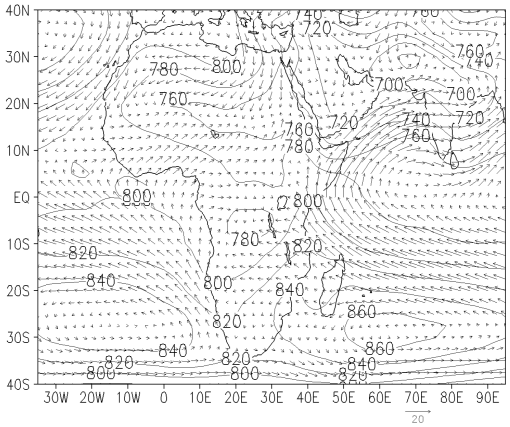

(b) RCM 925 hPa

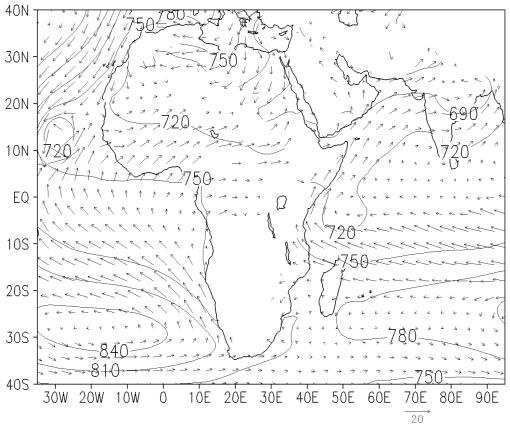

(c) NNRP 700 hPa

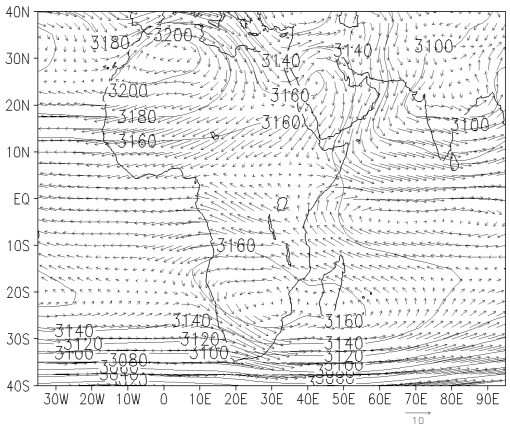

(d) RCM 700 hPa

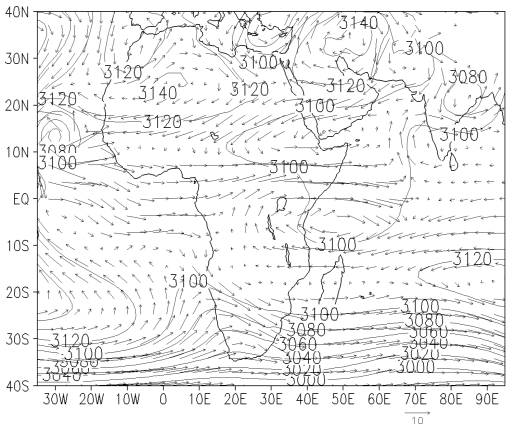

Figure 3.4: Winds (m/s) and geopotential heights (gpm) from the (a) NCEP/NCAR reanalysis at 925 hPa, (b) RCM at 925 hPa, (c) NCEP/NCAR reanalysis at 700 hPa, and (d) RCM at 700 hPa.

the western and central Sahel are reduced by an average of about 1mm/day. Comparison of Figure 3.5a with the precipitation from CTL (Figure 3.3a) shows that the 1980's SSTs introduce about 50% reduction in precipitation over the Sahel similar to the observed percentage reduction (Figure 3.1a). The magnitude of the drying is greatest over the western Sahel where the observed and simulated climatological precipitation rates are also the largest. The drying extends across Africa to the Ethiopian highlands with a minor discontinuity over the central Sahel.

The precipitation difference between ATL+IND90 and CTL (Figure 3.5c) shows that prescribing 1990s decadal mean SSTs introduces somewhat wetter conditions over the central Sahel and Guinean coast, while there are still localized dry regions over western Sahel and Ethiopian highlands (Figure 3.5b). Overall the 1990s anomalies are smaller than those of the 1980s as in the observations.

Figure 3.5c shows the difference between the 1990s and the 1980s in the model, analogous to Figure 3.1c for the observations. In both the model and the observations, the 1990s are significantly wetter over much of the Sahel.

Clearly, the model captures the decadal precipitation variability over the Sahel. The physical processes for the 1980s drought and the partial recovery during the 1990s are analyzed below.

3.3.1 Mechanisms of the 1980s drought

In order to isolate the processes responsible for the 1980s dryness, the results from the experiments with prescribed 1980s SSTs over the individual ocean basins are analyzed. Figures 3.6a and 3.6b show SST and precipitation differences between IND80

(a) ATL+IND80 - CTL

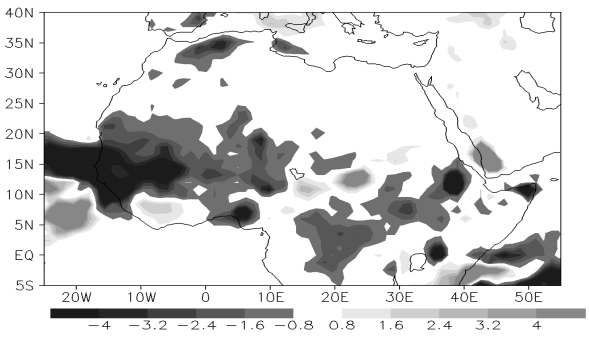

(b) ATL+IND90 - CTL

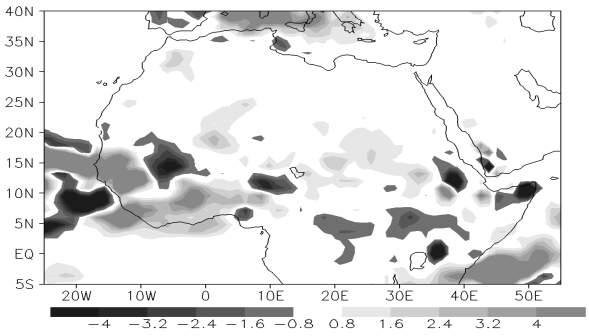

(c) ATL+IND90 - ATL+IND80

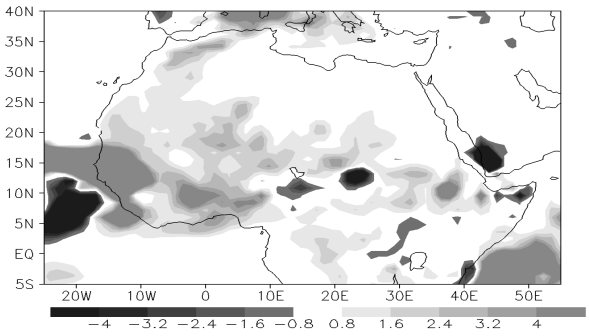

Figure 3.5: JAS precipitation (mm/day) from the RCM simulations. (a) ATL+IND80 minus CTL, (b) ATL+IND90 minus CTL and (c) ATL+IND90 minus ATL+IND80.

and CTL, respectively. The widespread Indian Ocean warming of about 0.4 K imposed in IND80 (Figure 3.6a) introduces drought over the western and central Sahel as well as the Ethiopian highlands, while the Guinean coast is mostly wetter. The magnitude of the response is comparable to that associated with warming over both Atlantic and Indian Ocean basins (compare Figures 3.5a and 3.6b), but the former is not as widespread as the latter. Prescribing the 1980s Atlantic Ocean SSTs (Figures 3.6c and 3.6d) introduces dry conditions along the west coast, but the response in the continental interior is not as pronounced.

The simulations indicate that the 1980s droughts were due to a combined warming of both ocean basins. Even though Indian Ocean warming is primarily responsible for the drying in the continental interior, the concurrent tropical Atlantic Ocean warming significantly enhanced it both in areal coverage and magnitude.

To understand the mechanisms by which regional SSTs influence Sahel precipitation, the JAS mean moisture budget from CTL vertically integrated through the full depth of the model atmosphere (surface to 50 hPa) is diagnosed using

$$\int_{P_s}^{P_t}(\dot{q})dp = \int_{P_s}^{P_t}(\frac{\partial q}{\partial t})dp + \int_{P_s}^{P_t}(\frac{\partial uq}{\partial x} + \frac{\partial vq}{\partial y})dp - \omega q_{P_t} + \omega q_{P_s} + \int_{P_s}^{P_t} F_q dp \qquad (3.1)$$

The left hand side of (3.1) is the net change in mixing ratio due to evaporation and condensation (if negative) and the right hand side includes zonal and meridional moisture convergence, moisture diffusion (F_q, which is largely surface evaporation because nearly all of the turbulence is in the boundary layer), the vertical moisture flux at the bottom and top of the model atmosphere as well as the local time rate of change of mixing ratio.

Figures 3.7a-d show the LHS and the first three terms on the RHS of (1); the last two terms on the RHS are negligible. The main source of moisture for condensation over the Sahel is horizontal moisture convergence (compare Figures 3.7a and 3.7b). The

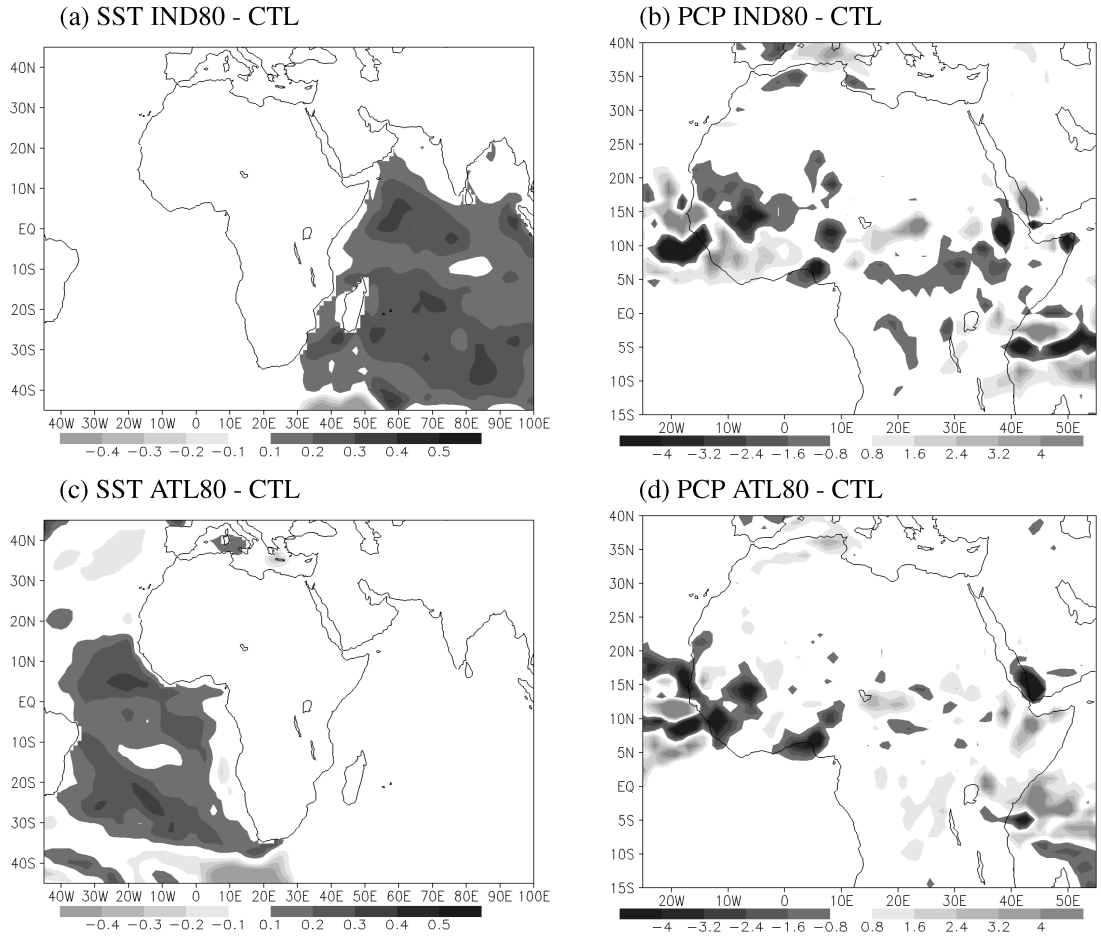

Figure 3.6: RCM precipitation response to 1980s Indian and Atlantic Ocean SST variations. a) SST (K) IND80 minus CTL, (b) precipitation (mm/day) IND80 minus CTL, (c) SST ATL80 minus CTL and (d) precipitation ATL80 minus CTL.

contribution of diffusion (Figure 3.7c), i.e., direct evaporation from the surface, is small and does not reflect the structure of the condensation field. This shows that much of the moisture over the Sahel is transported from the adjacent oceans.

Over the oceans, on the other hand, evaporation is widespread. The near surface vertical transport of moisture (Figure 3.7d), i.e., resolved vertical mixing, is negative

and so reduces condensation. Therefore, oceanic evaporation is the main source of moisture in the domain, while condensation and vertical mixing over both the oceans as well as over land are the sinks. Hence, in order to understand the influence of SSTs on Sahel precipitation, the nature of the moisture transport into the region needs to be analyzed.

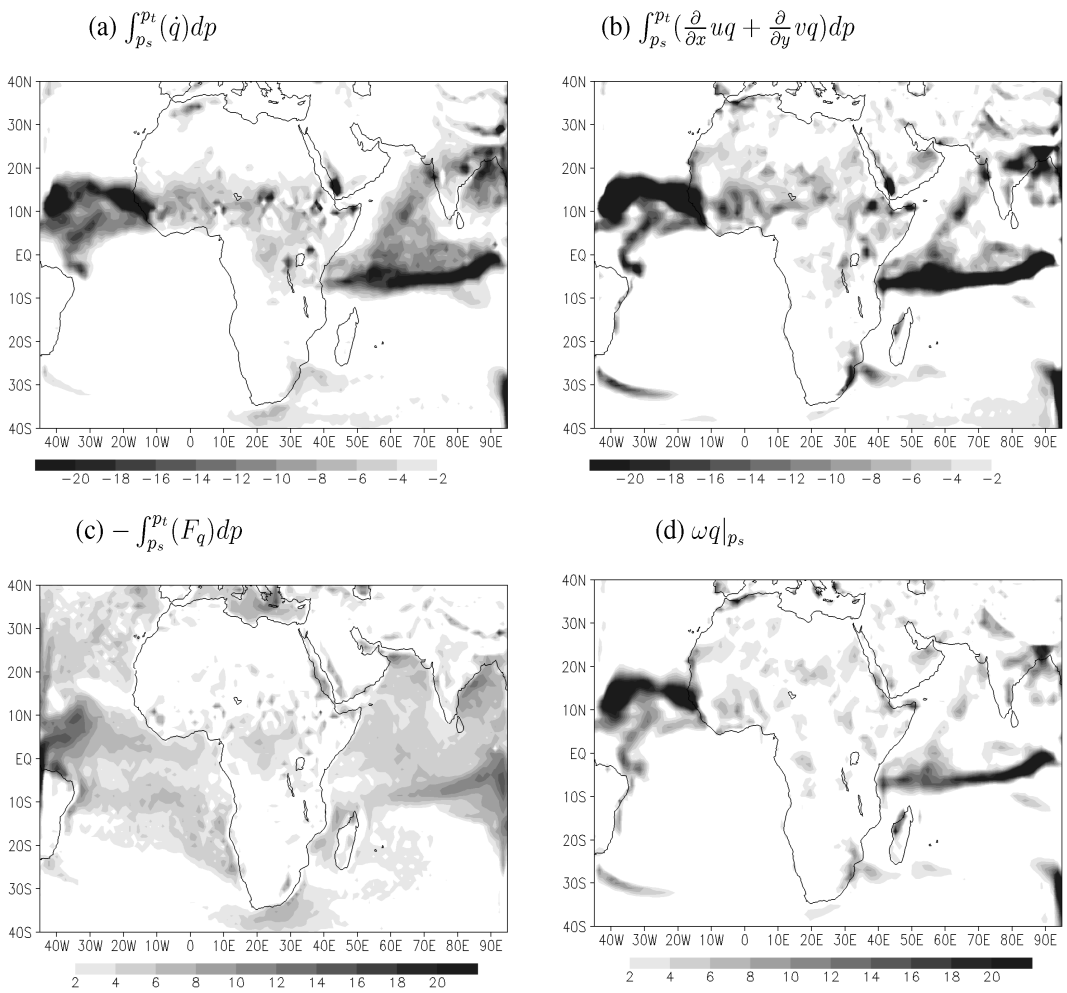

Figure 3.7: The terms in the vertically integrated moisture budget (1). (a) condensation, (b) horizontal convergence, (c) diffusion (surface evaporation) and (d) vertical advection at the surface. All are in mm/day.

Consider the moisture transport vector field $qV = (qu, qv)$. The vertically integrated

convergence of this vector field ($\nabla \cdot qV$) was shown in Figure 3.7b. This vector field can be decomposed into its irrotational and nondivergent components. By definition, the non-divergent component has no direct effect on the local moisture budget and precipitation. Separating the two components of the moisture transport vector enables identification of the sources and sinks of moisture. This is done by first defining a "moisture flux potential", χ, (the moist counterpart to the velocity potential) such that the irrotational component of the moisture transport (hereafter moisture flux) is $(qV)_{irr} = \left(\frac{\partial \chi}{\partial x}, \frac{\partial \chi}{\partial y}\right)$. Taking its divergence, we obtain

$$\nabla^2 \chi = \nabla \cdot (qV) \quad . \tag{3.2}$$

Poisson's equation (3.2) is solved using the Gauss-Seidel iteration (Jaluria and Torrance 2003) over the domain. Similarly, the relative vorticity is calculated from the wind field and used to calculate the streamfunction to identify the non-divergent Rossby wave components of the anomalous circulations.

Figure 3.8a shows the JAS mean vertically-integrated χ and moisture flux vectors from CTL. The main source of moisture in the domain is the tropical southern Atlantic Ocean (centered near 10^0S and 25^0W), while the Indian Ocean and the African Sahel are sinks. The strongest mean moisture flow into the continent occurs across the Coast of Guinea between 10^0E and 15^0W. Figure 3.8b shows the vertical structure of the meridional moisture flux at 5^0N. Figures 3.8a and 3.8b together demonstrate that the low-level southerly moisture flux across the Guinean coast is the main supply of moisture for the African Sahel, as expected.

To understand how Indian Ocean warming influences Sahel precipitation, the anomalous moisture flux field is considered (Figure 3.9a). Along the west coast of the Sahel, the anomalous moisture flux is zonal and directed away from the continent. Comparison with that of CTL (Figure 3.9b) shows a moisture loss of up to 50% from the Sahel region.

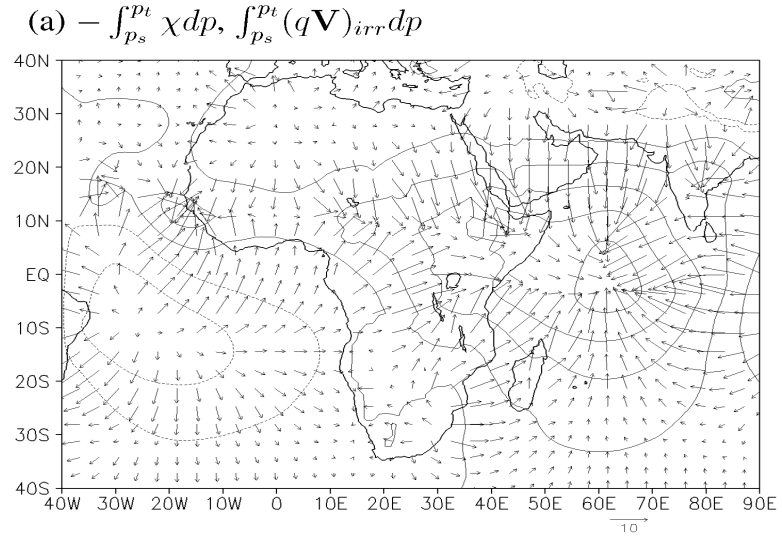

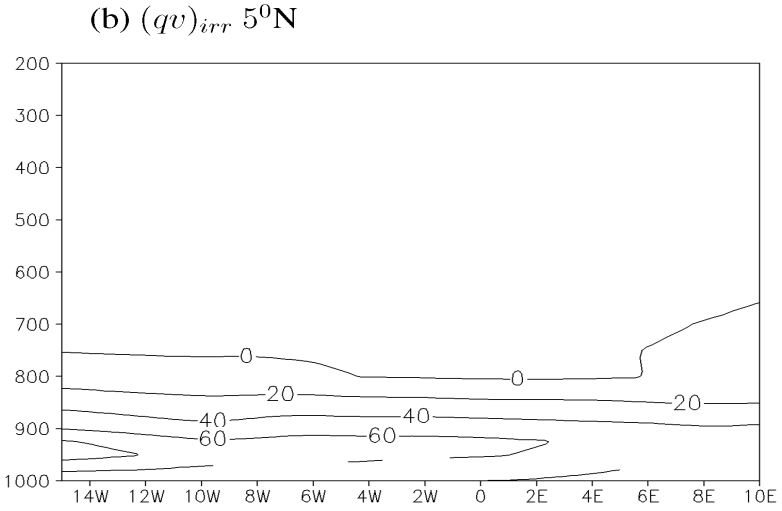

Figure 3.8: (a) Moisture flux potential and moisture flux (gm/kgs) from CTL and (b) cross section of meridional moisture flux at 5^0N (gm/kgs).

Figure 3.9b shows a latitude-height cross-section of the anomalous zonal moisture flux at 15^0W. The moisture flow away from the continent occurs above the boundary layer and is strongest near 700 hPa. Near the surface, there is a shallow anomalous moisture transport into the continent. This strengthening of the westerly flow onto the continent is consistent with the fact that the reduced precipitation and cloud cover warms up the land surface (not shown).

Figure 3.9c shows the anomalous circulation at 700 hPa over northwestern Africa. This circulation is a Rossby response to the wind divergence to its immediate east (Figure 3.9d), which is a strengthening of the Saharan high. The associated anticyclonic circulation enhances the African easterly jet and the anomalous easterly moisture flux. This divergence, in turn, along with the pair of cyclonic circulations over northeastern and southeastern Africa, constitutes the Rossby response to the large-scale convergence forcing over the equatorial Indian Ocean.

In their regional modeling study, Paeth and Hanse (2004) evaluate the validity of a linear analysis of the tropical African climate response to a prescribed forcing. They find that, to a large extent, the atmospheric circulation associated with SST anomalies can be represented by the first 10 Gill-Matsuno modes. However, they also find that the processes that give rise to the atmospheric heating field are nonlinear. Therefore, the primary non linear processes that determine the atmospheric response to SSTs and the role of the background climatology deserve some attention.

The perturbation moisture convergence,$\nabla \cdot ((qV)')$, which is shown to be the primary contributor to the precipitation anomalies, is decomposed to distinguish the roles of the background flow and the perturbations. Let $q = \bar{q} + q'$, where q is the decadal mean value (1980s or 1990s), the overbar refers to CTL, and the prime indicates the difference.

(a) $(q\mathbf{V})_{irr}$ IND80 - CTL

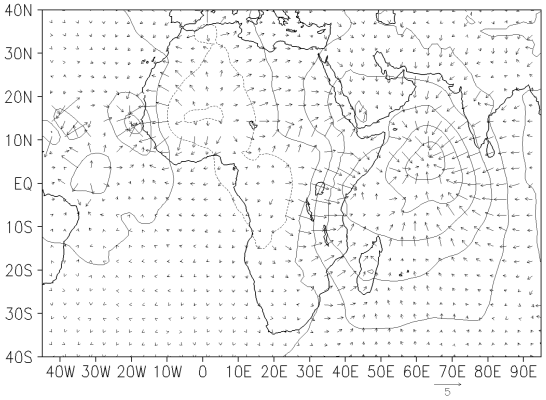

(b) $(qu)_{irr}$ IND80 - CTL 15^0W

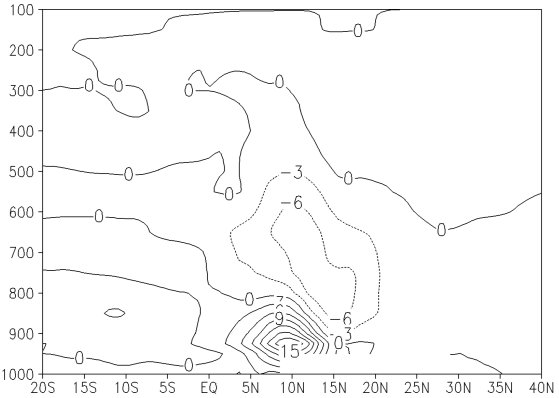

(c) $\mathbf{V}_{nd}$ IND80 - CTL

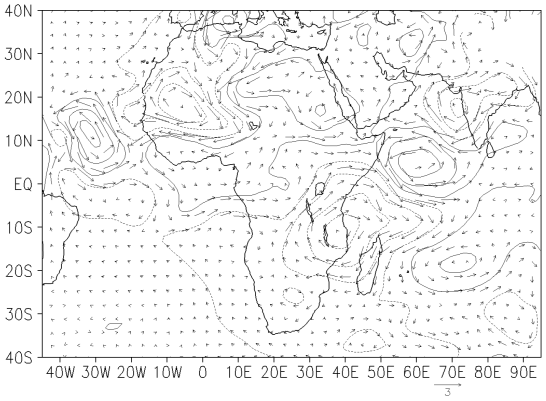

(d) $\mathbf{V}_{irr}$ IND80 - CTL and q

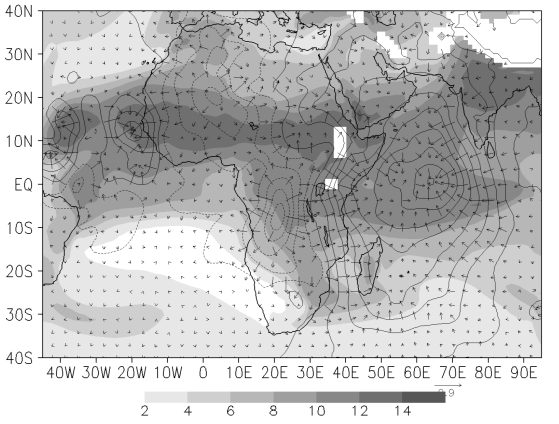

Figure 3.9: IND80 minus CTL, JAS mean (a) vertically integrated irrotational moisture flux (gm/kgs), (b) zonal moisture flux at 15^0W (gm/kgs) (c) non divergent wind at 700hpa (m/s) and (d) irrotational wind (m/s) and mixing ratio (g/kg) at 700hPa.

Similarly, $V = \bar{V} + V'$. Then,

$$\nabla \cdot (qV)' = \nabla \cdot \left(\bar{q}V' + q'\bar{V} + q'V' \right) \quad . \tag{3.3}$$

The terms on right hand side of (3.3) are the total change in moisture convergence due to the interaction of the anomalous wind divergence with the background moisture, the interaction of moisture perturbations with the background flow, and the interaction of anomalous mixing ratio with the anomalous wind field, respectively. The response to the anomalous SSTs is dominated by the first term. This is evident in Figure 3.9d, in which the locations of maximum convergence forcing over both the Atlantic and Indian Oceans also correspond to regions of large mixing ratio. In a similar manner, the divergence over Africa introduced by Indian Ocean warming has its greatest impact over the Sahel, where the background mixing ratio is at its maximum during summer. The anomalous anticyclonic circulation associated with this divergence, which drives moisture away from the continent (Figure 3.9b), further amplifies the effect.

The response of the modeled Sahel precipitation to the 1980s Atlantic Ocean warming (Figures 3.6c and 3.6d) is also analyzed. Atlantic Ocean warming also introduces strong moisture convergence off the western coast of the continent (Figure 3.10a) and poses direct competition for the available moisture. The anomalous anti-cyclonic circulation, which was shown to drive moisture away from the continent in the case of Indian Ocean warming, also exists in this case. However, here it extends to the surface (Figure 3.10b). Once again, the strong forcing over the northern equatorial Atlantic, despite the fact that much of the SST warming is south of the equator, can be explained by the fact that the former is the region where the background mixing ratio (and the first term on the RHS of (3)) is maximum (Figure 3.10d).

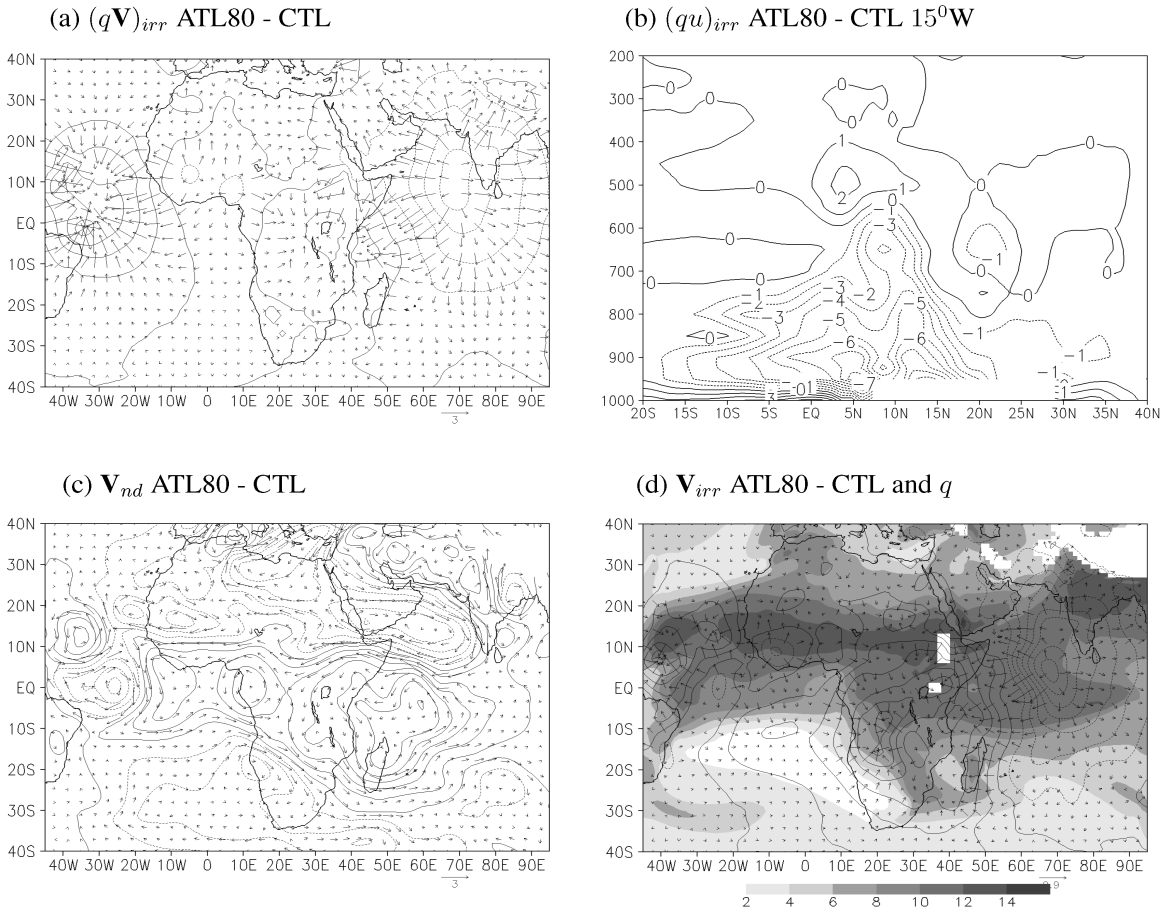

Figure 3.10: ATL80 minus CTL, JAS mean (a) vertically integrated irrotational moisture flux (gm/kgs), (b) zonal moisture flux at 15^0E (gm/kgs), (c) nondivergent wind at 700hpa (m/s) and (d) irrotational wind (m/s) and mixing ratio (g/kg) at 700hPa.

3.3.2 The 1990s recovery

To understand the modeled and observed partial recovery of Sahel precipitation in the 1990s (Figures 3.1c and 3.5c), the results from the experiments in which 1990s SSTs are imposed over the two oceans individually are considered (see Table 1). Figure 3.11 shows the prescribed summer mean SST differences between IND90 and CTL, as well as

between ATL90 and CTL and the respective precipitation differences. In the 1990s the northern tropical Atlantic Ocean was warmer than during the 1980s (compare Figures 3.11c and 3.6c), but the rest of the tropical Atlantic Ocean is cooler. But the Atlantic in both decades is generally warmer than the climatology. Similarly, a comparison of Figures 3.11a and 3.6a demonstrates that the tropical Indian Ocean was anomalously warm during both the 1980s and 1990s, but that the warming is stronger and zonally broader during the 1990s than the 1980s.

The SST anomalies over both ocean basins individually introduce widespread precipitation recovery (Figures 3.11b and 3.11d), but the positive precipitation anomalies associated with ATL90 SSTs are more widespread. Therefore, the recovery of the 1990s is primarily due to Atlantic Ocean SST patterns of that decade.

Figure 3.12a shows differences in the moisture flux potential (3.2) and the moisture flux vectors for ATL90 minus CTL, and Figure 3.12b displays the irrotational wind and the mixing ratio differences. The warm SST anomalies off the west coast of Africa (Figure 3.11c) are seen to be coincident with moist conditions and this introduces localized moisture convergence along the coast. The associated cyclonic wind pattern favors moisture transport into the continent that is greatest at 700 hPa (Figures 3.12c and 3.12d).

While the circulation patterns associated with 1990s and 1980s Atlantic Ocean warming are similar in that they both have a pair of cyclonic circulations which are typical response to local convergence, they differ in their strength and areal coverage (Figures 3.10c and 3.12c). The westerly part of the cyclonic circulation pattern of the 1990s favors moisture flow into the continent, while that 1980s is fully over the ocean. This suggests that the scale of the forcing is important factor in determining the direction of moisture transport between the ocean and continent, while this response is amplified by

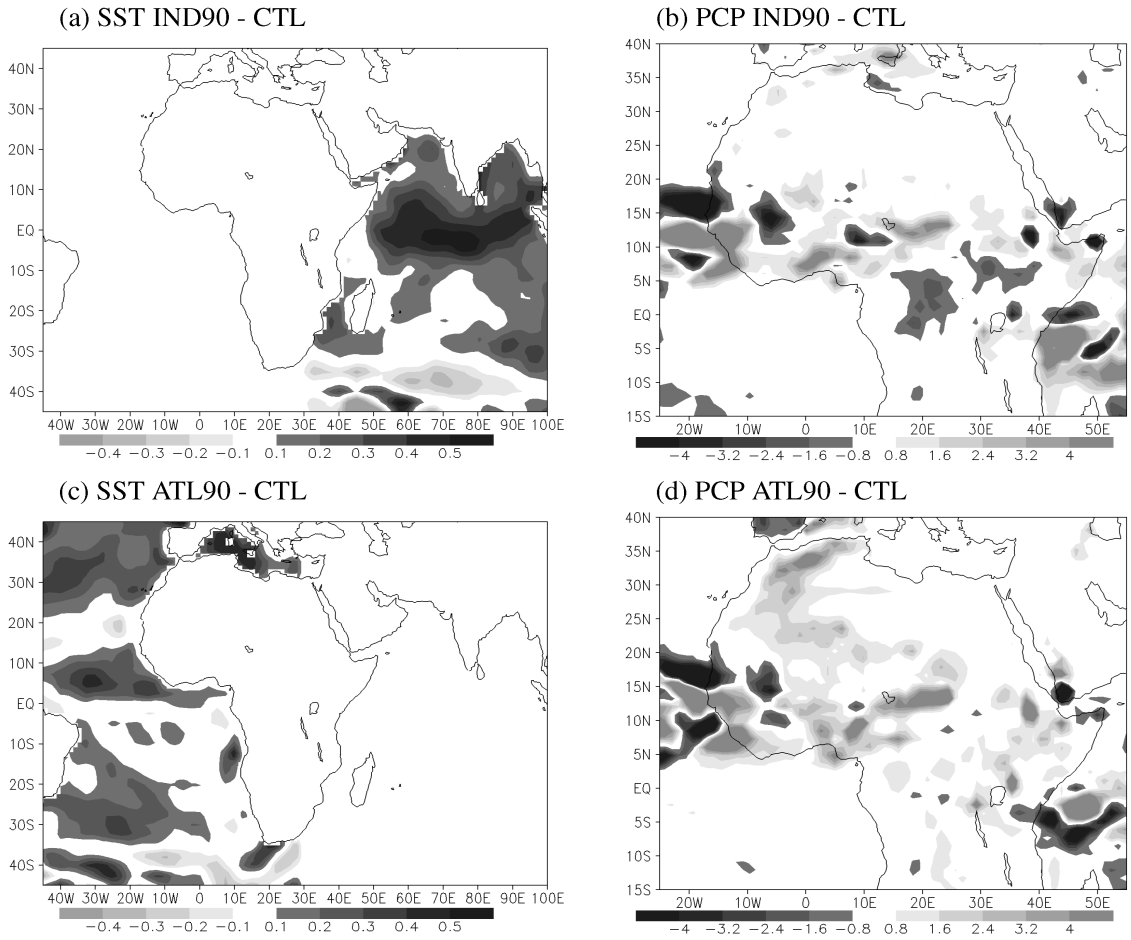

Figure 3.11: ATL90 minus CTL JAS mean (a) vertically integrated moisture flux (gm/kgs), (b) irrotational wind (m/s) and mixing ratio (g/kg) at 700 hPa. (c) non-divergent wind at 700 hpa, ATL90 minus CTL and (d) zonal moisture flux at 15^0E (gm/kgs).

(a) $(q\mathbf{V})_{irr}$ ATL90 - CTL

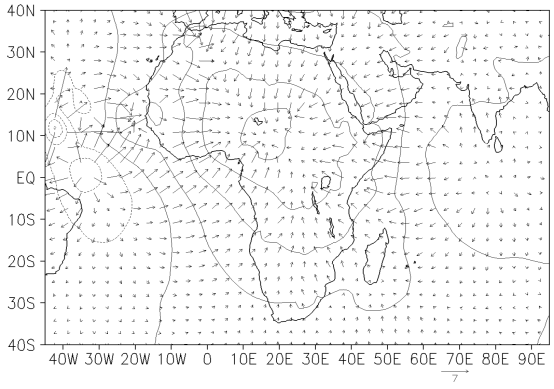

(b) $\mathbf{V}_{irr}$ ATL90 - CTL and q

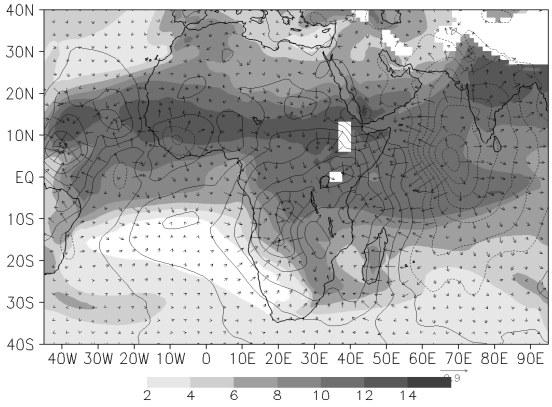

(c) $\mathbf{V}_{nd}$ ATL90 - CTL

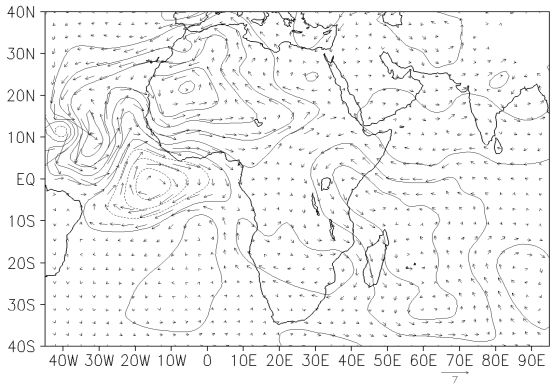

(d) $(qu)_{irr}$ ATL90 - CTL 15^0W

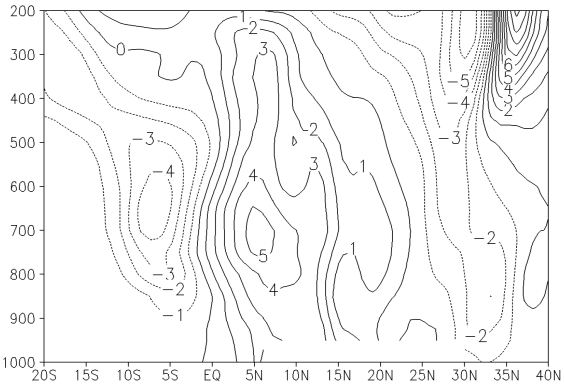

Figure 3.12: ATL90 minus CTL JAS mean (a) vertically integrated moisture flux (gm/kgs), (b) irrotational wind (m/s) and mixing ratio (g/kg) at 700 hPa. (c) non-divergent wind at 700 hpa, ATL90 minus CTL and (d) zonal moisture flux at 15^0E (gm/kgs).

the circulations associated with the condensation (and convergence) anomalies over the continent.

Figures 3.13a and 3.13b show the circulation in response to the 1990's warming in the Indian Ocean. Subsidence is induced over the equatorial Atlantic, with anomalous irrotational westerly flow onto the continent. The nondivergent flow onto the continent is also westerly, associated with the expected pair of cyclones that straddle the equator (Figure 3.13b).

The reason for the strikingly different response in the 1990s compared with the 1980s, even though the forcing over the Indian Ocean is quite similar, becomes apparent when the horizontal scales of the forcing above the boundary layer, i.e., the moisture convergence, are compared. While many of the circulation features of the 1980s and 1990s are similar, the 1990s convergence over the Indian Ocean covers a wider area and the subsequent divergence occurs over the equatorial Atlantic Ocean. In contrast, the moisture divergence associated with Indian Ocean warming in the 1980s occurs over western and central Africa (compare Figures 3.13a and 3.9a). Consequently, while the anomalous moisture flow across the west coast of Africa (15^0W) is directed away from the continent in the 1980s, it is directed onto the continent in the 1990s.

The difference in the scales of the forcing is also apparent in the non-divergent wind fields at 700 hPa (and Figures 3.13b and 3.9c). While the anomalous cyclonic circulations over northeastern and southeastern Africa are similar in both simulations, that of the 1990s extends far into western Africa and favors westerly moisture flow from the eastern equatorial Atlantic.

(a) $(q\mathbf{V})_{irr}$ IND90 - CTL

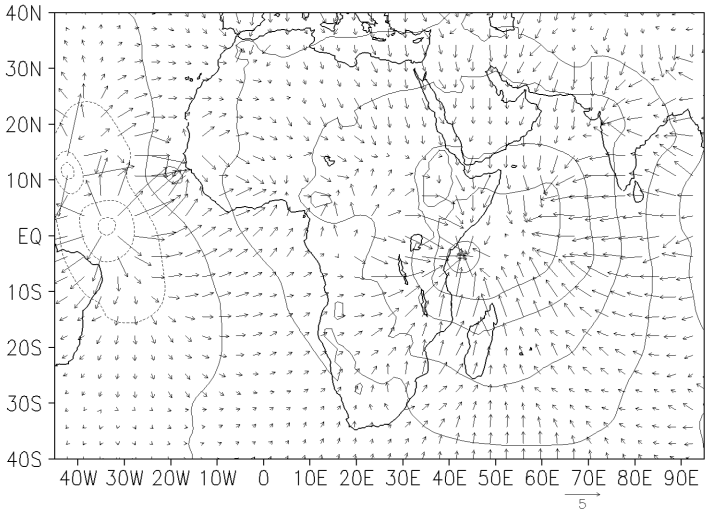

(b) $\mathbf{V}_{nd}$ IND90 - CTL

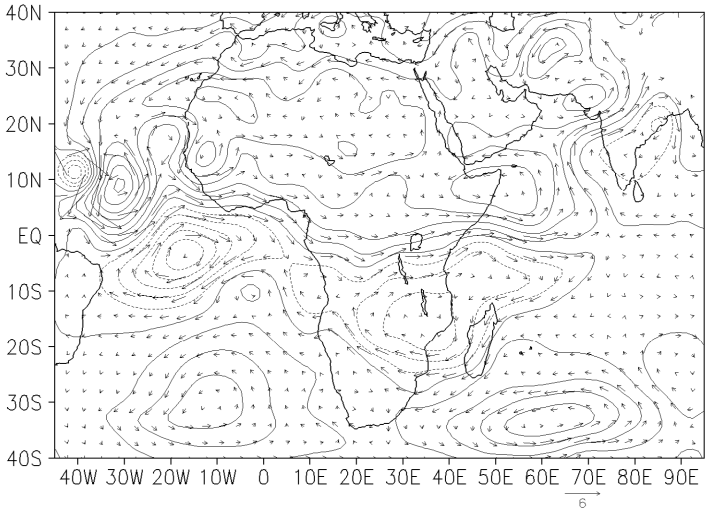

Figure 3.13: (a) IND90 minus CTL, JAS mean vertically integrated moisture flux (gm/kgs) and (b) non-divergent wind (m/s) at 700 hpa IND90 minus CTL.

3.3.3 Comparison with observations

To further validate the conclusions drawn from the model simulations, decadal variability in the NNRP wind and geopotential height fields are considered. We examine the full wind fields and the geopotential heights from the reanalysis because these are assimilated variables and, therefore, close to observations. The relatively low resolution of the reanalysis (2.5^0 x 2.5^0) and the fact that moisture fields are not assimilated makes it inadvisable to decompose the moisture convergence field as in the analysis of the model output. However, we can confidently examine the full fields for evidence of the processes identified in the model analysis.

Figure 3.14a shows the climatological mean 700 hPa wind and geopotential heights from the reanalysis and Figure 3.14b shows the difference between the 1980s mean and the climatology. The high geopotential heights and the associated anticyclonic circulation anomaly over the central Sahel (Figure 3.14b) is the main feature of the decade, representing a southward extension of the Saharan high and the African easterly jet. This agrees with the regional model simulations of the 1980s, which resulted from both Indian and Atlantic Ocean SSTAs (Figures 3.9c and 3.10c). In agreement with our modeling results the NNRP data also suggests the droughts of 1980s are related to the anticyclonic circulation and strengthened easterly flow. Compared with the reanalysis, the model shifts the anticyclonic circulation anomaly to the west, and the precipitation anomaly is also farther west than in the observations (compare Figures 3.1a and 3.5a).

A similar geopotential high and anticyclonic circulation anomaly is also observed in the 1990s in the reanalysis (Figure 3.14c). The associated easterly flow over western Africa, however, is weaker, implying that the moisture loss from the continent is also weaker. Differences between 1990s and 1980s in the reanalysis highlight the distinction (Figure 3.14d). Thus, consistent with our modeling results, the reanalysis suggests

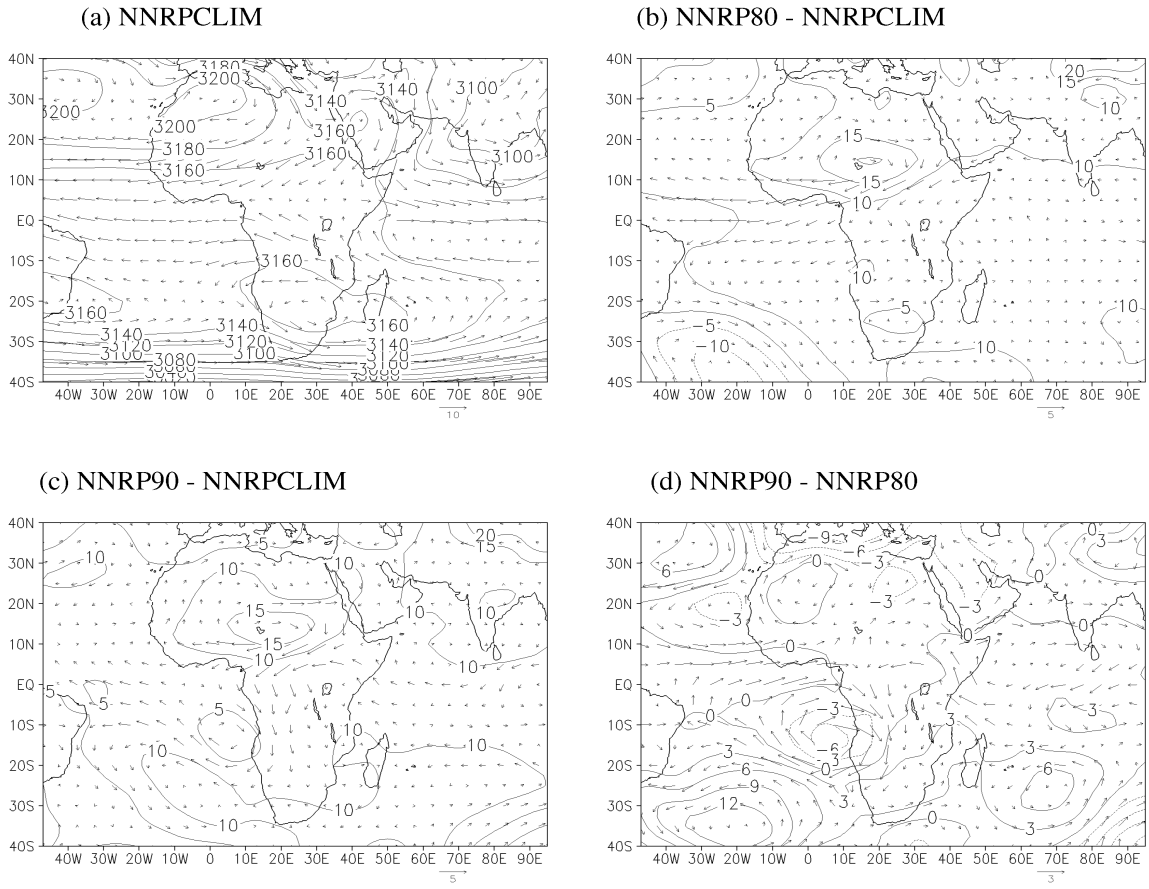

Figure 3.14: JAS mean wind (m/s) and geopotential height (gpm) at 700 hPa from the NCEP/NCAR reanalysis (NNRP); (a) climatological (1950-2002) average, (b) 1980s minus climatological, (c) 1990s minus climatological and (d) 1990s minus 1980s.

that the precipitation recovery of the 1990's over the Sahel is related to the anomalous cyclonic circulation (relative to the 1980s) associated with an anomalous low off the northwestern coast of Africa.

3.4 Discussion

This study shows that combined Indian and Atlantic Ocean SST anomalies are responsible for the 1980s droughts over the Sahel. Warming over the Indian Ocean during the 1980s introduced local convergence that forced subsidence over central Africa and an anomalous anticyclonic circulation over the west coast as part of the Rossby wave response to that convergence. This anticyclonic circulation enhances the westward transport of moisture from the Sahel to the tropical eastern Atlantic, desiccating the Sahel (Figures 3.9 and 3.14). The Atlantic Ocean warm anomaly of the 1980s introduced anomalous moisture convergence over the northern tropical Atlantic, further depleting the moisture supply into the continental interior (Figure 3.10).

Important nonlinear processes are identified. The location and extent of the forcing (i.e., anomalous moisture convergence in the vicinity of the SST anomalies) not only depend on the SST anomalies but also on the distribution of background atmospheric moisture. For example, while the strongest SST anomalies in the 1980s Atlantic Ocean are south of the equator (Figure 3.6c), the strongest anomalous moisture convergence over the ocean is near 10^0N, close to the latitude of maximum background mixing ratio (Figures 3.10a and 3.10d). This is also true for the remote response. The Sahel's response to the forcing over both ocean basins is strongest because the climatological moisture content there is at its maximum during northern summer. In other words, the larger the background moisture content, the larger will be the changes in moisture convergence for the same anomalous winds convergence (3.3).

The modeled 1990s recovery is related to changes in the scale and distribution of the forcing. The warm ocean surface off the northwestern coast of Africa during 1990s is mainly responsible for the recovery of the model precipitation (Figures 3.11c and

3.11d). The relatively strong cyclonic circulation over the northern tropical Atlantic favors anomalous moisture transport into the continent. Comparison of the moisture convergence responses to the 1980s and 1990s Indian Ocean SST anomalies shows that the response to the latter has a larger scale so the associated low-level divergence is located over the tropical Atlantic (compare Figures 3.9 and 3.13). Therefore, instead of an anomalous anticyclonic circulation driving away moisture from the continent as was the case for 1980s SST forcing, the flow is cyclonic and favors moisture transport into the continent for 1990s SST forcing.

It is important to note that while the primary forcing is external to the Sahel region, the local responses are amplified by moist processes. For example, the divergence over the Sahel in 1980s is enhanced by the anomalous moisture transport that desiccates the region just as much as the latter is a (Rossby wave) "response" to the former. The same applies to the convergence and the associated anomalous cyclonic circulations which supply the moisture during the 1990s recovery.

Some of these results agree with previous studies by various authors. Giannini et al. (2003), Bader and Latif (2003), and Lu and Delworth (2005) also show in their numerical studies that the subsidence and drought over the Sahel region are Rossby wave responses to Indian Ocean warming. In addition to that, however, our model results show that the associated anticyclonic circulation to the immediate west of the subsidence plays an important role in driving moisture away from the Sahel region.

While our results also agree with those of Hoerling et al. (2006) in their conclusion that Atlantic Ocean SSTs play an important role in Sahel decadal variability, the physical mechanisms inferred from the model results differ somewhat. In particular, Hoerling et al. (2006) suggest that a modulation of the latitudinal location of the ITCZ by meridional SST gradients in the Atlantic is the main cause of Sahel decadal precip-

itation variability. Our results, however, suggest that the influence of SST anomalies is most prominent over regions of maximum mixing ratio. Therefore, the anomalous convergence over the Atlantic Ocean is at nearly the same latitude as the Sahel region rendering the competition for moisture between the Sahel and the Atlantic a predominantly zonal process (Figure 3.10a). The role of northern Atlantic SST warming in the partial recovery of precipitation is, however, apparent in our model as well.

The importance of background moisture distributions and the scale of the forcing, as demonstrated by the vastly different response of Sahel precipitation to 1980s and 1990s SSTs, have some implications for analysis and projections of 21^{st} century Sahel precipitation. This study suggests that the Sahel precipitation response to SST variations in this century may be very sensitive to changes in the distribution of both atmospheric moisture and SST.

BIBLIOGRAPHY

[1] Adler, Robert F., George J. Huffman, David T. Bolvin, Scott Curtis, Eric J. Nelkin, 2000: Tropical Rainfall Distributions Determined Using TRMM Combined with Other Satellite and Rain Gauge Information. *Journal of Applied Meteorology*: Vol. 39, No. 12, pp. 2024–2037.

[2] Bader. J., and M. Latif, 2003: The impact of decadal-scale Indian Ocean sea surface temperature anomalies on Sahelian rainfall and the North Atlantic Oscillation, *Geophys. Res. Lett.*, 30(22), 2169, doi: 10.1029/ 2003GL018426.

[3] Brooks, N., 2004: Drought in the African Sahel: long term perspectives and future prospects, Tyndall Centre Working Paper No. 61.

[4] Charney, J.G., 1975: Dynamics of deserts and drought in the Sahel. Quarterly Journal of the Royal Meteorological Society, **101**, 193-202.

[5] Cook K.-H. and E.K. Vizy, 2006: Coupled Model Simulations of the West African Monsoon System: 20th century Simulations and 21st Century Predictions. *J. Climate*, **19**, 3681-3703

[6] Gadgil S., and S. Sajani, 1998: Monsoon precipitation in the AMIP runs. *Climate Dyn.*, **14**, 659–689.

[7] Giannini, A., Saravanan, R. and Chang, P., 2003: Oceanic forcing of Sahel rainfall on interannual to interdecadal time scales. *Science* **302**: 1027-1030.

[8] Hoerling, M., J. Hurrell, J. Eischeid, and A. Phillips 2006: Detection and attribution of 20th century northern and southern African rainfall change, *J. Clim.*, 19, 16 3989–4008.

[9] Huffman, G. J, and Coauthors, 1997: The Global Precipitation Climatology Project (GPCP) combined precipitation dataset. *Bull. Amer. Meteor. Soc.,* **78,** 5–20.

[10] Jaluria, Y and K. Torrance 2003: Computation heat transfer *Taylor and Francis Group* 544pp.

[11] Joseph, J.H., W.J. Wiscombe, and J.A. Weinman, 1976: The delta-Eddington approximation for radiative flux transfer. *J. Atmos. Sci.,* **33**, 2452-2459.

[12] Kain, John S. and J. M. Fritsch. 1990: A One-Dimensional Entraining-Detraining Plume Model and its Application in Convective Parameterization. *J. Atmos. Sci.,* **47**, 23, pp 2784 - 2802.

[13] Kalnay, E. M, and others, 1996: The NCEP/NCAR 40-year reanalysis project. *Bull. Amer. Meteor. Soc.* **77** 437- 471.

[14] Kiehl, J.T., and B.P. Briegleb, 1991: A new parameterization of the absorptance due to the 15-micron band system of carbon dioxide. *J. Geophys. Res*., **96**, 9013-9019.

[15] Liebmann, B., and C. A. Smith, 1996: Description of a complete (interpolated) outgoing longwave radiation dataset. *Bull. Amer. Meteor. Soc*., **77**, 1275-1277.

[16] Lu, J. and T. L. Delworth, 2005**:** Oceanic Forcing of the Late 20th Century Sahel Drought. *Geophys.l Res. Lett.,* 32, L22706, doi:10.1029/2005GL023316.

[17] Mitchell et al., 2002: Recent GCIP-sponsored advancements in coupled land-surface modeling and data assimilation in the NCEP Eta Mesoscale Model, *Reprints, 15th Conf. On Hydrology*, AMS, Long Beach, CA, 180-183.

[18] Mitchell, T., and P. Jones, 2005: An improved method of constructing a database of monthly climate observations and associated high-resolution grids. *Int. J. Climatology.,* 25, 693-712.

[19] Nicholson, S. E., 2003: Validation of TRMM and other rainfall estimates with a high density gauge data datasets for West Africa. Part II: validation of TRMM products. *J. Appl. Meteor., **42**, 1355-1368.*

[20] Paeth, H. and A. Hense, 2006: On the linear response of tropical African climate to SST changes deduced from regional climate model simulations Theor. appl. climatol, vol. 83, no1-4, pp. 1-19.

[21] Reynolds, and T. M. Smith, 1995: A high-resolution global sea surface temperature climatology. *J. Climate,* **8,** 1571–1583.

[22] Taylor CM, Lambin EF, Stephenne N, Harding RJ, Essery RLH 2002: The Influence of Land Use Change on Climate in the Sahel. Journal of Climate: Vol. 15, No. 24 pp. 3615–3629.

[23] Troen, I. and L. Mahrt, 1986: A simple model of the atmospheric boundary layer: sensitivity to surface evaporation. *Bound.-Layer Meteorol.*, **37**, 129-148.

[24] Vizy, E. K., and K. H. Cook, 2001: Development and application of a mesoscale climate model for the tropics: Influence of sea surface temperature anomalies on the West African monsoon, *J. Geophys. Res.- Atmos.*, **107** (D3), 10.1029/2001JD000686, 2002.

[25] Ward, M.N., 1998: Diagnosis and short-lead time prediction of summer rainfall in tropical north Africa at interannual and multidecadal timescales. *J. Climate*, 11, 3167-3191.

[26] Zeng N, Neelin JD, Lau KM, Tucker CJ (1999) Enhancement of interdecadal climate variability in the Sahel by vegetation interaction. *Science* 286: 1537-1540

Chapter 4

Development of a Coupled Regional Model and its Application to the Study of Interactions between the West African Monsoon and the Eastern Tropical Atlantic Ocean

Abstract

A regional ocean-atmosphere coupled model is developed for climate variability and change studies. The model allows dynamic and thermodynamic interactions between the atmospheric boundary layer and an ocean mixed layer with spatially and seasonally varying depth prescribed from observations. The model reproduces the West African monsoon circulation as well as aspects of observed seasonal SST variations in the tropical Atlantic. The model is used to identify various mechanisms which couple the West African monsoon circulation with eastern Atlantic SSTs. By reducing wind speeds and suppressing evaporation, the northward migration of the ITCZ off the west coast of Africa contributes to the modeled spring SST increases. This weakens the circulation associated with the North Atlantic subtropical high, leading to a westward expansion of the westerly flow on to the continent and enhances moisture transport onto the continent to support the monsoon. Near the end of the summer, coastal upwelling associated with this enhanced westerly flow as well as the solar cycle lead to the seasonal cooling of the SSTs. Over the Gulf of Guinea, the acceleration of the southerly West African monsoon surface winds contribute to cooling of the Gulf of Guinea between April and July by increasing the entrainment of cool underlying water and enhancing evaporation.

4.1 Introduction

The purpose of this paper is two-fold. The first is to describe the development of a coupled regional ocean/atmosphere/land model. The impetus for the development of this model is to advance our understanding of how monsoon circulations, which develop as a result of land/sea contrast, modify and are influenced by SSTs. The interaction comes about primarily through the local surface heat balance and the application of wind stresses on the ocean surface, which advects water horizontally within the ocean mixed layer and generate upwelling and downwelling. Thus, a basic understanding of this land/atmosphere/ocean interaction does not require a simulation of the global-scale ocean circulation, but would benefit from a higher-resolution simulation that better represents coastlines, topography, upwelling regions, and surface winds, and provides a representation of the monsoon that is better than what is typically generated in coupled GCMs.

The second purpose is to apply the coupled regional ocean/atmosphere/land model to improve our understanding of the West African monsoon system, including its role in determining the pronounced observed seasonality of SSTs in the eastern tropical Atlantic. The West African monsoon system is chosen for this study because this system features strong atmosphere/land surface coupling, and also because this monsoon circulation is thought to play an important role in determining the seasonality of eastern tropical Atlantic SSTs. Also, previous experience in modeling this monsoon system in a regional atmospheric model (Vizy and Cook 2002, Hsieh and Cook 2005, Hagos and Cook 2007) demonstrates that the regional model is able to capture the monsoon system more realistically than the current generation of coupled GCMs (Cook and Vizy 2006).

The following section provides background on the evidence for coupling among the

land, ocean, and atmosphere within the West African monsoon system, and identifies outstanding problems. This review includes a discussion of our current understanding of SST seasonality in the eastern Atlantic, and the extent to which this seasonality is captured in modeling studies. Section 3 describes the coupled atmosphere/ocean/land regional model and, in section 4, the application of the model over West Africa and the adjacent Atlantic Ocean is presented.

4.1.1 The West African monsoon system

The West African summer monsoon is a dominant component of the regional hydrological cycle on which the livelihood of a growing population is dependent. The system comprises surface flow across the Guinean and western coasts on to the continent. Figure 4.1 shows the mean summer (JAS) surface winds from the NCEP/NCAR reanalysis project (hereafter NNRP, Kalnay et al. 1996) and precipitation from TRMM-3B42V6 (Huffman et al. 2001). During the summer, the confluence of the southwesterly monsoon and the northeasterly Harmattan winds is as far as 20^0N and the precipitation maximum is at about 10^0N in the continental interior, with local maxima over Sierra Leon (8^0N) and the Cameroon highlands. During this period, the Atlantic marine ITCZ along with the confluence of the southeasterly and northeasterly surface winds is at its northernmost latitude and the easterly surface winds over the central Atlantic are weak.

The West African monsoon surface winds are primarily driven by temperature contrast between the land and the adjacent ocean surfaces. However, the associated surface heat and momentum fluxes, moisture transport and precipitation introduce various feedback processes that render the system inherently non-linear. For example, both the low-level westerly winds across the western coast of Africa and the African easterly

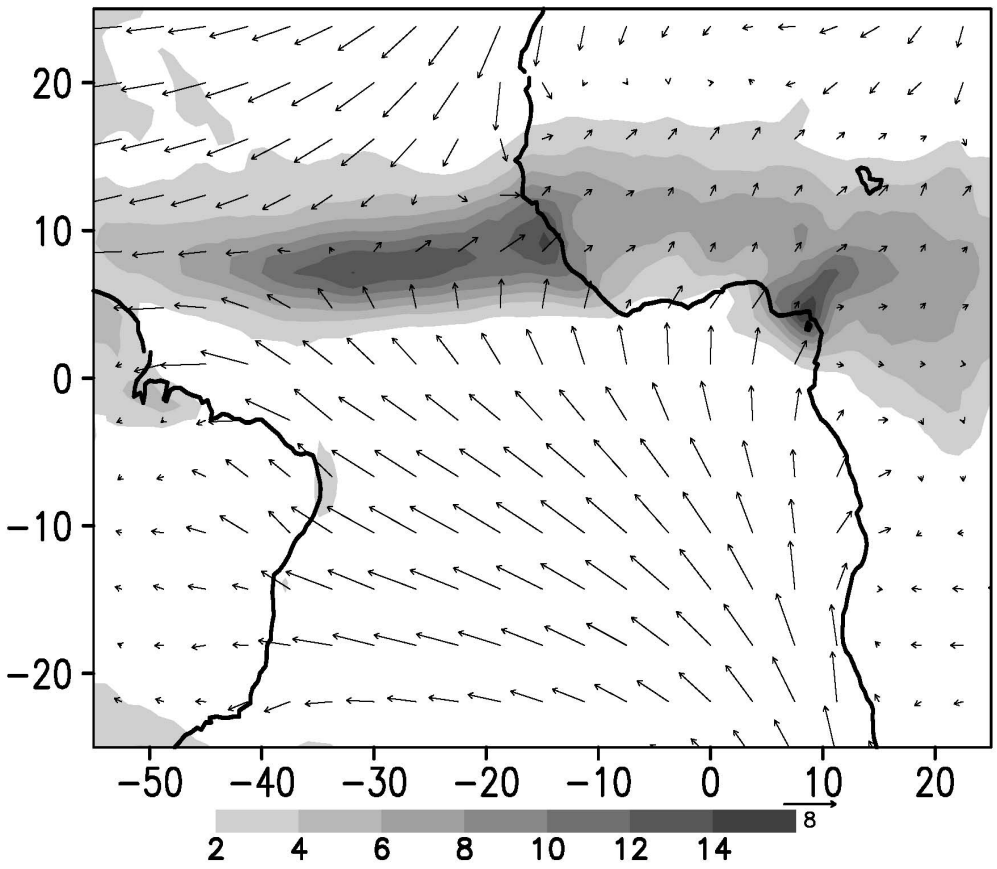

Figure 4.1: 1998 to 2006 mean JAS surface winds (m/s) from the NNRP and precipitation (mm/day) from TRMM (3B42V6).

jet (AEJ) aloft, which maintain the zonal moisture transport, are sensitive to the north-south land surface temperature gradient. This temperature gradient in turn is tied to the precipitation through soil moisture content (Cook 1999).

This land-atmosphere coupling operates at various time-scales. For example, it is implicated in the rapid drying of the Sahara at the end of the African humid period (Patricola and Cook 2007). On seasonal time scales, the relatively long memory of

soil moisture has been suggested as a possible source of predictability (Duoville et al. 2001). In addition, these land surface processes are known to enhance the response of the precipitation to remote forcing on decadal timescales (Zeng et al. 1999).

Various air-sea interaction mechanisms are believed to couple the monsoon dynamics with the regional SSTs (Okumura and Xie 2004, Li and Philander 1992). By partially controlling surface winds and the associated moisture transport, SSTs over the Atlantic Ocean have significant influence on variability at inter-annual to decadal time scales. The two-way interaction of the West African monsoon with eastern tropical Atlantic SSTs, specifically the role of the West African monsoon dynamics in the seasonal SST cycle and the associated feedback onto the monsoon, may contribute to better understanding inter-annual variability and improveprediction.

4.1.2 Seasonality of SSTs in the eastern tropical Atlantic

Sea surface temperature variability over eastern tropical Atlantic is marked by a strong annual cycle. During boreal spring, the sun is directly over the Gulf of Guinea, the trade winds are weak, and a band of high SSTs lies along the equator from 10^0S to 5^0N. As the year progresses, the trade winds along the equator intensify and a rapid decline of SSTs over the eastern equatorial Atlantic follows. For example at 10^0W, equatorial SSTs reach 28^0C in April and drop below 23^0C in July and August. This seasonal warming and cooling is highly asymmetric, with the latter taking only three months and the former seven months (Xie and Carton 2004). Over the northeastern tropical Atlantic, on the other hand, April to August is a period of rapid warming.

Identifying the role of the West African monsoon winds in this pronounced seasonal SST cycle has been a subject of extensive study. Mitchell and Wallace (1992) proposed

that the onset of the summer monsoon is instrumental in initiating the rapid cooling over the equatorial region. According to their observational analysis of SSTs, surface winds, and OLR, the intensification of the northward wind stress across the equator induces a remote response, bringing colder water to the surface just south of the equator to form the characteristic equatorial cold tongue. By further increasing the northward surface wind speed, the subsequent local sea level pressure rise enhances upwelling. They also hypothesize that the marked equatorial asymmetry in the annual mean SST distribution, with warmer waters in the northern tropics, may partly be due to the continental geometry. For example, the fact that the African coastline is parallel to the trade winds near the equatorial region, they argue, favors upwelling and advection of cold water, while the north-south alignment of the west coast of northern Africa favors weakening of the easterly trades.

Subsequent studies using atmospheric GCMs and simple ocean models support this general hypothesis. By forcing the GFDL R30 GCM by SSTs with and without the seasonal cycle, Li and Philander (1997) showed that the enhancement of the meridional winds and the associated surface stress are indeed forced by the warming of the African land surface and the feedback due to the seasonal SST cycle does not have strong influence. In the same study, using the Cane - Zebiak ocean model (Zebiak and Cane 1987) coupled with a one layer atmospheric model, they also show that about 60% of the seasonal SST variations over the Gulf of Guinea can be attributed to variations in evaporation, while other processes such as changes in thermocline depth and cloud feedback play secondary roles.

In contrast, recent studies suggest a more active role of the ocean surface dynamics and associated feedbacks. An atmospheric GCM study by Okumura and Xie (2004), for example, suggests that the southerly flow across the equator is itself enhanced by

the cooling. According to their results, the land surface warming drives cross equatorial southerlies which induce oceanic upwelling south of the equator that cools the eastern equatorial Atlantic. This cooling further intensifies the southerly monsoon flow in the Gulf of Guinea and accelerates the northward shift of the precipitation band and monsoon onset. They also identify a process through which the West African monsoon leads to zonal pressure gradients and the acceleration of the equatorial easterly trades resulting in the westward expansion of the cold equatorial SSTs.

The strong seasonality of the tropical Atlantic Ocean SST has proven remarkably difficult to simulate using coupled GCMs. In an inter-comparison study of 23 models, Devay et al. (2001) demonstrate that the seasonal SST range of most models with no flux adjustment is small compared to the observations. However, they show that many of the models correctly place the maximum in the SST cycle over the eastern tropical Atlantic. Dewitt (2005) shows that a weak zonal wind stress along the equator may be the cause of the incorrect zonal equatorial SST gradient in the ECHAM GCM coupled with the Modular Ocean Model (MOM). In his study, the ocean model was forced by observed and simulated surface winds and the bias in the SST gradient is primarily due to the coupled model's weak zonal wind stress. In their recent analysis of the CCSM3 zonal SST gradient problem, Deser et al. (2006) point to the poor representation of the West African Monsoon by its atmospheric component (CAM3) even when forced by observed SSTs. They argue that the fact that the model puts the summer Sahel precipitation too far inland might affect the air-sea interaction and introduce the bias.

In summary, while the seasonality of SST variability over the Gulf of Guinea and the influence of the monsoon has been studied extensively, the interaction of the monsoon with variability of northeastern Atlantic SSTs has not received as much attention. This application of a coupled regional climate model to study the interaction of the monsoon

with both northeastern Atlantic and Gulf Guinea SSTs provides an appropriate context for both evaluating the regional coupled modeling and improving our understanding of the land-air-sea processes associated with monsoon dynamics.

4.2 Coupled Regional Climate Model Development

4.2.1 Model and Experiment Design

The atmospheric component of the coupled regional climate model (CRCM) is an adaptation of the PSU/NCAR MM5-V3.7 (Grell et al. 1994), also described and applied for African monsoon and variability studies in Vizy and Cook (2002) and Hagos and Cook (2007a and b). The model is non-hydrostatic and solves the equations governing momentum, temperature, pressure, moisture, and liquid water on σ surfaces. Physical parameterizations were tested to produce a realistic representation of the circulation and precipitation over the model domain. The Kuo scheme (Kuo 1974) is used to represent convection, the radiation scheme is adapted from that of the NCAR Community Climate Model 2v (Joseph et al. 1976, Kiehl and Briegleb 1991), and boundary layer processes are represented using the Medium Range Forcasting (MRF) planetary boundary layer scheme (Troen and Mahrt, 1986).

The NCEP Oregon State Air Force Hydrological Lab (NOAH) land surface model is used to represent land surface processes (add reference here – Dudhia? Chen et al 1996?). The surface skin temperature is determined by a linearized surface energy balance, and heat transfer across the four soil layers is represented by the diffusion equation. Soil heat capacity and conductivity are functions of the volumetric soil water content which is governed by Richardson's equation. Land use types are specified according to

obseravtions and held fixed throughout the model integration. In the ocean component of the model, the evolution of SSTs is governed by conservation of energy (see Navarra 1999, Sterl and Hazeleger 2003) according to

$$\rho C_p h \frac{\partial T}{\partial t} = -\rho C_p h \mathbf{V_e} \cdot \nabla T - \rho C_p w_e (T - T_{-}) + Q_{rad} - Q_{lat} - Q_{sen} + \kappa \rho C_p h \frac{\partial^2 T}{\partial z^2}. \quad (4.1)$$

In (4.1) the left hand side is the net heat gain by the mixed layer (hereafter Q_{net}) where T is the temperature of the ocean mixed layer, which is assumed to be isothermal. ρ and C_p are density and specific heat capacity of water, h is the mixed layer depth, $\mathbf{V_e}$ is the Ekman current velocity, T_{-} is the temperature at the base of the mixed layer, and w_e is the vertical entrainment velocity. For brevity, the first two terms on the RHS of (4.1) will be referred to as Q_{adv} and Q_{ent} respectively. Q_{rad} is the net radiative heating, andQ_{lat} and Q_{sen} are the latent and sensible heat fluxes from the ocean to the atmosphere, respectively. The last term represents heat transfer by vertical diffusion, where κ is the diffusion coefficient.

As in the Cane-Zebiak model and (Cane and Zebiak 1987), the dynamics of the Ekman current, $\mathbf{V_e} = (u_e, v_e)$, where u_e and v_e are the zonal and meridional components, is governed by a three-way balance among the mean friction in the mixed layer, the Coriolis force, and the surface wind stress $\tau = \left(\tau_x, \tau_y\right)$ according to

$$r u_e - f v_e = \frac{\tau_x}{\rho h} \quad (4.2)$$

and

$$r v_e + f u_e = \frac{\tau_y}{\rho h}. \quad (4.3)$$

r is the mean friction coefficient in the mixed layer and f is the Coriolis parameter. The vertical entrainment velocity associated with the deepening of the mixed layer and wind-driven divergence, we, is given by

$$w_e = \Gamma(\frac{\partial h}{\partial t} + \nabla \cdot (h V_e)). \quad (4.4)$$

If the mixed layer is thickening, it is entraining cold water. If it is getting shallower, SSTs are not affected. Therefore, $\Gamma = 1$ if the term in the bracket is positive and $\Gamma = 0$ otherwise.

At every time step, the heat and momentum flux terms (Q_{rad}, Q_{lat}, Q_{sen} and τ) are calculated in the atmospheric PBL scheme and communicated to the ocean model. In the ocean model, the net heat flux ($Q_{rad} - Q_{lat} - Q_{sen}$), u_e, and w_e are calculated. Heat transport by advection and entrainment are then calculated, and the diffusion term, $\frac{\partial^2 T}{\partial z^2}$, is approximated by $\frac{(T-T_-)}{h^2}$. Once the SST tendency (LHS of 1) is calculated the SST is updated and fed back to the PBL parameterization where it is used to derive the heat and momentum flux terms for the next time step in the atmospheric model.

In the ocean model, spatial derivatives at an ocean point surrounded by other ocean points are calculated using central finite differencing. If the ocean variable is not defined at a neighboring point, i.e., if a neighboring point is on land, forward or backward difference is used. Simple forward differencing is used to advance SSTs in time.

The seasonal cycle of the ocean mixed layer depth is incorporated using 12 hourly data obtained by interpolating the Naval Research Laboratory monthly climatology of mixed layer depth (Kara et al. 2003). In accordance with the definition of mixed layer depth in this data set, the temperature at the base of the mixed layer is set to be $T_- = \bar{T}_{obs} - 0.8K$ where $\bar{T}_{obs}$ is the climatological annual mean SST from Reynolds and Smith (1995). The vertical diffusion coefficient, κ, is $10^{-5} m^2 s^{-1}$ (as suggested by Brian and Lewis 1979) and C_p is $4218 JK^{-1} kg^{-1}$. To avoid singularity at the equator, the Rayleigh friction coefficient in the Ekman transport equations is set to $r = 0.5 day^{-1}$ (as in Sterl and Hazeleger 2004 and Okumura and Xie 2004). The experiment starts on the 15th of October and runs for one year, with the first 2 weeks discarded as a spin up period.

The model simulations are run over a rectangular domain enclosed by 30^0E to 65^0W and 30^0S to 30^0N. The 90 km grid spacing used in these simulations allows for resolution of the important features over a domain large enough to cover West Africa and the tropical Atlantic Ocean. There are 23 vertical σ levels and the model time step is 90 seconds. The top of the atmosphere is fixed at 50 hPa and an upper radiative boundary condition is used. The effects of snow cover are neglected. The NOAH LSM is initialized by soil moisture and temperature fields at the 10cm and 200cm levels from the NCEP/NCAR Reanalysis Project (hereafter NNRP, Kalnay et al. 1996).

4.2.2 Evaluation

Figure 4.2 displays the mean JAS 10m wind and precipitation from the CRCM simulation. Comparison of Figs. 1 and 2 show that the model reproduces the northeasterly and southeasterly winds over the tropical Atlantic well. In both the reanalysis and the coupled model output, the surface winds are westerly over the northeastern tropical Atlantic (near 10^0N) and directed toward the continent; however in the NNRP, the westerly surface winds into the continent are weaker. In situ measurements suggest that the NNRP underestimates this westerly low-level flow. For example, field studies from the Global Atmospheric Research Program Atlantic Tropical Experiment (GATE) showed these shallow westerly winds contained inside the frictional boundary layer (depth of 2km) between 0^0 and 20^0N attain maximum speeds of 5 m/s at around 8^0N (Grodsky and Carton 2003). The GATE observations indicated that these shallow westerly winds occur over vast areas of the tropical Atlantic sector.

The mean summer precipitation in the model (Figure. 4.2) is compared with the TRMM data in Figure 4.1. The precipitation maxima over the coast of Africa (15^0W)

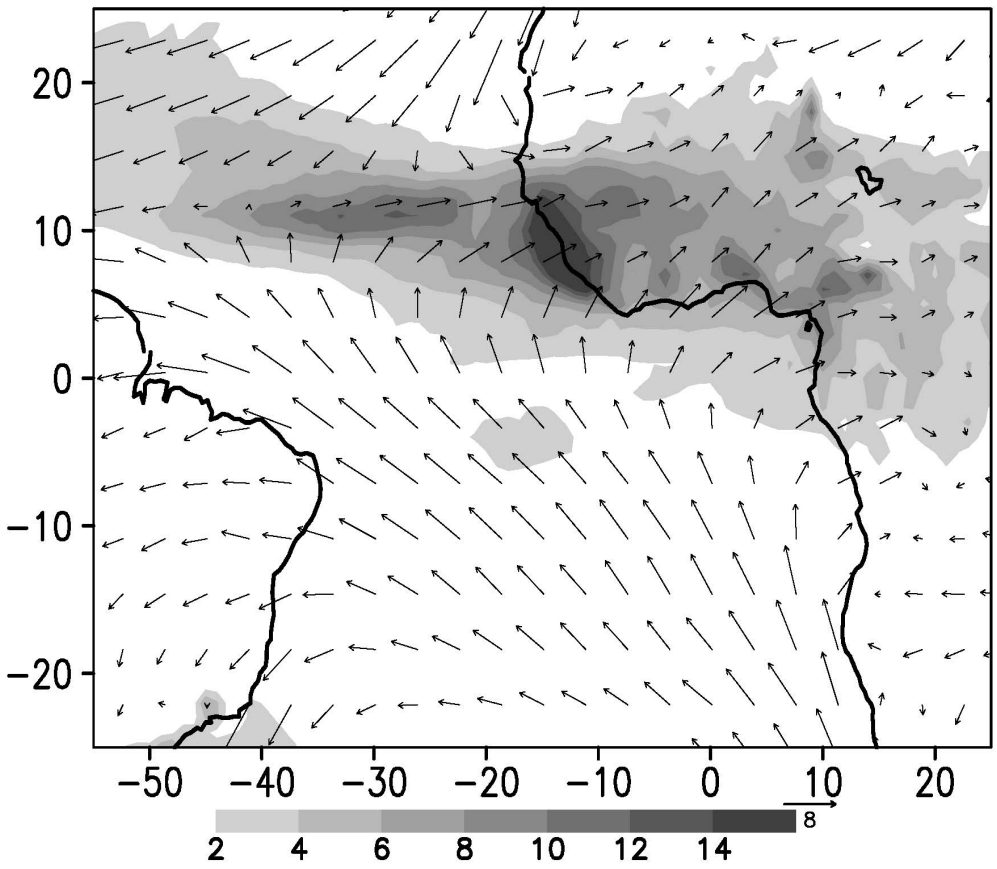

Figure 4.2: JAS surface winds (m/s) and precipitation (mm/day) from the CRCM.

and the Cameroon Highlands (10^0E) are well simulated but precipitation over the central Atlantic is shifted north by about five degrees and is weaker over the western tropical Atlantic.

Here the performance of the model in capturing the monsoon onset and the mean summer precipitation is evaluated. The modeled daily latitudinal migration of precipitation averaged over West Africa (10^0E to 10^0W, Figure 4.3a) is compared with various observational data sets. The JAS 1998-2006 mean precipitation from TRMM (3B42V6)

is displayed in Figure 4.3b. Figures 4.3c and 4.3d display the 1998-2004 JAS mean summer precipitation from the Global Precipitation Climatology Project (GPCP; Huffman et al. 1997) and from the Famine Early Warning System (FEWS; Herman et al. 1997) data.

The model captures the seasonal migration of the precipitation well. Specifically, the magnitude of the simulated precipitation is comparable to the observations and the date of the simulated monsoon jump, the day at which the 10-day running mean precipitation along 10^0N is greater than that along the coast line, is within the range of the observations. The meridional extent of the model precipitation in May is narrower than in the observations and the modeled precipitation over the Gulf of Guinea is on average 2 mm/day drier than the observations.

The simulated mean annual SST is shown in Figure 4.4a. The shading in Figure 4.4a denotes the difference between the simulated and observed SSTs. Over most of the central Atlantic, the mean simulated SSTs are within 1K of the observations. In general, there is a warm bias of about 2K over the eastern Atlantic and a cold bias of similar magnitude over the western tropical Atlantic. This model shares the bias in the east-west SST gradient with many state - of - the - art global models discussed in the introduction. The distribution and magnitude of these biases are remarkably similar to those found in the CCSM3 (Chang et al. 2007) suggesting a common cause despite the differences in the model set-up especially in their oceanic components.

Figs. 4b and c show the evolution of simulated and observed area averaged SSTs over the northeastern Atlantic (the region enclosed by the 10^0N,-22^0N and 18^0W,-38^0W in Figure 4.4a; NETA hereafter) and the Gulf of Guinea (10^0S – 3^0N and 10^0E -10^0W in Figure 4.4a, GOG hereafter). The model reproduces the April to July rapid warming over the NETA region with a bias of about 0.5K. The rapid observed April to July

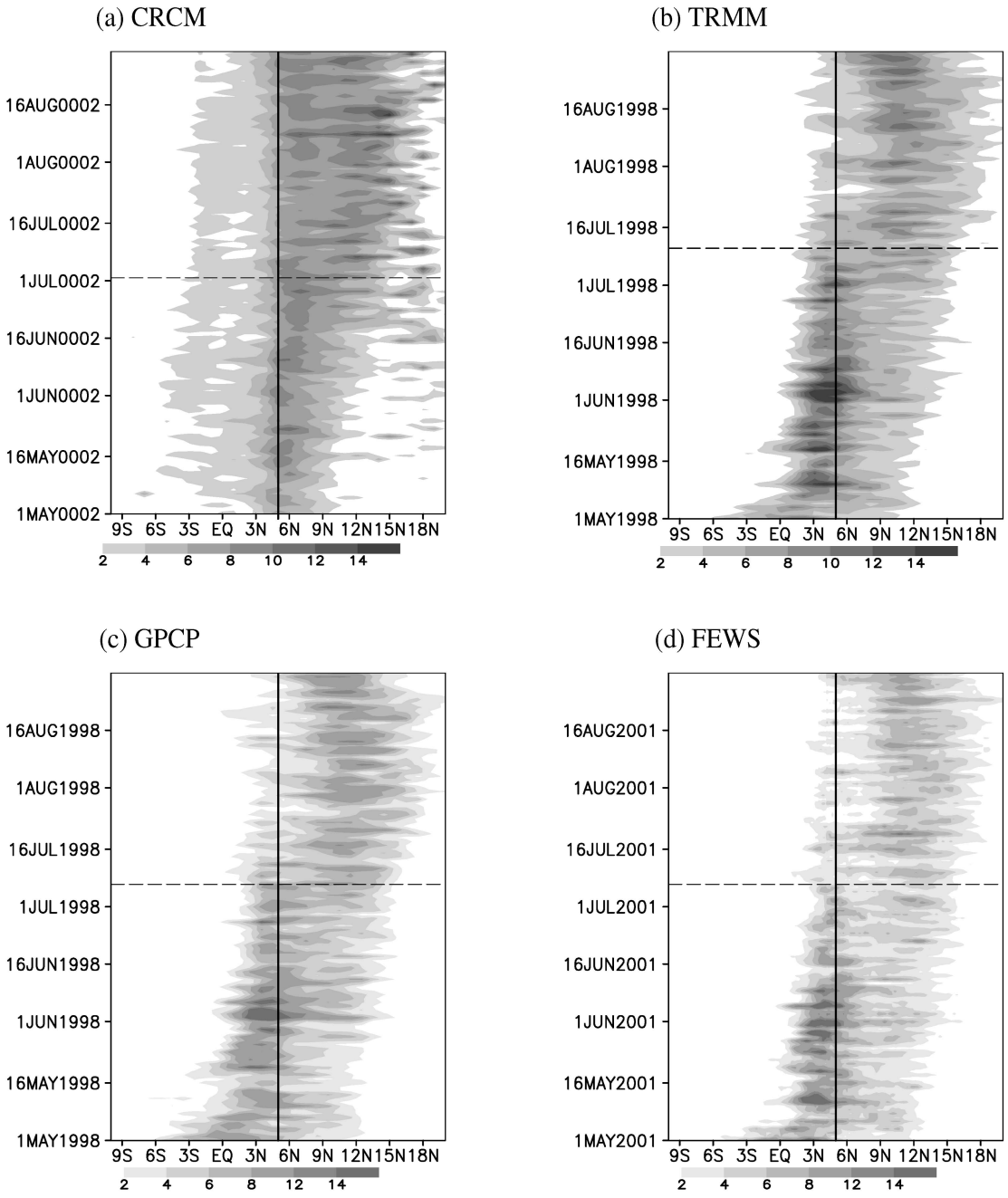

Figure 4.3: Daily precipitation (mm/day) from (a) the CRCM simulation, (b) TRMM (3B42V6, 1998 to 2006 mean), (c) GPCP (1998 to 2004 mean) and (d) FEWS (2000 to 2006 mean)

cooling of GOG SSTs during that period is captured in the simulation but the summer season progresses, the bias becomes significant (up to 2K). During the summer, the model accounts for about half of the seasonal change in SSTs over the GOG.

In summary,

- The model simulates surface winds, summer precipitation and monsoon seasonal cycle reasonably well.
- It reproduces the seasonal SST variability over northeastern tropical Atlantic with a mean bias of less than 1K.
- Even though the model has significant biases of about 2K over the Gulf of Guinea through the summer, the reasonable simulation of April to July SST variations by the CRCM suggests that the April to July rapid cooling over the Gulf of Guinea is partly related to the monsoon dynamics. This connection is further analyzed in the following section.
- Sensitivity tests show that the overall bias in the zonal SST gradient, which the model shares with coupled GCMs, is at least partly related to the relatively weak zonal stress. Appropriate flux corrective steps could be used for multi-year simulations depending on the purpose the study.

4.3 Interaction of the West African Monsoon circulation with the northeastern tropical Atlantic Ocean

As noted in the previous section, the model's performance in simulating the mean SST and seasonal cycle varies spatially. In particular, the model simulates the northeastern

(a) Annual mean SST

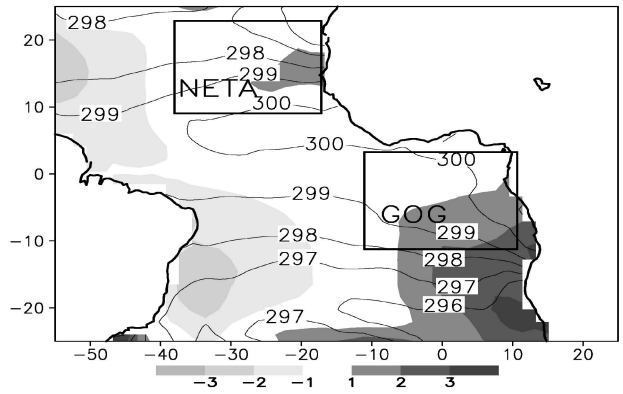

(b) NETA SST

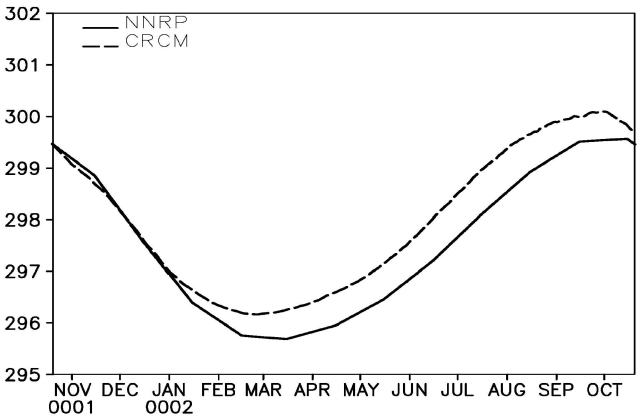

(c) GOG SST

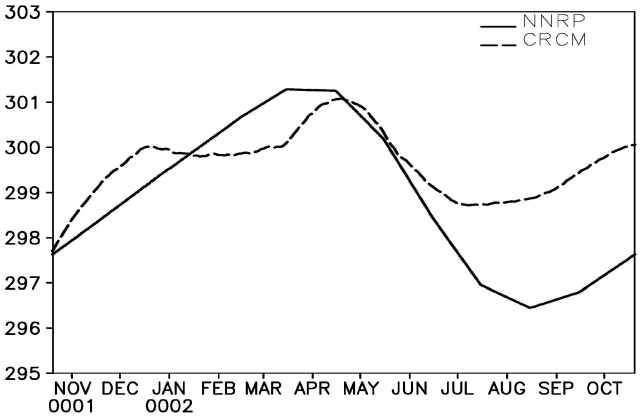

Figure 4.4: (a) Annual mean SST (K) the CRCM and its deviation from the NNRP (shaded) and area average SST cycle over the (b) northeastern tropical Atlantic (NETA) and (c) Gulf of Guinea (GOG) drawn in (a).

tropical Atlantic SST seasonal cycle considerably better than it does the Gulf of Guinea seasonal SST cycle. Here we examine the dynamic and thermodynamic interactions of the monsoon with the northeastern tropical Atlantic.

A surface energy budget analysis shows that the primary balance over the NETA region is between radiative heating and evaporation cooling. Figure 4.5a shows this balance. Entrainment cooling is small during spring. During the fall and winter, evaporative cooling dominates over radiative heating and there is a net loss of heat from the mixed layer. During the spring and summer, radiative heating exceeds evaporative and entrainment cooling and there is a net heat flux into the ocean mixed layer.

Most of the seasonal variation in the mixed layer heat content is related to seasonal variations in radiative heating. However, the roles of the suppressed evaporation and sensible cooling between May and August and increased entrainment cooling between July and September are significant. In particular the combined contribution from the suppression of evaporation and sensible cooling becomes comparable to that of radiative heating in July. By the end of the summer, entrainment cooling becomes the primary process associated with the SSTs' decline. At their respective maxima, contributions from the suppression of evaporation and increased entrainment cooling are comparable to that of radiative heating. This suggests an important role of the surface winds in the seasonal SST cycle.

To isolate the physical processes that suppress evaporation between May and August over the NETA, surface winds and moisture content are considered. Figure 4.6 shows the surface wind speed as well as its zonal and meridional components averaged over the NETA region. The decline in total wind speed is due to that of the meridional component which halved between April and August.

(a) NETA heat budget

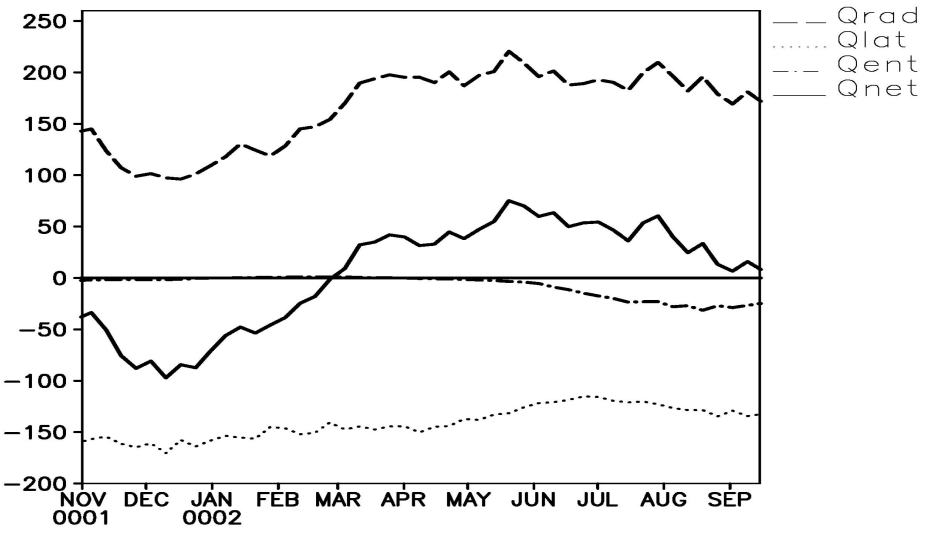

(b) NETA heat budget - annual mean

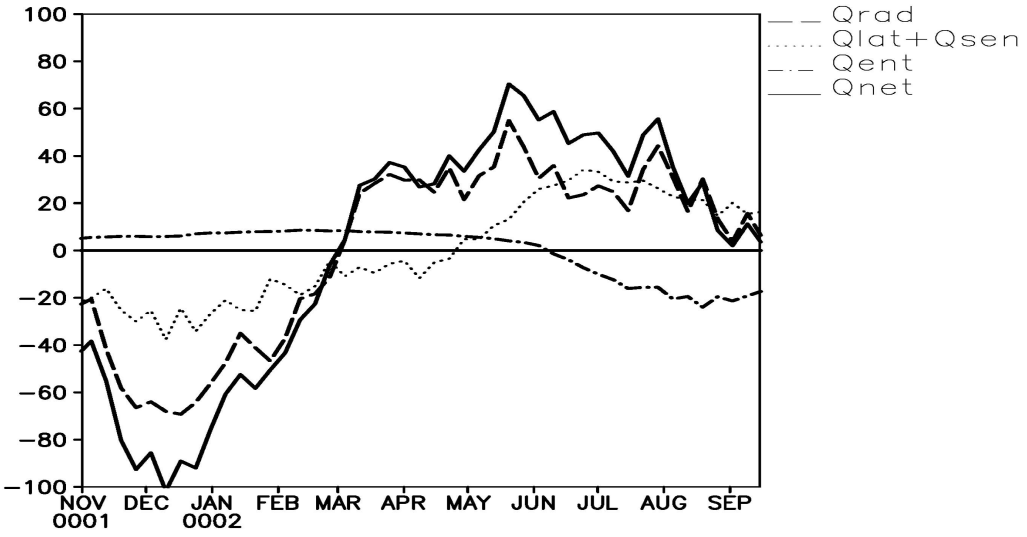

Figure 4.5: (a) The energy budget terms and (b) their deviation from their respective annual averages (Wm^{-2}) over NETA.

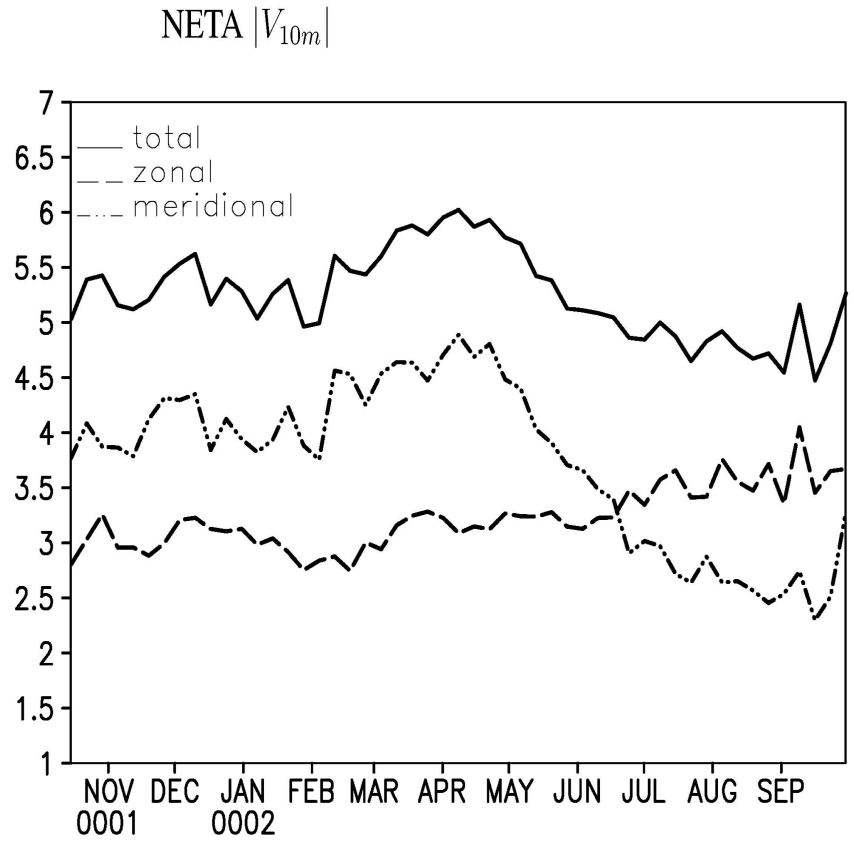

Figure 4.6: Surface wind speed (m/s) area averaged over NETA.

As discussed in the introduction, the period of transition between northern spring and summer is marked by the northward migration of the line of confluence of the northeasterly and southeasterly winds. Figures 4.7a and 4.7b show the evolution of surface pressure and the meridional surface winds over the NETA from the CRCM and the NNRP, respectively. In both panels, the northward migration of the southerly winds (the 5m/s contour, for example) is apparent, and it leaves the NETA (which is denoted by the dashed lines) with low wind speed. This is related to the northward migration of the ITCZ low pressure. This is demonstrated by the tilt of the 1016hPa and 0m/s contour

in Figure 4.7a.

In addition to influencing heat transfer between the atmosphere and the ocean, the winds over the NETA apply stress to the ocean surface which induces entrainment. As shown in the energy budget analysis, this entrainment is the primary cooling mechanism at the end of the summer. Figure 4.8 shows the surface winds and the associated wind-driven ocean currents in August (the month in which entrainment is at its maximum). Because of Coriolis effect, the strong westerly flow onto the continent near 10^0N drives southeasterly currents. This results in divergence and entrainment cooling to the north of the surface wind maximum. The same effect of the westerly flow is also identified in an observational and numerical study by Grodsky et al. (2003).

The primarily non-divergent westerly surface flow onto the continent is part of the cyclonic circulation associated with the African heat low (Figure 4.9). During the summer, increased soil moisture and reduced surface temperature enhances the temperature gradient between the Sahel and the Sahara and leads to the northward expansion of this westerly low level flow. Its westward extension also exhibits significant seasonal variation. The direction of the zonal surface winds over the NETA depends on the competition between the North Atlantic high, which favors easterly flow, and the African heat low, which favors westerlies. During the summer, the weakening of the North Atlantic high enables the strengthening and westward expansion of the westerly winds (compare Figs. 9a and b). In this way, mediated through the North Atlantic high, the seasonal SST variability of northeastern Atlantic modulates the westerly surface winds.

SST seasonal cycle also controls the availability of moisture for transport into the continent. Figure 4.10 shows the zonal wind and mixing ratio off the west coast of Africa in April and July. In summer, the increased mixing ratio coupled with the increased westerly flow into the continent supplies moisture for the inland monsoon precipitation.

(a) CRCM

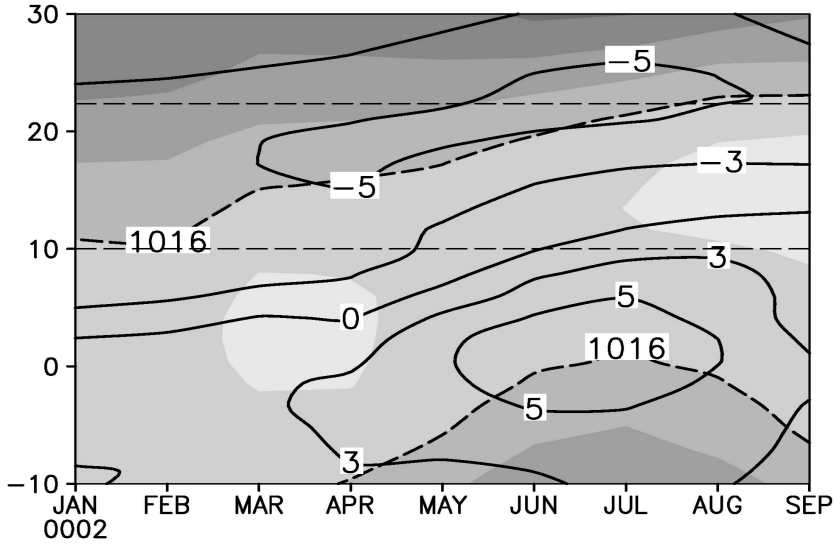

(b) NNRP

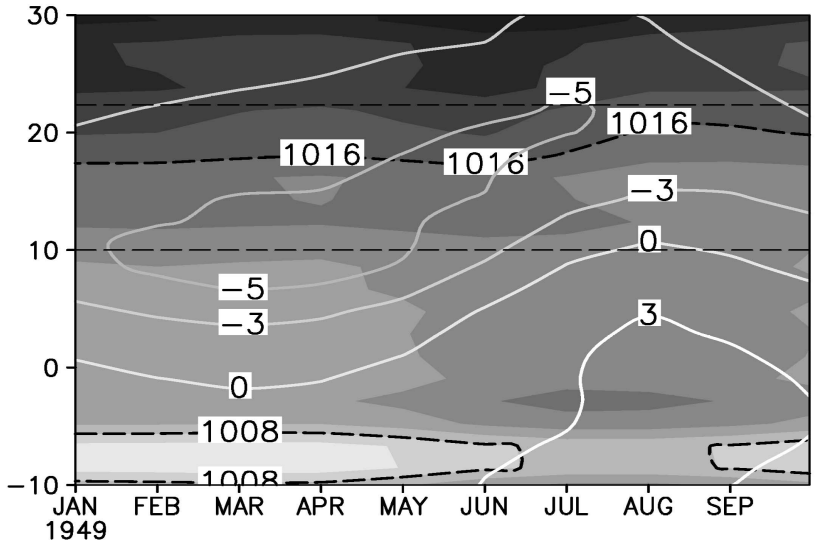

Figure 4.7: (a) Surface meridional wind speed (m/s) and surface pressure (hPa) from (a) CRCM and (b) NNRP. Both averaged over NETA (10E to 10W). Distance between shades is 2hPa.

(a) Surface wind (Aug)

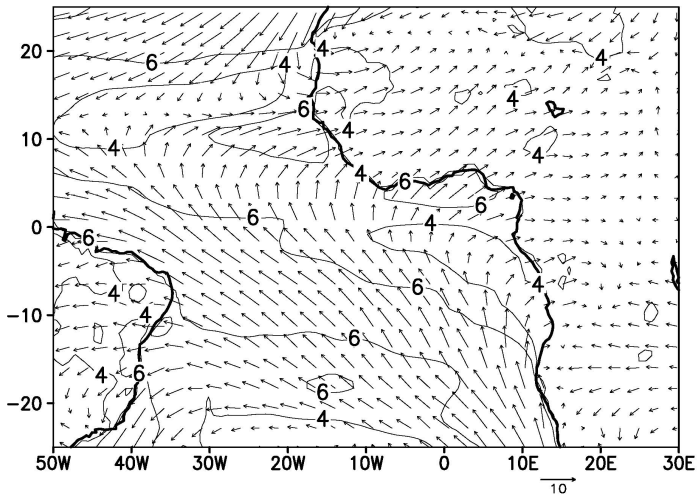

(b) Wind driven currents (Aug)

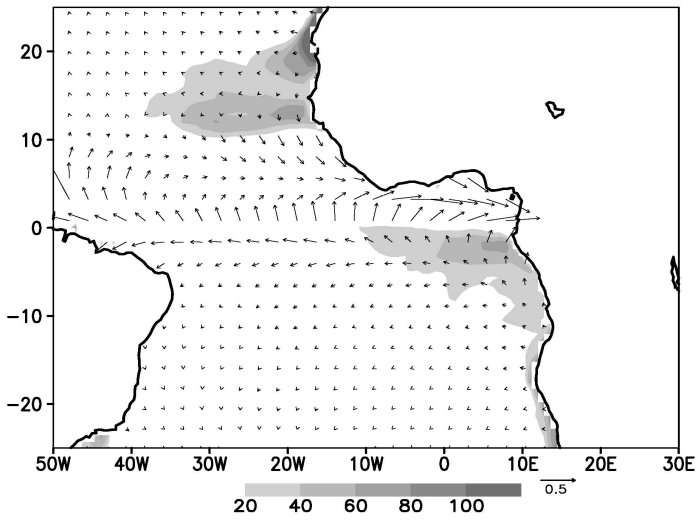

Figure 4.8: (a) Surface winds (m/s), wind speed (contours) and (b) wind driven currents (m/s) and entrainment cooling (shaded in Wm^{-2}) in August.

(a) April

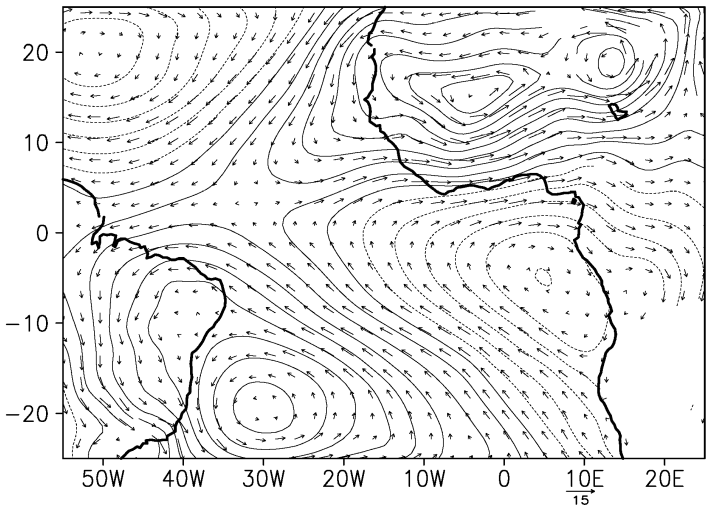

(b) July

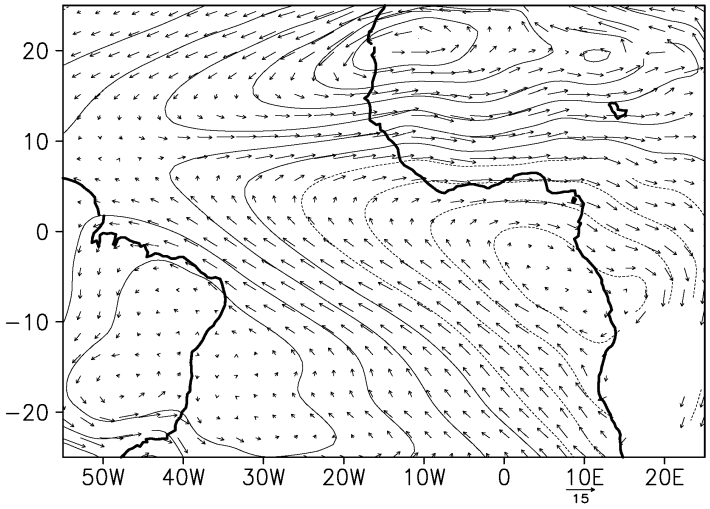

Figure 4.9: Mean (a) April and (b) July irrotational component of surface wind (m/s) and stream function.

By enhancing the saturation mixing ratio, the seasonal warming increases the amount of moisture available for transport into the continent.

4.4 Interaction of the West African Monsoon circulation with Gulf of Guinea SSTs

Because the model fails to fully account for seasonal SST variations over the GOG region, comparison of the energy budget terms could lead to erroneous conclusions. However, enumeration of the important processes simulated provides some information on the monsoon-ocean interaction in this region. The seasonal cooling over the Gulf of Guinea is accompanied by an enhancement of the surface monsoon winds. Figure 4.11 shows the evolution of the area averaged wind speed and its zonal and meridional components over the GOG. The rapid increase in wind speed between April and July coincides with the decrease of GOG SSTs. Most of the wind speed change is related to the meridional component which almost doubles during this period. The increase in the zonal component is gradual.

The southerly winds over the GOG exert stress over the ocean which induces entrainment. Figure 4.12 shows the surface winds and the associated wind driven ocean currents in May, when the entrainment is at its maximum. Over the southeastern tropical Atlantic, there is little meridional variation in the magnitude of the surface winds. For example, the wind speed at (0^0, 0^0) is about 6m/s southerly and that over (0^0, 10^0S) is also about 6m/s but southeasterly (Figure 4.12a). But because of the variation of the Coriolis parameter with latitude, the response of the ocean surface to the stress exerted at the two latitudes is different. On the equator, the primary balance is between the surface stress and friction in the mixed layer. Therefore, the ocean currents are in the

(a) April u and q at (20^0W)

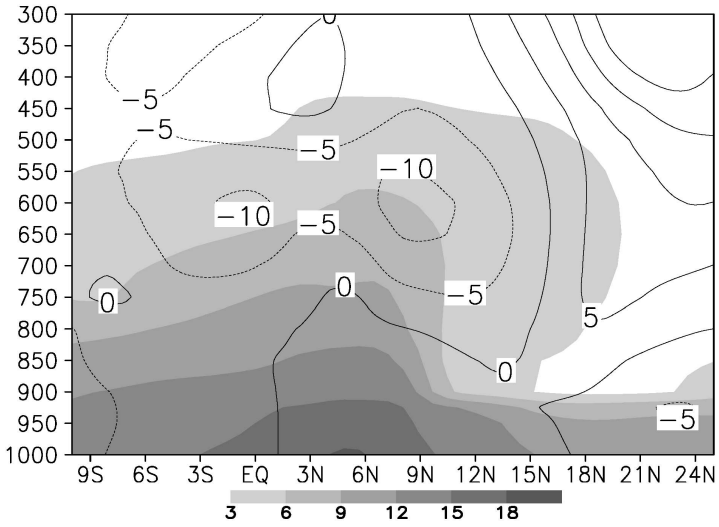

(b) July u and q at (20^0W)

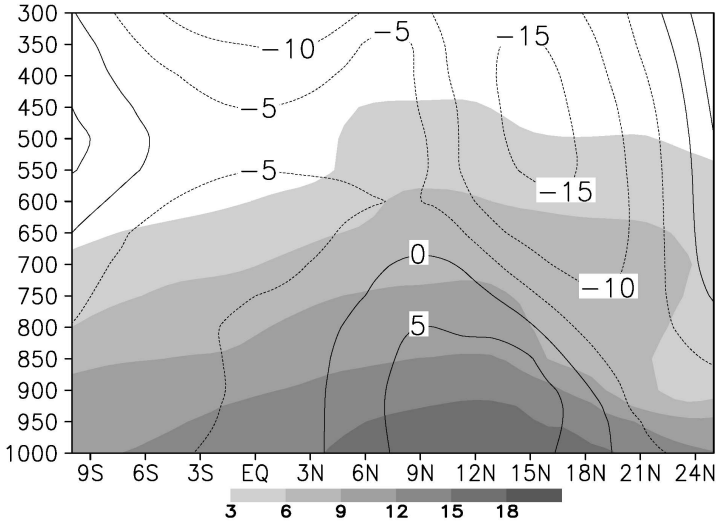

Figure 4.10: Zonal wind (m/s) and mixing ratio (g/kg) at 20^0W in (a) April and (b) July.

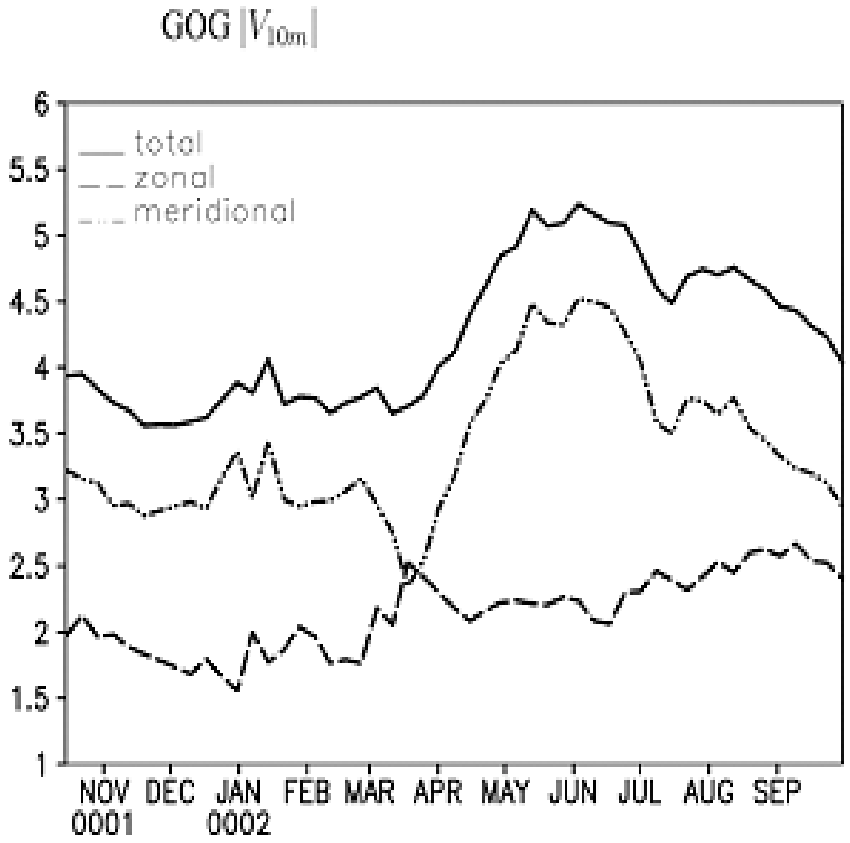

Figure 4.11: Surface wind speed (m/s) area averaged over the GOG.

same direction as the surface winds (Figure 4.12b). At 10^0S, on the other hand, friction and Coriolis forces are comparable and the surface currents are oriented at an angle of about 45 degrees to the surface winds. This results in the divergence of ocean currents and upwelling. This process is also identified in anumerical study by Philander and Pacanowski (1981). Similarly, the southerly winds near the coast induce easterly currents and cooling (shaded) due to coastal upwelling along the southern coast of Africa. The relatively shallow mixed layer thickness (Figure 4.12b) over the region also contributes to the higher sensitivity of SSTs to variations in the net heat flux. Increased

evaporation and decreases in radiative cooling also contribute to the accelerated cooling in the model.

To estimate the relative roles of variations in pressure over land and ocean in forcing the acceleration of these southerly winds, the seasonal evolution of the surface pressure is considered. Figures 4.13a and 4.13b show the evolution of the mean surface pressure (shaded) and the meridional velocity (contours) from the CRCM and the NNRP, respectively. They show that while the African heat low is in place for most of the year, the meridional wind speed near the equator varies with pressure over the Gulf of Guinea. In both the CRCM and the NNRP, the meridional wind speed reaches its maximum near (and slightly ahead of) the surface pressure to the immediate south. The fact that the northward movement of the high is well simulated despite relatively warm SSTs compared to the observations suggests that strong southerly winds might be responsible for the rapid northward advection of the high pressure as suggested by Okumura and Xie (2004).

The changes in radiative heating due the seasonal northward migration of the sun and associated changes in the stratus clouds which are not simulated well in our regional model could have important contributions to the seasonal SST cycle and interactions with the monsoon. As the mixed layer becomes shallow the fraction of solar radiation transmitted into the deep ocean. The absence of this mechanism in this model could also have contributed to the warm bias over the Gulf of Guinea.

(a) Surface wind (May)

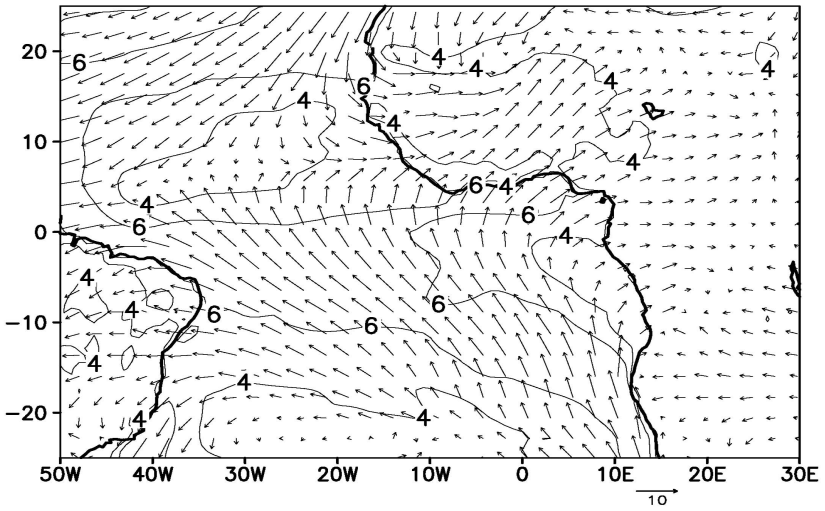

(b) Wind driven currents (May)

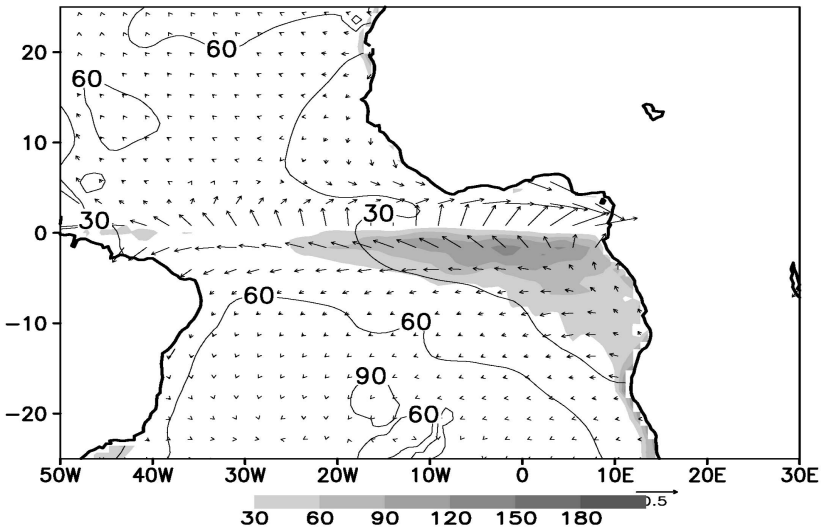

Figure 4.12: (a) Surface winds (m/s), wind speed (contours) and (b) wind driven currents (m/s) and entrainment cooling (shaded in Wm^{-2}) in May.

(a) CRCM

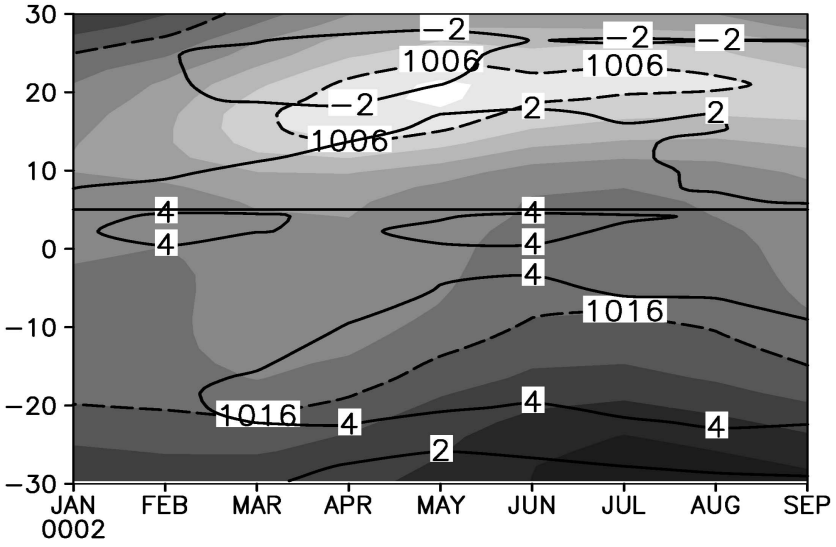

(b) NNRP

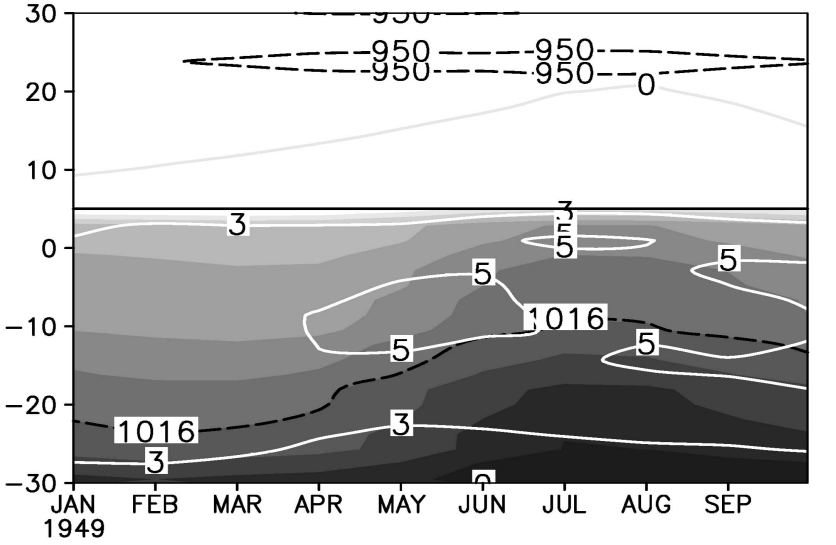

Figure 4.13: (a) Surface meridional wind speed (m/s) and surface pressure (hPa) from (a) CRCM and (b) NNRP. Both averaged over GOG (10E to 10W). The spacing between shades is 2hPa.

4.5 Discussion

In this study the development of a regional coupled model and its application to ocean-atmosphere-land interactions over West Africa and the adjacent Atlantic Ocean are presented. The model includes both dynamic and thermodynamic air-sea interactions as well as a land surface scheme. It is a coupling of the NCAR/PSU MM5 regional climate model with an ocean mixed layer model with observed spatially and seasonally varying mixed layer depth.

The ability of the model to simulate the monsoon dynamics and precipitation and the SST seasonal cycle are evaluated. The model simulates the monsoon precipitation as well as its seasonal cycle well, and the associated surface winds compare well with the NCEP/NCAR reanalysis. Without any flux corrective measures the model captures the full seasonal cycle of SSTs over the northeastern tropical Atlantic, but the simulated Gulf of Guinea SST seasonal seasonality is smaller than in the observations. In particular, the modeled summer SSTs over the Gulf of Guinea are warmer by about 2K.

Air sea interactions over the northeastern tropical Atlantic, off the west coast of Africa, are further investigated. While the primary factor for the seasonal SST cycle in this region is solar heating, suppression of evaporation during early summer and entrainment cooling at the end of the summer play important roles, comparable to the radiative heating variation. The suppression of evaporation is mainly due to the northward migration of the ITCZ and the associated reduction of meridional wind speed. The seasonal SST warming weakens the North Atlantic high, weakening the associated anticyclonic easterly winds and favoring the westward expansion of the cyclonic westerly flow associated with the African heat low. This coupled with the seasonal northward migration of the mixing ratio maximum, enhances moisture transport into the continent. As the sum-

mer progresses, the stress associated with the westerly winds induces southerly ocean currents. These currents result in upwelling to the immediate north of the westerly flow and initiate the gradual decline of SSTs.

Similarly, over the Gulf of Guinea the start of the monsoon season is accompanied by the acceleration of southerly winds across the equator. Because of variations of the Coriolis force with latitude, these winds drive upwelling (and cooling) to the immediate south of the equator. In addition to that the acceleration of the southerly winds through the spring appears to contribute to the advection of high pressure over to the Gulf of Guinea.

The low level flow across the western coast is known to be significantly correlated with precipitation over the Sahel on interannual timescales. For example, Grist and Nicholson (2001) show stronger low level westerly winds during wet years in the western Sahel. Understanding the three-way interactions among northeastern Atlantic SSTs, the low-level monsoon flow and precipitation contributes to better understanding of precipitation variability on interannual timescales and beyond.

BIBLIOGRAPHY

[1] Brian, J. P. , and L. J. Lewis, 1979: A water mass model of the world ocean. *J. Geophys. Res.,* **84,** 2503–2517.

[2] Cook, K. H. 1999: Generation of the African Easterly Jet and its Role in Determining West African Precipitation, *J. Climate* **12**, 1165–1184.

[3] Cook, K.H., and E.K. Vizy, 2006: Coupled Model Simulations of the West African Monsoon System: Twentieth- and Twenty-First-Century Simulations. *J. Climate*, **19**, 3681–3703.

[4] Chang, C.Y., J.A. Carton, S.A. Grodsky, and S. Nigam, 2007: Seasonal Climate of the Tropical Atlantic Sector in the NCAR Community Climate System Model 3: Error Structure and Probable Causes of Errors. , **20**, 1053–1070.

[5] Chen, F., K. E. Mitchell, J. Schaake, Y. Xue, H.-L. Pan, V. Koren, Q. Y. Duan, M. Ek, and A. Betts, Modeling of land-surface evaporation by four schemes and comparison with FIFE observations, J. Geophys. Res., 101, 7251–7268, 1996.[AGU]

[6] Davey M., Coauthors, 2002: STOIC: A study of coupled model climatology and variability in tropical ocean regions. *Climate Dyn.*, **18**, 403–420.

[7] Deser C., A. Capotondi, R. Saravanan, and A. Phillips, 2006: Tropical Pacific and Atlantic variability in CCSM3. J. Climate, 19, 2451–2481

[8] Douville, H., F. Chauvin, and H. Broqua, 2001: Influence of Soil Moisture on the Asian and African Monsoons. Part I: Mean Monsoon and Daily Precipitation. *J. Climate*, **14**, 2381–2403.

[9] DeWitt D. G., 2005: Diagnosis of the tropical Atlantic near-equatorial SST bias in a directly coupled atmosphere-ocean general circulation model. *Geophys. Res. Lett.*, **32**, L01703, doi

[10] Foltz, G., S.A. Grodsky, J.A. Carton, and M. McPhaden, 2003: Seasonal mixed layer heat budget of the tropical Atlantic, *J. Geophys. Res.* , **108**, 3146

[11] Grell, G.A., J. Dudhia, and D.R. Stauffer, 1994: A description of the fifth-generation Penn State/NCAR mesoscale model (MM5). NCAR Tech. Note NCAR/TN-398+STR, 122pp.

[12] Grist, J.P., and S.E. Nicholson, A study of the dynamics factors influencing the rainfall variability in the West African Sahel, J. Clim., 14, 1337-1359, 2001.

[13] Grodsky, S. A., J. A. Carton, and S. Nigam (2003), Near surface westerly wind jet in the Atlantic ITCZ, Geophys. Res. Lett., 30(19), 2009,

[14] Hagos S. M. and K. H. Cook 2007a: Dynamics of the West African Monsoon Jump., *J. Clim.*, in press.

[15] Hellerman, S., and M. Rosenstein, 1983: Normal monthly wind stress over the world ocean with error estimates. J. Phys. Oceanogr., 13, 1093-1104.

[16] Herman, A. V.B. Kumar, P.A. Arkin, and J. V. Kousky, 1997: Objectively Determined 10-Day African Rainfall Estimates Created for Famine Early Warming Systems, Int. J. Remote Sensing, 18, 2147-2159.

[17] Huffman, G. J, and Coauthors, 1997: The Global Precipitation Climatology Project (GPCP) combined precipitation dataset. *Bull. Amer. Meteor. Soc.,* **78,** 5–20.

[18] Huffman, G.J., R.F. Adler, M. Morrissey, D.T. Bolvin, S. Curtis, R. Joyce, B McGavock, J. Susskind, 2001: Global Precipitation at One-Degree Daily Resolution from Multi-Satellite Observations. J. Hydrometeor., 2(4.1), 36-50.

[19] Joseph, J.H., W.J. Wiscombe, and J.A. Weinman, 1976: The delta-Eddington approximation for radiative flux transfer. *J. Atmos. Sci.,* **33**, 2452-2459.

[20] Kalnay, E. M, and others, 1996: The NCEP/NCAR 40-year reanalysis project. *Bull. Amer. Meteor. Soc.* **77** 437- 471.

[21] Kara, A. Birol; Rochford, Peter A.; Hurlburt, Harley E. 2003: Mixed layer depth variability over the global ocean. *J. Geophys. Res*., 108, C3, pp. 24-1,

[22] Kiehl, J.T., and B.P. Briegleb, 1991: A new parameterization of the absorptance due to the 15-micron band system of carbon dioxide. *J. Geophys. Res*., **96**, 9013-9019.

[23] Kuo, H.L., 1974. Further studies of the influence of cumulus convection on large-scale flow. *J. Atmos. Sci.* **31**, pp. 1232–1240.

[24] Li, T., and S.G.H. Philander, 1997: On the seasonal cycle of the equatorial Atlantic Ocean, J. Climate, 10, 813-817

[25] Mitchell, T., and J. M. Wallace, 1992: The annual cycle in equatorial convection and sea surface temperature. *J. Climate*, **5**, 1140–1156.

[26] Navarra, A., Beyond El Nino Decadal and Interdecadal Climate Variability 1999: Springer 374pp.

[27] Okumura, Y., and S.-P. Xie, 2004: Interaction of the Atlantic equatorial cold tongue and African monsoon, *J. Clim.*, **19** ,5859 - 5873.

[28] Patricola, C. M. and K. H. Cook, 2007: A Mechanism for Abrupt Climate Change over Northern Africa: Interactions Between Vegetation and the African Easterly Jet, *submitted to Journal of Climate.*

[29] Philander, S. G. H., and R. C. Pacanowski, 1981: The oceanic response to cross equatorial winds (with applications to coastal upwelling in low latitudes). Tellus, 33, 201-210.

[30] Sterl, A., and W. Hazeleger (2003), Coupled variability and air-sea interaction in the South Atlantic Ocean, Climate Dyn., 21, 559-571.

[31] Troen, I. and L. Mahrt, 1986: A simple model of the atmospheric boundary layer: Sensitivity to surface evaporation. *Bound. Layer Meteorol.*, **37**, 129-148.

[32] Vizy, E. K., and K. H. Cook (2002), Development and application of a mesoscale climate model for the tropics: Influence of sea surface temperature anomalies on the West African monsoon, J. Geophys. Res.- Atmos., 07(D3)

[33] Xie, S.-P., and J.A. Carton, 2004: Tropical Atlantic variability: patterns, mechanisms, and impacts, in "Ocean-Atmosphere Interaction and Climate Variability", edited by C. Wang, S.-P. Xie, and J. A. Carton, AGU Press.

[34] Zebiak, S. E. and M. A. Cane (1987): A model El Nino-Southern Oscillation. *Mon. Wea. Rev.*, **115**, 2262–2278.

[35] Zeng, N., J. D. Neelin, K.-M. Lau, and C. J. Tucker (1999), Enhancement of interdecadal climate variability in the Sahel by vegetation interaction, Science, 286, 1537–1540.

Chapter 5

Conclusion

This study contributes to our current understanding of the West African Monsoon dynamics, variability and interactions with the Atlantic Ocean surface. It identifies various processes involving thresholds, nonlinear interactions and feedback between perturbations and climatology.

The West African Monsoon jump, which is the decline of precipitation along the coast of Guinea and increased precipitation in the continental interior, is the result of low level moisture supply forced by the warming over land and associated condensation. This condensational heating in turn enhances pressure gradient between the free atmosphere over land and the ocean leading to inertial instability. This leads to the demise of precipitation along the coast and the deepening of the monsoon flow into the continental interior.

The modeling study also shows that decadal variability in the Atlantic and Indian Ocean SSTs have strong influence over Sahel precipitation. In particular, analysis of the modeled dry conditions over Africa in response to the 1980s observed SSTs and the relatively wetter response to 1990s SSTs show that anomalous circulation patterns, moisture transport and ultimately Sahel precipitation are sensitive to the scale and distribution of SST anomalies and the background moisture distribution. These circulation and moisture transport patterns are further amplified by the response to the condensational heating anomalies.

Finally, this study identifies the mechanisms of coupling between the monsoon circulation and the Eastern Tropical Atlantic SST cycle. While much of the cooling over the Gulf of Guinea is related to evaporation and entrainment cooling forced by the southerly

surface winds, the cooling and attendant high pressure contribute to the increased land-sea pressure gradient. The northward migration of the ITCZ from spring to summer and associated decline in wind speed over northeastern tropical Atlantic suppress evaporation and contribute to the seasonal warming off the western coast of the Sahel.

Because of its potential impact on large population, as witnessed in the last few decades, understanding climate variability and change over the Sahel and producing projections for 21st century have been important areas of research. The results of this study suggest that understanding climate variability and improving prediction requires thorough untangling of nonlinear interactions, feedbacks and thresholds. For example, if the circulation patterns and precipitation are sensitive to the scales and distributions of SST anomalies and the background conditions, pin pointing the impact of climate change will partly require identification of the SST patterns that give rise to a certain response and quantifying the projection of the future SST anomalies on those patterns.

In general, modeling study of climate change requires thorough understanding of many complex processes. The climate scientist has responsibility to insure that the projections are rooted on solid scientific ground and to provide policy makers and the general public with clear and sound information on the current understanding and uncertainties. This endeavor is likely to take decades of patient and multidisciplinary work and this dissertation is a contribution toward that goal.